Bulgarian Academy of Sciences. Space Research Institute.
Aerospace Research in Bulgaria. 19, 2005, Sofia

AEROSPACE RESEARCH IN BULGARIA

Volume 19 * Sofia * 2005
Space Research Institute
Bulgarian Academy of Sciences

Address
AEROSPACE RESEARCH IN BULGARIA
Space Research Institute
6 Moskovska, Sofia 1000,
Bulgaria
E-mail: office@space.bas.bg,
http://www.space.bas.bg

Editor&Translation
Lubomira Kraleva

Technical Editor
Valeri Vassev

ISSN 0861-1432

Aerospace Research in Bulgaria

19/2005

C o n t e n t s

Съдържание

Bulgarian Academy of Sciences. Space Research Institute.
Aerospace Research in Bulgaria. 19, 2005, Sofia

SOME POTENTIALITIES FOR USING AEROSPACE INFORMATION IN THE FIELD OF NATIONAL SECURITY AND DEFENCE

Petar Getsov, Pavel Penev

Space Research Institute, Bulgarian Academy of Sciences

Abstract

The modern tendencies in using remote sensing techniques and systems for studying the Earth from space are formulated. The potentialities to use dual-destination space monitoring commercial satellites on the territory of the Republic of Bulgaria are outlined. General formulation of the tasks in the field of defence and security resolved through the space segment is given. A structure for a sovereign National Space Information Centre is suggested.

Introduction

This paper marks the start of a series of papers to be published in the journal *Aerospace Research in Bulgaria* dedicated to observing the Earth's surface by aircrafts and satellites for the purpose of resolving a wide scope of tasks in the field of crises management, national security and defence, agriculture, ecology and more. Many of the materials have been reported at various fora with the aim to urge the responsible bodies and institutions to take adequate decisions for undertaking and implementing a national monitoring system.

Based on the analysis of the current *status quo* of the country in the field, as well as on our long-lasting efforts to establish a National Aerospace Information Centre, we start a series of papers and suggestions related with national security, which is a modern and effective trend in the leading countries' defence and security in the end of the XX-th and the beginning of the XXI-st century.

The ready access to and moderate cost of a number of space technologies provide for their successful use nowadays by countries of the size of the Republic of Bulgaria (such as the Netherlands, Israel, Greece, Belgium etc.).

The analysis of world experience reveals that using space-based technologies provides to overcome a great part of the shortcomings and restrictions of traditional ground-based technologies related primarily with observation, communication, and navigation.

One basic type of space information systems, occupying a significant part of the field, are Remote Sensing Satellite Systems (RSSS), through which information about the Earth is acquired and interpreted.

The current great importance and wide application of RSSS providing the so-called **space monitoring** is determined by the following circumstances:

- global spatial scope of the observed territory (aquatoria);
- possibility to observe specific areas or objects in various spectral ranges at given intervals, day or night, or in complex meteorological conditions
- possibility to obtain images featuring high resolution and providing abundant information, and quite often – the required operativenesss;
- well developed international market of space video- and photoimages.

The most active and dynamic component of the RSSS is the earth satellite furnished with appropriate dedicated equipment. It translates information about the monitored area to ground-based receiving centres either directly or through retranslating satellites.

Currently, the RSSS provide mainly three types of images: photoimages, electronic-optic images, and radiolocation images.

On the brink between the XX-th and the XXI-st century, a number of modern tendencies are observed related with the use of remote sensing techniques and systems for study of the Earth from space, such as:

- transfer of technologies;
- commercialization of high-resolution space images;
- integration of various-destination systems;
- introduction of GIS;
- facilitated online customer access to supplied data;
- mutual penetration and integration of military and civil space systems etc.

The tendencies outlined above suggest intensive penetration of space monitoring in both defence and security structures, as well as in communication, geodesy and cartography, transport, ecology, power engineering, agriculture, meteorology etc.

The experience from the so-called "space epoch wars", starting with Desert Storm (1991) and ending with the military campaign in Iraq (2003) reveals that the MoD of the USA, irrespective of the military space system orbital formations it has maintained for dozens of years already, is among the greatest users of information supplied by civil RSSS (such as the *Landsat*, *Spot*, *Ikonos* etc.). The latter has been used successfully to plan the troops' military activities and to spot aviation targets.

A tendency in space technologies on a world scale to reduce the gap in the information potentialities of RS earth satellites for civil and military purpose (Fig. 1) has been observed. Thus, for instance, the civil satellites *Ikonos*, *Quick Bird*, *Orb View*, *Resurs–DK* etc. feature image resolution of 1-4 m in the monochromatic and multispectral regime. The available ground-based receiving stations or terminals will provide to obtain on-line information about the observed objects. This will make it possible, at nowadays' stage of space technologies development, using information from some civil RS Earth satellites, to also resolve military problems, including tactic ones, with a number of RSSSs featuring **dual destination.**

Among the companies constructing and launching in space commercial RS Earth satellites with particularly important military application are the American companies Space Imaging which constructed the satellite *Ikonos* and Digital Globe which constructed the satellite *Quick Bird*. The information from the mentioned "high-resolution" satellites triggered the establishment of a **coordinate data base** for each theatre of war, ensuring the successful hitting by controlled aircraft (rockets, aviation bombs etc.) of some specific targets using GPS–corrected orientation. Moreover, the information from these satellites provides to construct 3D models of the locality, which makes it possible to model the troops' military actions. Conditions are also provided to form the so-called **geo-spatial information,** representing a set of various maps, aviation and space images, and intelligence data.

The classification of RS Earth satellites is shown in Fig. 1.

Accounting for the great information potentialities of the satellites *Quick Bird-2* and *Ikonos-2* featuring maximum resolution of 0,6 m and 0,8 m accordingly, in 2003, the National Ocean and Atmosphere Administration (NOAA), USA, provided a license to the companies Space Imaging and Digital Globe for the construction of satellites featuring resolution of up to 0,25 m. Buying and use of such fine-detail images by any state is of crucial importance for defence, security, economy, ecology, as well as for the successful conducting of a number of humanitarian and rescue operations.

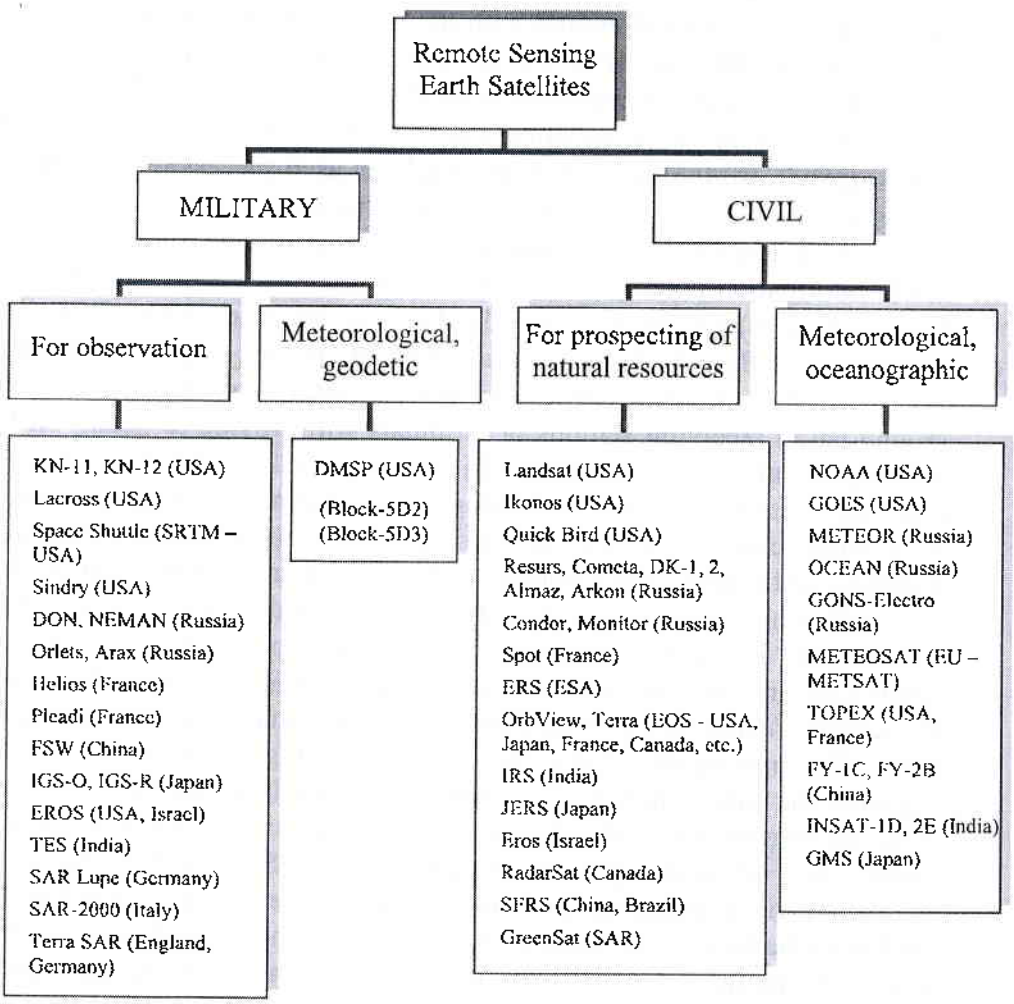

Fig. 1 Classification of RS Earth satellites

Experts believe that, by 2006, about 70% of the space image market will account for products featuring resolution of 1 m or better. Thus, in the beginning of the XXI-st century, the division of the major space states' programmes in the field of RSSS and in other fields into civil and military is only provisional, whereby the gap between the two types is decreasing continuously.

Accounting for the above-mentioned tendencies and for space's leading role in the struggle for information superiority, a number of countries having no potential of their own to launch and maintain Earth

satellites are establishing and using to the benefit of their national security the so-called **"space segment"**. It is based on the information obtained from various RSSSs, global satellite navigation systems, and satellite communication systems which, upon being received at the ground-based stations, subject to dedicated processing and analysis, is submitted to the appropriate customers.

The material basis for space monitoring may be a mobile satellite image receiving station receiving information from satellites with electronic-optic and radiolocation sensors. An example of such station is the Dutch mobile receiving station RAPIDS, which was demonstrated in September, 2000, in Sofia and which features satisfactory characteristics and relatively low price.

Thus, with such a station available, the information from various RS Earth satellites will be fed to the appropriate users nearly on-line, in various climatic conditions, and various times of the day, which requires the use of dedicated software and modern GIS technologies during its processing at the ground-based component.

The establishment of the space segment will make it possible to obtain global, precise, and operative information for the region which is possible only through space monitoring.

The practical implementation of this approach will make it possible to resolve important defence-related problems of the country. The State and army early warning system will be elevated to a new, modern level, providing for monitoring of possible critical situations within and outside the country. Such information will assist greatly adequate decision-taking on the part of the State and military government. If the space information for the region is of sufficient size, trustworthy, and fed nearly on-line, this will speed up the "information-decision-action" cognitive cycle. The latter will be accomplished sooner than the traditional circumstance-related-information acquisition cycle, which will make it possible to outrun the opponent in applying active force and technique.

Digital cartography and GIS construction will be elevated to a new, modern level, too. Digital modelling and various types of simulation will be applied successfully in solving a wide range of defence tasks.

The nearly on-line use of fine-detail images will also enhance the solving of a number of tasks related with state security. Among them, the most topical ones currently are prevention of terrorist acts using transport technique, monitoring and identification of various objects, early detection of fires and floods, identification of earthquakes.

The considered topic's increased importance to defence, security, infrastructure, power engineering, ecology, agriculture, and other areas, coupled with the fact that now no single institution or organization has in its disposition enough funds to buy dedicated monitoring and professionals training equipment call for establishment of a sovereign National Space Information Centre to receive information from satellites for remote sensing, navigation, communication, and meteoprovision. The major nowadays users of the space monitoring system's information are the Ministry of Defence (MoD), the Ministry of Interior (MoI), the State Civil Protection Agency (SCPA), the Ministry of Agriculture and Forests (MoAF), the Ministry of Transport and Communications (MoTC), the Ministry of Environment and Water (MoEW), the Ministry of Power Engineering and Energy Resources (MoPWER), the Ministry of Regional Development and Town Planning (MoRDTP), the Bulgarian Academy of Sciences (BAS), the Bulgarian Red Cross (BRC) etc.

The structure and the human resource of the proposed sovereign National Space Information Centre will depend on the class of the dedicated equipment to be bought and its configuration, on the pertaining hardware and software, as well as on the commitment of the institutions and organizations intending to use the received space information. Accounting for the progress of space technologies, especially during the recent 10 years, the Centre might comprise a ground-based station receiving and processing information from RS Earth satellites, image formation station, communication-information unit with communication terminals for the satellite communication and meteorological systems, analysis and operative coordination department, and service section. The Centre's staff may amount to 25-30 people.

The accomplishment of this approach will provide information superiority to the State and military government under the conditions of various crises or potential military conflicts.

In peace times, the global space monitoring of the area circumstances will update the information provision of important economic or ecological spheres. The efficiency of a number of humanitarian and rescue operations performed by land or sea will be improved.

Modern information medium is built on space monitoring information. The space sector supplementing traditional information structure increases substantially the information field, velocity, precision, and quality of information processes.

The global space monitoring of the circumstances in the region fosters the role enhancement of the preventive factor in national security and the successful management of crises of various nature.

Based on the performed analysis, as well as on the obvious tendencies for implementing space technologies in this field, since 1997 until nowadays, we have continuously proposed to the military and political government of the Bulgarian Army to review the idea for a National Aerospace Information Centre.

Hereunder, the reader will find enclosed the last proposal to the MoD, slightly abridged:

Offer for Establishment of a Space Coordination Centre at the Council of Ministers of the Republic of Bulgaria

Accounting for the increasing role of space in armed struggle, information struggle including, as well as of space information commercialization process which started since the middle of the 90-ies of the XX-th century, in 1997, some leading scientists from the Space Research Institute, BAS, and the *G. S. Rakovski* Military Academy elaborated and forwarded to the Head of the General Staff of the Bulgarian Army a proposal for establishment of a Military-Space Coordination Centre (MSCC) at the BA. The basic idea of the proposal was to establish and operate **a space segment of the BA**, where the required space information for the region and the country will be received from **satellites of various destination** to be then processed, analyzed, and coordinated with the appropriate users for the purposes of a wide range of tasks in military affairs and in other spheres, inclusive of providing for humanitarian and rescue operations. Moreover, accounting for the experience of the MoD and the BA in using navigation, communication, and meteorological satellites, as well as in the field of satellite geodesy and cartography, it was suggested that the space segment be coordinated with the appropriate users and **images** of the country and the region from remote sensing Earth satellites (RSES). The experience of a number of European and other countries from the end of the XX-th century shows that the information supplied by these satellites for certain consideration is characterized by its ready access, global nature, image resolution of the order of a couple of meters, and where a receiving satellite station is available, operativeness. Images with the mentioned characteristics may provide the State and military government with **information superiority in the conditions of various crises or possible military conflicts.**

As a result of a series of organized events of various nature, in April 1998, a Memorandum was elaborated suggesting to establish an MSCC at the BA as a relatively sovereign subsystem of the National Space Information Centre. It was pointed out that the establishment of the MSCC at the BA should comply with the stages of the National Space Programme.

During 1998-2004, some individual activities were carried out on this topic, both at scientific fora, as well as political ones. Thus, for instance, in September 2000, in Sofia, demonstrations of a Dutch mobile station for receiving of satellite images (RAPIDS) were organized as well as a Bulgarian-Dutch seminar on the use and prospects for development of remote-sensing-of-the-Earth technologies. The conclusion was made that the RAPIDS system may serve as a material basis of the National Space Information Centre.

In 2001, in Sofia, on the invitation of the Standing Committee for Population Protection against Disasters, Accidents, and Catastrophes, and the State Civil Protection Agency, the potentialities of the Centre for Receiving and Analysis of Space Information at the Ministry of Emergency Situations of Russia were discussed, which is intended primarily for early detection of fires and floods, and for earthquake identification.

During the considered period (1998-2004), space information centres were established in Israel, Turkey, and Greece, the first two of them belonging to the system of military institutions. This confirmed the actuality and advisability of the offer from 1997 for establishment of a MSCC at the BA.

During the period from 1998 to 2003, the Interinstitutional Committee on Space Research at the Council of Ministers of the Republic of Bulgaria failed to establish a National Space Information Centre.

Meanwhile, the need of establishing such a centre increased greatly after the large-scale fires which flared up during the recent years in some mountainous and field regions of the Republic of Bulgaria. On behalf of the State Civil Protection Agency, in November 2003, the intention was expressed to establish a **Space Monitoring Centre** to receive satellite images at times of fires, floods, or earthquakes. It was suggested that this Space Monitoring Centre be subordinate to the Council of Ministers, so that the information might be used by all institutions.

The juxtaposing of the tasks assigned to the Space Monitoring Centre with those of the MSCC at the BA proposed in 1997 reveals that the tasks related with remote sensing of disasters and accidents constitute only one component and function of the MSCC at the BA, namely the one related with assessment of regional ecosystems. Moreover, at this stage, the

struggle to mitigate disasters, accidents, and catastrophes is **one of the BA's missions**, whereas experts in satellite image processing may be found in BAS and the Military-Topographic Office of the BA. The experts from the latter were educated at the Remote Sensing Development Centre of the French Space Agency.

Judging from the distance of time, i.e. more than six years after the submission of the proposal for establishment of a MSCC at the BA, the conclusion may me made that this proposal is still in line with the world tendency from the end of the XX-th century for establishment of **unified satellite information systems** for remote sensing, navigation, communication, and meteoprovision.

The implementation of **space-based technologies** in the BA will make it possible to overcome a great part of the shortcomings and restrictions of traditional ground-based technologies related mostly with observation, communication, and navigation.

Space-based technologies will provide for organization of a **modern early warning system** in the country, which will be in line with the new missions and tasks of the BA, including those outside the territory of the Republic of Bulgaria.

Accounting for the foregoing, as well as for the possibilities to sell space information to some countries of the region, it may be expected that the funds invested to buy a ground-based station for receiving of satellite images and other dedicated equipment (estimated price of about one million US dollars) will be restored to the State.

Accounting for the increased importance of the considered problems to defence, security, infrastructure, ecology, agriculture, and other fields, as well as for the fact that, at this stage, no institution or organization has in its disposition the required funds to buy the appropriate satellite equipment and to pay for adequate expert training necessitates to establish a **Space Coordination Centre (SCC)** for the information obtained from satellites for remote sensing, navigation, communication, and meteoprovision for the needs of users from various institution and organizations (MoD, MoI, SCPA, MoAF, MoTC, MoEW, BRC etc.).

It is expedient to establish and operate a SCC as a sovereign unit at the Council of Ministers of the Republic of Bulgaria.

The formation of a SCC may provide for **monitoring of possible critical situations in the country and the region** and assist taking appropriate decisions.

The structure and staff of the SCC will depend on the level of the bought dedicated equipment and its configuration, the respective hardware

and software, as well as the participation rate of the institutions and organizations as users of the received space information. Accounting for the progress in space technologies during the elapsed period, the SCC may comprise a ground-based station for receiving and processing of the information acquired by RS Earth satellites, an image-formation station, a communication-information unit with terminals for connection with the satellite communication and meteorological systems, an analysis and operative coordination department, and a service sector. The expedient establishment of an SCC, compatible with those of the neighbouring countries and allies, will turn into a preventive factor for national security; will elevate to a modern level the early warning system of the State and the army and will update the information provision of important spheres in economy, ecology, and the humanitarian field.

Based on the foregoing,

WE SUGGEST:

1. To initiate the establishment of a Space Coordination Centre as a sovereign unit at the Council of Ministers of the Republic of Bulgaria.
2. During the formation of the Space Coordination Centre, to avail of the experience, potential and infrastructure of the MoD, the BA, and the BAS, while inscribing the Centre onto the list of the country's management systems at times of crises.
3. To provide funding for the Space Coordination Centre in the budget for 200_, to be allocated specifically for this purpose by a Resolution of the Council of Ministers, with proportional participation of the leading institutions and organizations in the use of space information.
4. To supply the key elements of the organizational structure of the Space Coordination Centre in 200_, in advance of staff education, buying of dedicated systems, hardware and software, providing for receiving, processing, analysis, and coordination of space information among users.

References:

1. Aerospace America, 2003–2004.
2. Space News, 2003–2004.
3. Г е ц о в П. С., П е н е в П. Б. Ролята на аерокосмическите технологии и на военния фактор за националната сигурност, Aerospace Research in Bulgaria, София, БАН, кн. 17, 2003 г.
4. Новости космонавтики, кн. 1, 2004 г.
5. П е н е в П. Б. и др. Космосът във военното дело, София, ВИ, 2003 г.

НЯКОИ ВЪЗМОЖНОСТИ ЗА ИЗПОЛЗВАНЕТО НА АЕРОКОСМИЧЕСКАТА ИНФОРМАЦИЯ В ОБЛАСТТА НА НАЦИОНАЛНАТА СИГУРНОСТ И ОТБРАНАТА

Петър Гецов, Павел Пенев

Резюме

Формулирани са съвременните тенденции, свързани с използването на дистанционните методи и системи за изследване на Земята от Космоса. Посочено е мястото на комерсиалните спътници за дистанционно сондиране с двойно предназначение с възможности за космически мониторинг в условията на Р. България. В обобщен вид са дефинирани задачите в областта на отбраната и сигурността, решавани с помощта на космическия сегмент.

Предлага се структура на надведомствен Национален център за космическа информация.

Bulgarian Academy of Sciences. Space Research Institute.
Aerospace Research in Bulgaria. 19, 2005, Sofia

THIN VISCOUS ELLIPTICAL ACCRETION DISCS WITH ORBITS SHARING A COMMON LONGITUDE OF PERIASTRON. DYNAMICAL EQUATION FOR INTEGER VALUES OF THE POWERS IN THE VISCOSITY LAW

Dimitar Dimitrov

Space Research Institute, Bulgarian Academy of Sciences

Abstract

We consider a model of thin stationary viscous accretion disc around a stellar mass compact object developed by Lyubarskij et al. [3]. The orbits of the gaseous particles are ellipses which eccentricities may vary from inner to the outer parts of the disc and which apse lines are in line with each other. The accepted viscosity coefficient η obeys the relation $\eta = \beta \Sigma^n$ with Σ - surface density of the accretion disc, β and n - constants. Our considerations are dealing with the cases when the exponent n takes integer values, namely $n = -1, 0, 1, 2$ and 3, which lie in the physically suitable range. We derive in an explicit form the auxiliary functions introduced by Lyubarskij et al. For two values of $n = -1$ and $n = +2$ we also write the explicit form of the dynamical equation governing the radial structure of the disc. For the other cases we limit us with graphical representations of the ratios of the coefficients of this equation.

Keywords: *accretion discs.*

1. Introduction

There are both observational and theoretical grounds to believe that the circular orbits of fluid particles in accretion discs are not the only possible cases which may be considered in treatment of accretion phenomena. The most widespread applications of using eccentric orbits for description and explanation of the observed astrophysical events are the superhumps in the light-curves of dwarf-nova cataclysmic variables like SU UMa stars. This type of binary stars consists of a white dwarf, with a gaseous accretion disc

around it, and a main sequence star which supplies matter to the disc through the inner Lagrangian point L_1. The internal instability of the disc, caused by viscosity stresses, as well as the tidal influence of the companion star, are the reasons determining the elongated (elliptical) shape of the disc. Its dimensions also vary during different stages of the outburst events depending on the total accumulated mass and the thermal conditions. The mass transfer stream from the companion star strikes the outer parts of the accretion disc at the so-called "hot-spot" region. But nevertheless, it is not expected the dynamics of the accretion disc to be significantly affected by that perturbation. For example, time-resolved spectroscopy is applied to study the nova-like variable UU Aqu. Using eclipse mapping techniques, spatially resolved spectra of its accretion disc as a function of the distance from the disc centre were obtained. Consideration of the data suggests that the asymmetric structure in the outer disc (previously identified as a bright spot) may be considered as a signature of an elliptical disc, similar to those in SU UMa stars during superoutbursts [1]. However, it is worth noting that this interpretation is not the only possible one. The non-axisymmetric features observed in the discs of dwarf-novae during the outburst events are often considered to be spiral shocks, but this explanation strikes with some problems: the natural site of the wave excitation lies outside the Roche lobe, the accretion disc must be "hot", the treatments of wave propagation does not take into account the vertical disc structure [2]. Consequently, the elliptical shape of the discs in these cases remains a plausible explanation of the observed features of dwarf-nova outbursts.

During the recent years, increasing interest has been devoted to the problem of formation of planetary systems around solar-like young stellar systems. Here, the accretion discs, from which the planets generate, may consist not only of gaseous component, but be predominantly composed of solid dust particles and rocks, and have a complex radial structure. An accreting protoplanet that is embedded into the disc may clear an annulus about its orbital path. Numerous observational efforts have lead to the discovery of many extrasolar planet systems (the number of planets approaches one hundred at present time) and, in the majority of cases, the eccentricities of the planet orbits were evaluated with sufficient accuracy. These estimates definitely lead to the conclusion that, as a rule, the extrasolar planets have orbits with considerable eccentricities - evidence that the progenitor accretion discs were also with elliptical shape.

The large variety of possibilities for the parameters of the systems "accretion disc + binary star" suggests, in turn, a large number of theoretical models for these astrophysical systems. It is not always possible to solve

analytically problems arising in this way and numerical approaches are needed to find the solutions of the equations describing the discs dynamics. In this paper, we focus on a model of elliptical accretion disc developed by Lyubarskij et al. [3]. Our aim is to obtain in explicit form the dynamical equation describing the properties of the accretion disc around a stellar mass compact object for some particular values of the viscosity law parameters. An important specific feature of this model is that the apse lines of all particle orbits are in line with each other. This condition, imposed "by hand", may be removed, as it has been done in more recent studies of fluid dynamics of eccentric discs by Ogilvie, by using complex values of disc eccentricity [4]. But this complication makes it much more difficult to find an analytical solution to the dynamical equation of the disc. Our main purpose is to use an analytical approach to the considered problem. We restrict ourselves to the more simple task based on the model of Lyubarskij et al. [3], although the accuracy of this description (in opposite to the model of Ogilvie [4]) is not enough suitable to make precise tests of the theory by observations. Nevertheless, we hope that the fully analytical treatment of the accretion flows in such simplified cases may be useful in the attempts to solve analytically (or to determine the limits of the analytical approach) the more complicated and realistic models of accretion discs, which are appropriate for evaluating the model parameters from direct comparison with observations.

2. Accretion Disc Model

In what follows, we shall use the notations and approach according to the paper of Lyubarskij et al. [3]. The eccentric disc model, considered in this paper, includes also the non-stationary regime, but we shall limit ourselves only to the stationary picture. The theory represents, to some extent, a generalization of the standard thin α-disc theory to the case of elliptical streamlines of gaseous particles. The accepted viscosity law describes a proportionality between the viscosity coefficient η and the n-th power of disc surface density Σ: $\eta = \beta\Sigma^n$, where β and n are constants. Our intention is to write explicitly and to investigate the possibility for exact analytical solution of the dynamical equation, governing the radial structure of the accretion disc, for *integer* values of the power n, namely for n = -1, 0, 1, 2, and 3. These selections are of astrophysical interest and the implications for non-integer values of n may possibly be obtained through an interpolation between the data for these integer numbers. In the considered model, the eccentricity e of the particle orbits may vary under the transition from the inner to the outer parts of the disc. For every elliptical orbit, the dependence of its eccentricity e on the focal parameter p ($p = b^2/a$; a and b are the major

and the minor semiaxes), giving the "size" of the ellipse, is determined by the following dynamical equation [3]:

(1) $[\, Y\,(\partial Z/\partial \dot{e}) - Z\,(\partial Y/\partial \dot{e})\,]\,\ddot{e} + [\, Y\,(\partial Z/\partial e) - Z\,(\partial Y/\partial e) - Y^2 e\,]\,\dot{e} + Y\,[\,(3/2)W - Z - (1/2)(1 - e^2)\,Y\,] = 0\,.$

This is a second order ordinary differential equation, where the dot $(\cdot)$ denotes differentiation with respect to the variable $u \equiv ln\ p$ and it is taken into account that $e = e\,(p, n)$. The analytical expressions for auxiliary functions Y, Z and W (averaged over the azimuthal angle φ) and the integrals I_{0-}, I_{0+} and I_k (k = 0, 1,...,4) are given in a previous paper [5], devoted to the investigation of equation (1). All these quantities are functions of e, $\dot{e} \equiv \partial e/\partial u$ and n. In the present study, we have computed in explicit form the integrals I_{0-} , I_{0+} and I_k (k = 0, 1,...,4), and correspondingly Y, Z and W for the above mentioned integer values of the exponent n. This is done by the use of some already tabulated integrals ([6], formulae 858.525 and 858.535) and consequential application of the derived results for the next steps of the evaluations. We remind here that, according to Lyubarskij et al. [3], the negative values of the eccentricity e simply imply that the periastron of the ellipse lies on the negative part of the abscissa axis as opposite to the case of positive values of e, when its abscissa is positive. We stress again that the considered model of particle orbits includes only apse lines in line with each other, i.e., all ordinates of the periastron points are equal to zero. We obtain the following results:

Case $n = -1$

(2a) $I_0\,(e, \dot{e}, n = -1) = \pi\,(1 - e^2)^{-5/2}\,(2 + e^2)\,,$

(2b) $I_1\,(e, \dot{e}, n = -1) = -3\pi\,e\,(1 - e^2)^{-5/2}\,,$

(2c) $I_2\,(e, \dot{e}, n = -1) = \pi\,(1 - e^2)^{-5/2}\,(1 + 2e^2)\,,$

(2d) $I_3\,(e, \dot{e}, n = -1) = \pi\,(1 - e^2)^{-5/2}\,e^{-3}\,[-2 + 5e^2 - 6e^4 + 2(1 - e^2)^{5/2}]\,,$

(2e) $I_4\,(e, \dot{e}, n = -1) = 3\pi\,(1 - e^2)^{-5/2}\,e^{-4}\,[\,2 - 5e^2 + 4e^4 - 2(1 - e^2)^{5/2}\,]\,,$

(2g) $I_{0+}\,(e, \dot{e}, n = -1) = \pi\,(1 - e^2)^{-5/2}\,[1 - (e - \dot{e})^2]^{-1/2}\,\dot{e}^{-3}\,\{-2e\,(1 - e^2)\,\dot{e}\,(e - \dot{e}) ? [1 - (e - \dot{e})^2]^{1/2} + 2e\,(1 - e^2)^2\,(e - \dot{e})^2\,[1 - (e - \dot{e})^2]^{1/2} - 2(1 - e^2)^{5/2}\,(e - \dot{e})^3 + e\,(2 + e^2)\,\dot{e}^2\,[1 - (e - \dot{e})^2]^{1/2}\}\,,$

(2h) $I_{0-}\,(e, \dot{e}, n = -1) = \pi\,(1 - e^2)^{-7/2}\,(2 + 3e^2)\,.$

Case $n = 0$

(3a) $I_0(e, \dot{e}, n = 0) = 2\pi (1 - e^2)^{-3/2} [1 - (e - \dot{e})^2]^{-1/2} \dot{e}^{-2} \{ e \dot{e} [1 - (e - \dot{e})^2]^{1/2} - e (e - \dot{e}) \; ? (1 - e^2) [1 - (e - \dot{e})^2]^{1/2} + (e - \dot{e})^2 (1 - e^2)^{3/2} \}$,

(3b) $I_1(e, \dot{e}, n = 0) = 2\pi (1 - e^2)^{-3/2} [1 - (e - \dot{e})^2]^{-1/2} \dot{e}^{-2} \{ (e - \dot{e} - e^3) [1 - (e - \dot{e})^2]^{1/2} - (e - \dot{e}) (1 - e^2)^{3/2} \}$,

(3c) $I_2(e, \dot{e}, n = 0) = 2\pi (1 - e^2)^{-3/2} [1 - (e - \dot{e})^2]^{-1/2} \dot{e}^{-2} \{ (-1 + e^2 + e \dot{e}) ? [1 - (e - \dot{e})^2]^2 + (1 - e^2)^{3/2} \}$,

(3d) $I_3(e, \dot{e}, n = 0) = 2\pi (1 - e^2)^{-3/2} [1 - (e - \dot{e})^2]^{-1/2} e^{-2} \dot{e}^{-2} (e - \dot{e})^{-1} \{ -e^2 (1 - e^2)^{3/2} + [e^2 - e^4 - e^3 \dot{e} - \dot{e}^2 + 2e^2 \dot{e}^2 + \dot{e}^2 (1 - e^2)^{3/2}] [1 - (e - \dot{e})^2]^{1/2} \}$,

(3e) $I_4(e, \dot{e}, n = 0) = 2\pi (1 - e^2)^{-3/2} [1 - (e - \dot{e})^2]^{-1/2} e^{-3} \dot{e}^{-2} (e - \dot{e})^{-2} \{ e^3 (1 - e^2)^{3/2} + (-e^3 + e^5 + e^4 \dot{e} + 3e \dot{e}^2 - 5e^3 \dot{e}^2 - 2\dot{e}^3 + 3e^2 \dot{e}^3) [1 - (e - \dot{e})^2]^{1/2} + (-3e \dot{e}^2 + 2\dot{e}^3) ? (1 - e^2)^{3/2} [1 - (e - \dot{e})^2]^{1/2} \}$,

(3g) $I_{0+}(e, \dot{e}, n = 0) = 2\pi (1 - e^2)^{-3/2} [1 - (e - \dot{e})^2]^{-3/2} \dot{e}^{-3} \{ (2e^3 - 2e^5 - 3e^2 \dot{e} + 8e^4 \dot{e} - 12e^3 \dot{e}^2 + \dot{e}^3 + 8e^2 \dot{e}^3 - 2e \dot{e}^4) (1 - e^2)^{3/2} + (-2e^3 + 2e^5 + 3e^2 \dot{e} - 2e^4 \dot{e}) ? [1 - (e - \dot{e})^2]^{3/2} \}$,

(3h) $I_{0-}(e, \dot{e}, n = 0) = \pi (1 - e^2)^{-5/2} [1 - (e - \dot{e})^2]^{-1/2} \dot{e}^{-3} \{ (2e^3 - 4e^5 + 2e^7 - 6e^2 \dot{e} + 10e^4 \dot{e} - 4e^6 \dot{e} + 6e \dot{e}^2 - 5e^3 \dot{e}^2 + 2e^5 \dot{e}^2) [1 - (e - \dot{e})^2]^{1/2} - 2(e - \dot{e})^3 (1 - e^2)^{5/2} \}$.

Case $n = +1$

(4a) $I_0(e, \dot{e}, n = +1) = 2\pi (e - \dot{e})^{-1/2} [1 - (e - \dot{e})^2]^{-3/2} \dot{e}^{-2} \{ (-e^2 + e^4 - 3e^3 \dot{e} + \dot{e}^2 + 3e^2 \dot{e}^2 - e \dot{e}^3) (1 - e^2)^{1/2} + e^2 [1 - (e - \dot{e})^2]^{3/2} \}$,

(4b) $I_1(e, \dot{e}, n = +1) = 2\pi (1 - e^2)^{-1/2} [1 - (e - \dot{e})^2]^{-3/2} \dot{e}^{-2} \{ [e - (e - \dot{e})^3] (1 - e^2)^{1/2} - e [1 - (e - \dot{e})^2]^{3/2} \}$,

(4c) $I_2(e, \dot{e}, n = +1) = 2\pi (1 - e^2)^{-1/2} [1 - (e - \dot{e})^2]^{-3/2} \dot{e}^{-2} \{ (-1 + e^2 - 3e \dot{e} + 2\dot{e}^2) ? (1 - e^2)^{1/2} + [1 - (e - \dot{e})^2]^{3/2} \}$,

(4d) $I_3(e, \dot{e}, n = +1) = 2\pi (1 - e^2)^{-1/2} [1 - (e - \dot{e})^2]^{-3/2} e^{-1} \dot{e}^{-2} (e - \dot{e})^{-2} ? \{ -(e - \dot{e})^2 [1 - (e - \dot{e})^2]^{3/2} + [e^2 - e^4 - 2e \dot{e} + 5e^3 \dot{e} - 7e^2 \dot{e}^2 + 3e \dot{e}^3 + \dot{e}^2 [1 - (e - \dot{e})^2]^{3/2}] (1 - e^2)^{1/2} \}$,

(4e) $I_4(e, \dot{e}, n = +1) = 2\pi (1 - e^2)^{-1/2} [1 - (e - \dot{e})^2]^{-3/2} e^{-2} \dot{e}^{-2} (e - \dot{e})^{-3} \{ (e - \dot{e})^3 ? [1 - (e - \dot{e})^2]^{3/2} + (-e^3 + e^5 + 3e^2 \dot{e} - 6e^4 \dot{e} + 9e^3 \dot{e}^2 - 4e^2 \dot{e}^3) (1 - e^2)^{1/2} + (-3e \dot{e}^2 + \dot{e}^3) (1 - e^2)^{1/2} [1 - (e - \dot{e})^2]^{3/2} \}$,

(4g) $I_{0+}(e, \dot{e}, n = +1) = \pi (1 - e^2)^{-1/2} [1 - (e - \dot{e})^2]^{-5/2} \dot{e}^{-3} \{ (-2e^3 + 4e^5 - 2e^7 - 10e^4 \dot{e} + 10e^6 \dot{e} + 5e^3 \dot{e}^2 - 20e^5 \dot{e}^2 + 2\dot{e}^3 + 5e^2 \dot{e}^3 + 20e^4 \dot{e}^3 - 5e \dot{e}^4 - 10e^3 \dot{e}^4 + \dot{e}^5 + 2e^2 \dot{e}^5) ? (1 - e^2)^{1/2} + 2e^3 [1 - (e - \dot{e})^2]^{5/2} \}$,

(4h) $I_{0-}(e, \dot{e}, n = +1) = 2\pi (1 - e^2)^{-3/2} [1 - (e - \dot{e})^2]^{-3/2} \dot{e}^{-3} \{ (2e^3 - 2e^5 - 3e^2 \dot{e} + 8e^4 \dot{e}$

$- 12e^3 \dot{e}^2 + \dot{e}^3 + 8e^2 \dot{e}^3 - 2e \dot{e}^4) (1 - e^2)^{3/2} + (- 2e^3 + 2e^5 + 3e^2 \dot{e} - 2e^4 \dot{e})$
$? [1 - (e - \dot{e})^2]^{3/2} \} .$

Case $n = + 2$

(5a) $I_0 (e, \dot{e}, n = + 2) = \pi [1 - (e - \dot{e})^2]^{- 5/2} [2 + (e - \dot{e})^2] ,$

(5b) $I_1 (e, \dot{e}, n = + 2) = - 3\pi (e - \dot{e}) [1 - (e - \dot{e})^2]^{- 5/2} ,$

(5c) $I_2 (e, \dot{e}, n = + 2) = \pi [1 + 2(e - \dot{e})^2] [1 - (e - \dot{e})^2]^{- 5/2} ,$

(5d) $I_3 (e, \dot{e}, n = + 2) = \pi [1 - (e - \dot{e})^2]^{- 5/2} (e - \dot{e})^{- 3} \{ - 2 + 5e^2 - 6e^4 - 10e \dot{e} + 24e^3 \dot{e} + 5\dot{e}^2 - 36e^2 \dot{e}^2 + 24e \dot{e}^3 - 6\dot{e}^4 + 2[1 - (e - \dot{e})^2]^{5/2} \} ,$

(5e) $I_4 (e, \dot{e}, n = + 2) = \pi [1 - (e - \dot{e})^2]^{- 5/2} (e - \dot{e})^{- 4} \{ 6 - 15e^2 + 12e^4 + 30e \dot{e} - 48e^3 \dot{e} - 15\dot{e}^2 + 72e^2 \dot{e}^2 - 48e \dot{e}^3 + 12 \dot{e}^4 - 6 [1 - (e - \dot{e})^2]^{5/2} \} ,$

(5g) $I_{0+} (e, \dot{e}, n = + 2) = \pi [2 + 3(e - \dot{e})^2] [1 - (e - \dot{e})^2]^{- 7/2} ,$

(5h) $I_{0-} (e, \dot{e}, n = + 2) = I_{0+} (e, \dot{e}, n = + 1) ,$ (see formula (4g)) .

Case $n = + 3$

(6a) $I_0 (e, \dot{e}, n = + 3) = \pi [1 - (e - \dot{e})^2]^{- 7/2} (2 - e^2 - e^4 - 2e \dot{e} + 3e^3 \dot{e} + 3\dot{e}^2 - 3e^2 \dot{e}^2 + e \dot{e}^3) ,$

(6b) $I_1 (e, \dot{e}, n = + 3) = \pi [1 - (e - \dot{e})^2]^{- 7/2} (e - \dot{e})^{- 1} (- 3e^2 + 3e^4 + 7e \dot{e} - 8e^3 \dot{e} - 4\dot{e}^2 + 6e^2 \dot{e}^2 - \dot{e}^4) ,$

(6c) $I_2 (e, \dot{e}, n = + 3) = \pi [1 - (e - \dot{e})^2]^{- 7/2} (1 + e^2 - 2e^4 - 5e \dot{e} + 6e^3 \dot{e} + 4\dot{e}^2 - 6e^2 \dot{e}^2 + 2e \dot{e}^3) ,$

(6d) $I_3 (e, \dot{e}, n = + 3) = \pi [1 - (e - \dot{e})^2]^{- 7/2} (e - \dot{e})^{- 4} \{ - 2e + 7e^3 - 11e^5 + 6e^7 - 14e^2 \dot{e} + 47e^4 \dot{e} - 34e^6 \dot{e} + 7e \dot{e}^2 - 78e^3 \dot{e}^2 + 78e^5 \dot{e}^2 + 62e^2 \dot{e}^3 - 90e^4 \dot{e}^3 - 23e \dot{e}^4 + 50e^3 \dot{e}^4 + 3\dot{e}^5 - 6e^2 \dot{e}^5 - 6e \dot{e}^6 + 2\dot{e}^7 + 2e [1 - (e - \dot{e})^2]^{7/2} \} ,$

(6e) $I_4 (e, \dot{e}, n = + 3) = \pi [1 - (e - \dot{e})^2]^{- 7/2} (e - \dot{e})^{- 5} \{ 6e - 21e^3 + 27e^5 - 12e^7 + 2\dot{e} + 35e^2 \dot{e} - 100e^4 \dot{e} + 64e^6 \dot{e} - 7e \dot{e}^2 + 130e^3 \dot{e}^2 - 132e^5 \dot{e}^2 - 7\dot{e}^3 - 60e^2 \dot{e}^3 + 120e^4 \dot{e}^3 - 5e \dot{e}^4 - 20e^3 \dot{e}^4 + 8\dot{e}^5 - 48e^2 \dot{e}^5 + 36e \dot{e}^6 - 8\dot{e}^7 + (- 6e - 2\dot{e}) [1 - (e - \dot{e})^2]^{7/2} \} ,$

(6g) $I_{0+} (e, \dot{e}, n = + 3) = (\pi/4) [1 - (e - \dot{e})^2]^{- 9/2} (e - \dot{e})^{-1} (8e + 4e^3 - 12e^5 - 8\dot{e} - 32e^2 \dot{e} + 45e^4 \dot{e} + 52e \dot{e}^2 - 60e^3 \dot{e}^2 - 24\dot{e}^3 + 30e^2 \dot{e}^3 - 3 \dot{e}^5) ,$

(6h) $I_{0-} (e, \dot{e}, n = + 3) = \pi [2 + 3(e - \dot{e})^2] [1 - (e - \dot{e})^2]^{- 7/2} .$

The above formulae must be considered under the restrictions $|e| < 1$, $|\dot{e}| < 1$ and $|e - \dot{e}| < 1$, which from a physical point of view guarantee that the trajectories of the gas particles are bounded (i.e., are ellipses) and do not intersect with each other. From a mathematical point of view these conditions also mean that the singularities in the expressions for metric, radius vector,

Keplerian velocity and shear tensor (see [3], Appendix A), as well as in the integrals I_{0-}, I_{0+}, I_k (k = 0, 1, ... , 4) are avoided. It should be pointed out that in some cases values $e = 0$, $\dot{e} = 0$ or $(e - \dot{e}) = 0$ may occur in the denominators of the expressions (2) - (6). Nevertheless, the integrals can also be analytically computed (even more easily !) by direct substitution of the so mentioned zero values into the original definitions of the integrals. These results may be compared with the limits derived from relations (2) - (6) when e, $\dot{e}$ or $(e - \dot{e})$ approach zero. The later calculations are based on the application of the L'Hospital's rule for solving of uncertainties of the type 0/0. In the both cases the final results are the same and consequently, we do not need to trouble about the nullification of the denominators - the transitions of the expressions (2) - (6) to the singular values of their arguments are continuous.

3. Auxiliary Functions and Dynamical Equation

According to paper [5], where the expressions for $Y(e, \dot{e}, n)$, $Z(e, \dot{e}, n)$ and $W(e, \dot{e}, n)$ are given in explicit form as linear combinations of the integrals I_k $(e, \dot{e}, n)$, (k = 0, 1, ... , 4) (see formulae (2) - (4) from [5]). Having already the results (2) - (6) for integer n, we are in a position to compute $Y(e, \dot{e}, n)$, $Z(e, \dot{e}, n)$ and $W(e, \dot{e}, n)$ in a straightforward manner. There is not indispensable need to use the available linear relations between integrals I_{0-}, I_{0+} and I_k, (k = 0, 1, ..., 4), in order to reduce the complexity of the initial formulae and, correspondingly, the intermediate calculations. Such simplifications are very desirable when the more general considerations of non-integer n are examined, when manifest evaluations of I_k (k = 0, 1, ... , 4) like (2) - (6) are not available. We shall directly write here the analytical form of the auxiliary functions $Y(e, \dot{e}, n)$, $Z(e, \dot{e}, n)$ and $W(e, \dot{e}, n)$ for $n = -1, 0, \ldots, 3$.

Case $n = -1$

(7a) $$3Y(e, \dot{e}, n = -1) = (p/GM)^{-1/2} (1 - e^2)^{-3/2} (3 - 3e^2 + 4e\dot{e}) ,$$

(7b) $$3Z(e, \dot{e}, n = -1) = (p/GM)^{-1/2} (1 - e^2)^{-1/2} [-1 + e^2 - 2e\dot{e} + 4(1 - e^2)^{1/2}]$$

(7c) $$9W(e, \dot{e}, n = -1) = (p/GM)^{-1/2} (1 - e^2)^{-3/2} e^{-2} [e^2 - 2e^4 + e^6 + 4e^3\dot{e} - 4e^5\dot{e} + 24\dot{e}^2 - 24e^2\dot{e}^2 + 4e^4\dot{e}^2 + (8e^2 - 24\dot{e}^2) (1 - e^2)^{3/2}] .$$

Case $n = 0$

(8a) $$3Y(e, \dot{e}, n = 0) = (1 - e^2)^{-1/2} [1 - (e - \dot{e})^2]^{-1/2} \dot{e}^{-1} \{ (- 3e + 3e^3 - \dot{e} - 5e^2\dot{e} + 2e\dot{e}^2) ? (1 - e^2)^{1/2} + (3e - 3e^3 + 4\dot{e} + 2e^2\dot{e}) [1 - (e - \dot{e})^2]^{1/2} \} ,$$

(8b) $3Z(e, \dot{e}, n = 0) = [1 - (e - \dot{e})^2]^{-1/2} \dot{e}^{-1} \{ - e + 2e^3 - e^5 - \dot{e} - 2e^2 \dot{e} + 3e^4 \dot{e} - 2e \dot{e}^2 - 2e^3 \dot{e}^2 + (e - e^3 + 2e^2 \dot{e}) (1 - e^2)^{1/2} [1 - (e - \dot{e})^2]^{1/2} + 4\dot{e} [1 - (e - \dot{e})^2]^{1/2} \}$,

(8c) $9W(e, \dot{e}, n = 0) = (1 - e^2)^{-1/2} [1 - (e - \dot{e})^2]^{-1/2} e^{-1} \dot{e}^{-1} (e - \dot{e})^{-1} \{ (- e^3 + 2e^5 - e^7 + 2e^2 \dot{e} - 8e^4 \dot{e} + 6e^6 \dot{e} + 7e \dot{e}^2 + 2e^3 \dot{e}^2 - 13e^5 \dot{e}^2 + 12e^2 \dot{e}^3 + 12e^4 \dot{e}^3 - 8e \dot{e}^4 - 4e^3 \dot{e}^4) ? (1 - e^2)^{1/2} + (8e^2 \dot{e} - 8e \dot{e}^2 - 8\dot{e}^3) (1 - e^2)^{1/2} [1 - (e - \dot{e})^2]^{1/2} + (e^3 - 2e^5 + e^7 - e^2 \dot{e} + 6e^4 \dot{e} - 5e^6 \dot{e} - 8e \dot{e}^2 + 4e^3 \dot{e}^2 + 8e^5 \dot{e}^2 + 8\dot{e}^3 - 8e^2 \dot{e}^3 - 4e^4 \dot{e}^3) ? [1 - (e - \dot{e})^2]^{1/2} \}$.

Case $n = + 1$

(9a) $3Y(e, \dot{e}, n = + 1) = (p/GM)^{1/2} (1 - e^2)^{-1/2} [1 - (e - \dot{e})^2]^{-3/2} \dot{e}^{-1} \{ (4e - 8e^3 + 4e^5 + 3\dot{e} + 9e^2 \dot{e} - 12e^4 \dot{e} + 2e \dot{e}^2 + 12e^3 \dot{e}^2 - 4\dot{e}^3 - 4e^2 \dot{e}^3) (1 - e^2)^{1/2} + (- 4e + 8e^3 - 4e^5 - 8e^2 \dot{e} + 8e^4 \dot{e} + 4e \dot{e}^2 - 4e^3 \dot{e}^2) [1 - (e - \dot{e})^2]^{1/2} \}$

(9b) $3Z(e, \dot{e}, n = +1) = (p/GM)^{1/2} [1 - (e - \dot{e})^2]^{-3/2} (e - \dot{e})^{-2} \{ - e^2 + 2e^4 - e^6 + 2e \dot{e} - 8e^3 \dot{e} + 6e^5 \dot{e} + 3\dot{e}^2 + 6e^2 \dot{e}^2 - 13e^4 \dot{e}^2 + 4e \dot{e}^3 + 12e^3 \dot{e}^3 - 4\dot{e}^4 - 4e^2 \dot{e}^4 + (4e^2 - 4e^4 - 8e \dot{e} + 16e^3 \dot{e} - 20e^2 \dot{e}^2 + 8e \dot{e}^3) [1 - (e - \dot{e})^2]^{1/2} \}$

(9c) $9W(e, \dot{e}, n = + 1) = (p/GM)^{1/2} [1 - (e - \dot{e})^2]^{-3/2} \{ 1 - 2e^2 + e^4 + 4e \dot{e} - 4e^3 \dot{e} + 4e^2 \dot{e}^2 + (8 - 8e^2 + 16e \dot{e} - 8\dot{e}^2) [1 - (e - \dot{e})^2]^{1/2} \}$.

Case $n = + 2$

(10a) $3Y(e, \dot{e}, n = + 2) = (p/2GM) [1 - (e - \dot{e})^2]^{-5/2} (6 - 12e^2 + 6e^4 + 23e \dot{e} - 23e^3 \dot{e} - 9\dot{e}^2 + 31e^2 \dot{e}^2 - 14e \dot{e}^3)$,

(10b) $3Z(e, \dot{e}, n = + 2) = (p/2GM) [1 - (e - \dot{e})^2]^{-5/2} (e - \dot{e})^{-3} \{- 2e^3 + 6e^5 - 6e^7 + 2e^9 + 6e^2 \dot{e} - 29e^4 \dot{e} + 40e^6 \dot{e} - 17e^8 \dot{e} + 18e \dot{e}^2 + 2e^3 \dot{e}^2 - 78e^5 \dot{e}^2 + 58e^7 \dot{e}^2 - 6\dot{e}^3 + 68e^2 \dot{e}^3 + 28e^4 \dot{e}^3 - 102e^6 \dot{e}^3 - 56e \dot{e}^4 + 74e^3 \dot{e}^4 + 98e^5 \dot{e}^4 + 9\dot{e}^5 - 84e^2 \dot{e}^5 - 49e^4 \dot{e}^5 + 26e \dot{e}^6 + 10e^3 \dot{e}^6 + (8e^3 - 24e^2 \dot{e}) [1 - (e - \dot{e})^2]^{5/2} \}$,

(10c) $9W(e, \dot{e}, n = 2) = (p/2GM) [1 - (e - \dot{e})^2]^{-5/2} (e - \dot{e})^{-3} \{ 2e^3 - 6e^5 + 6e^7 - 2e^9 - 6e^2 \dot{e} + 27e^4 \dot{e} - 36e^6 \dot{e} + 15e^8 \dot{e} + 6e \dot{e}^2 - 44e^3 \dot{e}^2 + 82e^5 \dot{e}^2 - 44e^7 \dot{e}^2 - 18\dot{e}^3 + 70e^2 \dot{e}^3 - 110e^4 \dot{e}^3 + 62e^6 \dot{e}^3 - 86e \dot{e}^4 + 132e^3 \dot{e}^4 - 38e^5 \dot{e}^4 + 39\dot{e}^5 - 142e^2 \dot{e}^5 - e^4 \dot{e}^5 + 92e \dot{e}^6 + 12e^3 \dot{e}^6 - 24\dot{e}^7 - 4e^2 \dot{e}^7 + (16e^3 - 32e^5 + 16e^7 - 48e^2 \dot{e} + 160e^4 \dot{e} - 112e^6 \dot{e} + 48e \dot{e}^2 - 320e^3 \dot{e}^2 + 336e^5 \dot{e}^2 + 288e^2 \dot{e}^3 - 544e^4 \dot{e}^3 - 96e \dot{e}^4 + 496e^3 \dot{e}^4 - 240e^2 \dot{e}^5 + 48e \dot{e}^6) [1 - (e - \dot{e})^2]^{1/2} \}$.

Case $n = + 3$

(11a) $3Y(e, \dot{e}, n = + 3) = (1/2) (p/GM)^{3/2} [1 - (e - \dot{e})^2]^{-7/2} (6 - 18e^2 + 18e^4 - 6e^6 + 30e \dot{e} - 60e^3 \dot{e} + 30e^5 \dot{e} - 7\dot{e}^2 + 65e^2 \dot{e}^2 - 58e^4 \dot{e}^2 - 20e \dot{e}^3 + 50e^3 \dot{e}^3 - 4\dot{e}^4 - 16e^2 \dot{e}^4)$,

(11b) $3Z(e, \dot{e}, n = +3) = (1/2)\,(p/GM)^{3/2}\,[1 - (e - \dot{e})^2]^{-7/2}\,(e - \dot{e})^{-4}\,\{ -2e^4 + 8e^6 - 12e^8 + 8e^{10} - 2e^{12} + 8e^3\,\dot{e} - 46e^5\,\dot{e} + 90e^7\,\dot{e} - 74e^9\,\dot{e} + 22e^{11}\,\dot{e} + 36e^2\,\dot{e}^2 - 43e^4\,\dot{e}^2 - 124e^6\,\dot{e}^2 + 233e^8\,\dot{e}^2 - 102e^{10}\,\dot{e}^2 - 24e\,\dot{e}^3 + 248e^3\,\dot{e}^3 - 206e^5\,\dot{e}^3 - 280e^7\,\dot{e}^3 + 262e^9\,\dot{e}^3 + 6\dot{e}^4 - 230e^2\,\dot{e}^4 + 680e^4\,\dot{e}^4 - 66e^6\,\dot{e}^4 - 410e^8\,\dot{e}^4 + 70e\,\dot{e}^5 - 658e^3\,\dot{e}^5 + 546e^5\,\dot{e}^5 + 402e^7\,\dot{e}^5 - 7\dot{e}^6 + 260e^2\,\dot{e}^6 - 607e^4\,\dot{e}^6 - 242e^6\,\dot{e}^6 - 26e\,\dot{e}^7 + 296e^3\,\dot{e}^7 + 82e^5\,\dot{e}^7 - 4\,\dot{e}^8 - 56e^2\,\dot{e}^8 - 12e^4\,\dot{e}^8 + (8e^4 - 24e^6 + 24e^8 - 8e^{10} - 32e^3\,\dot{e} + 144e^5\,\dot{e} - 192e^7\,\dot{e} + 80e^9\,\dot{e} - 216e^4\,\dot{e}^2 + 528e^6\,\dot{e}^2 - 312e^8\,\dot{e}^2 + 96e^3\,\dot{e}^3 - 672e^5\,\dot{e}^3 + 640e^7\,\dot{e}^3 + 408e^4\,\dot{e}^4 - 760e^6\,\dot{e}^4 - 96e^3\,\dot{e}^5 + 528e^5\,\dot{e}^5 - 200e^4\,\dot{e}^6 + 32e^3\,\dot{e}^7)\,[1 - (e - \dot{e})^2]^{1/2} \}$,

(11c) $9W(e, \dot{e}, n = +3) = (1/2)\,(p/GM)^{3/2}\,[1 - (e - \dot{e})^2]^{-7/2}\,(e - \dot{e})^{-4}\,\{ 2e^4 - 8e^6 + 12e^8 - 8e^{10} + 2e^{12} - 8e^3\,\dot{e} + 42e^5\,\dot{e} - 78e^7\,\dot{e} + 62e^9\,\dot{e} - 18e^{11}\,\dot{e} + 28e^2\,\dot{e}^2 - 133e^4\,\dot{e}^2 + 248e^6\,\dot{e}^2 - 209e^8\,\dot{e}^2 + 66e^{10}\,\dot{e}^2 - 72e\,\dot{e}^3 + 384e^3\,\dot{e}^3 - 662e^5\,\dot{e}^3 + 472e^7\,\dot{e}^3 - 122e^9\,\dot{e}^3 + 18\dot{e}^4 - 542e^2\,\dot{e}^4 + 1340e^4\,\dot{e}^4 - 914e^6\,\dot{e}^4 + 102e^8\,\dot{e}^4 + 302e\,\dot{e}^5 - 1642e^3\,\dot{e}^5 + 1474e^5\,\dot{e}^5 + 18e^7\,\dot{e}^5 - 45\dot{e}^6 + 1088e^2\,\dot{e}^6 - 1681e^4\,\dot{e}^6 - 122e^6\,\dot{e}^6 - 338e\,\dot{e}^7 + 1200e^3\,\dot{e}^7 + 114e^5\,\dot{e}^7 + 32\dot{e}^8 - 476e^2\,\dot{e}^8 - 48e^4\,\dot{e}^8 + 80e\,\dot{e}^9 + 8e^3\,\dot{e}^9 + (16e^4 - 64e^3\,\dot{e} + 80e^2\,\dot{e}^2)\,[1 - (e - \dot{e})^2]^{7/2} \}$.

Let us remind some of the notations used above: p is the focal parameter of the ellipse (for circular orbits p is simply the radius of the particle trajectory at the considered moment), $u \equiv ln\ p$, $\dot{e} \equiv \partial e/\partial u$, G is the Newton's gravitational constant and M is the mass of the compact object around which the accretion disc rotates. The knowledge of the factor $(p/GM)^{n/2}$ (for all astrophysically significant values of the exponent n) is not needed, because after the substitution of the auxiliary functions Y, Z and W into the dynamical equation (1), this factor cancels out. The partial derivatives of these auxiliary functions with respect to e and $\dot{e}$ are computable without any technical problems and we shall not give here their analytical evaluations. We shall note again that the singularity problem which may arise in relation to null values of e, $\dot{e}$ and $(e - \dot{e})$ in the denominators can be overcome by means of the L'Hospital's theorem (indeterminations of the 0/0 type). The same observation will hold later for the coefficients of dynamical equation (1). Here, another property of the free term of this equation should be mentioned. Upon computing in explicit form the expression $(3Y)\,[\,9W - 2(3Z) + (e^2 - 1)\,(3Y)\,]$, substituting it into equation (1), and reducing it to a common denominator with the second term on the left-hand side of (1), it turns out that the result factorizes with respect to $\dot{e}$. The free term is absorbed into the term containing the first derivatives of $\dot{e}$ and the dynamical equation

(1) becomes a second order *homogeneous* differential equation. It may be shown that this feature is inherent to (1) not only for the considered integer values of $n = -1, 0, \ldots, +3$, but also for an arbitrary physically acceptable n. In view of this, we rewrite equation (1) in the following form:

(12) $\quad A(e, \dot{e}, n)\, \ddot{e} + B(e, \dot{e}, n)\, \dot{e} = 0 .$

We can write the solution of the above equation as

(13) $\quad e(u, n) = \dot{e}_0 \int exp \{ - \int [\, B(e, \dot{e}, n)/A(e, \dot{e}, n) \,]\, du \} + e_0 ,$

where, according to the general theory of second order ordinary differential equations, the solution (for a given value of the exponent n) depends on two integration constants $e_0 \equiv e(u_0, n)$ and $\dot{e}_0 \equiv \dot{e}(u_0, n)$; $u_0 \equiv ln\, p_0$ is a fixed initial value. For example, p_0 may be the focal parameter of the innermost/outermost ellipse bounding the disc.

The above formally written solution is not useful because $A(e, \dot{e}, n)$ and $B(e, \dot{e}, n)$ are known in an explicit form as functions on e, $\dot{e}$ and n, but not as functions on u (so far $e = e(u, n)$ is not solved yet !). A method for solving the equation (11) by means of expanding the eccentricity e by powers in u will be considered in a forthcoming paper. Now we shall restrict ourselves only to give the explicit form of dynamical equation (11) for two values of n, namely $n = -1$ and $n = +2$. For the other considered integer values of n ($n = 0, +1$ and $+3$), the analytical expressions are too long to be given. For this reason, we depict graphically the dependencies of the ratios of the coefficients of equation (11) A and B on e and $\dot{e}$ for fixed n.

Dynamical equation : Case $n = -1$

(14) $\quad 2e^3 (1 - e^2)^{3/2} [\, 8 + (1 - e^2)^{1/2} \,] \ddot{e} + [\, - 3e^3 + 6e^5 - 3e^7 - 36\dot{e} + 74e^2 \dot{e} - 46e^4 \dot{e} + 8e^6 \dot{e} - 48e \dot{e}^2 + 48e^3 \dot{e}^2 - 8e^5 \dot{e}^2 + (12e^3 - 12e^5 + 36\dot{e} - 56e^2 \dot{e} + 68e^4 \dot{e} + 48e \dot{e}^2 - 48e^3 \dot{e}^2) (1 - e^2)^{1/2} \,] \dot{e} = 0 .$

Dynamical equation : Case $n = +2$

(15) $\quad \{ - 10e^4 + 40e^6 - 60e^8 + 40e^{10} - 10e^{12} + 144e \dot{e} - 560e^3 \dot{e} + 724e^5 \dot{e} - 252e^7 \dot{e} - 148e^9 \dot{e} + 92e^{11} \dot{e} + 1104e^2 \dot{e}^2 - 3165e^4 \dot{e}^2 + 2654e^6 \dot{e}^2 - 229e^8 \dot{e}^2 - 364e^{10} \dot{e}^2 - 504e \dot{e}^3 + 4628e^3 \dot{e}^3 - 7208e^5 \dot{e}^3 + 2272e^7 \dot{e}^3 + 812e^9 \dot{e}^3 + 18\dot{e}^4 - 2842e^2 \dot{e}^4 + 9366e^4 \dot{e}^4 - 5554e^6 \dot{e}^4 - 1120e^8 \dot{e}^4 + 696e \dot{e}^5 - 6404e^3 \dot{e}^5 + 7016e^5 \dot{e}^5 + 980e^7 \dot{e}^5 - 81\dot{e}^6 + 2258e^2 \dot{e}^6 - 5021e^4 \dot{e}^6 -$

$532e^6\dot{e}^6 - 408e\dot{e}^7 + 1940e^3\dot{e}^7 + 164e^5\dot{e}^7 + 54\dot{e}^8 - 316e^2\dot{e}^8 - 22e^4\dot{e}^8 +$
$(28e^4 - 84e^6 + 84e^8 - 28e^{10} - 144e\dot{e} + 416e^3\dot{e} - 228e^5\dot{e}$
$- 216e^7\dot{e} + 172e^9\dot{e} - 852e^2\dot{e}^2 + 1572e^4e^2 - 300e^6\dot{e}^2 - 420e^8\dot{e}^2 + 360e$
$\dot{e}^3 - 2328e^3\dot{e}^3 + 1644e^5\dot{e}^3 + 500e^7\dot{e}^3 + 1176e^2\dot{e}^4 - 2124e^4\dot{e}^4 - 260e^6$
$\dot{e}^4 - 108e\dot{e}^5 + 984e^3\dot{e}^5 - 12e^5\dot{e}^5 + 36e^2\dot{e}^6 + 68e^4\dot{e}^6 - 108e\dot{e}^7 - 20e^3$
$\dot{e}^7) [1 - (e - \dot{e})^2]^{1/2} \} \ddot{e} + \{ 6e^4 - 24e^6 + 36e^8 - 24e^{10} + 6e^{12} - 72e\dot{e} +$
$272e^3\dot{e} - 323e^5\dot{e} + 57e^7\dot{e} + 127e^9\dot{e} - 61e^{11}\dot{e} - 72\dot{e}^2 - 236e^2\dot{e}^2 + 982e^4$
$\dot{e}^2 - 683e^6\dot{e}^2 - 276e^8\dot{e}^2 + 285e^{10}\dot{e}^2 - 360e\dot{e}^3 - 234e^3\dot{e}^3 + 889e^5\dot{e}^3 +$
$524e^7\dot{e}^3 - 819e^9\dot{e}^3 + 270\dot{e}^4 - 1528e^2\dot{e}^4 + 1255e^4\dot{e}^4 - 1538e^6\dot{e}^4 +$
$1617e^8\dot{e}^4 + 1493e\dot{e}^5 - 4141e^3\dot{e}^5 + 3717e^5\dot{e}^5 - 2289e^7\dot{e}^5 - 366\dot{e}^6 +$
$4043e^2\dot{e}^6 - 5488e^4\dot{e}^6 + 2331e^6\dot{e}^6 - 1717e\dot{e}^7 + 4870e^3\dot{e}^7$
$- 1665e^5\dot{e}^7 + 261\dot{e}^8 - 2550e^2\dot{e}^8 + 789e^4\dot{e}^8 + 722e\dot{e}^9 - 222e^3\dot{e}^9 - 84\dot{e}^{10}$
$+ 28e^2\dot{e}^{10} + [- 24e^4 + 72e^6 - 72e^8 + 24e^{10} + 72e\dot{e} - 164e^3\dot{e} - 72e^5\dot{e}$
$+ 348e^7\dot{e} - 184e^9\dot{e} + 72\dot{e}^2 + 92e^2\dot{e}^2 + 12e^4\dot{e}^2 - 828e^6\dot{e}^2 + 652e^8\dot{e}^2 +$
$396e\dot{e}^3 - 756e^3\dot{e}^3 + 1632e^5\dot{e}^3 - 1416e^7\dot{e}^3 - 252\dot{e}^4 + 1788e^2\dot{e}^4 -$
$2868e^4\dot{e}^4 + 2060e^6\dot{e}^4 - 1332e\dot{e}^5 + 3492e^3\dot{e}^5 - 2024e^5\dot{e}^5 + 288\dot{e}^6 -$
$2460e^2\dot{e}^6 + 1284e^4\dot{e}^6 + 864e\dot{e}^7 - 472e^3\dot{e}^7 - 108\dot{e}^8 + 76e^2\dot{e}^8] [1 - (e -$
$\dot{e})^2]^{1/2} \} \dot{e} = 0 .$

4. Conclusions

The complexity of the accretion flows phenomena requires using both analytical and numerical approaches for their description. The analytical methods are preferable because of the compact representation of the results, suitable for their interpretations and further applications. They also allow to control more clearly the process of derivation of the solutions and the influence of the accepted approximations on the output data. It often happens that the analytical treatment of the considered problem is not possible to be performed up to the final stage of the computational process and further use of numerical methods is needed. Nevertheless, even this partial application of the analytical description reveals which of the approximations are more important and suggests more effectively how to overcome them and how to improve the model without complicating it too much. Of course, the comparisons with astronomical observations, in our case, observational data of close binary systems containing accretion discs, serve as a test for the task's successful solution. As mentioned above, already existing theoretical models of eccentric discs around the compact stars in binaries explain successfully many of the observed properties of these astronomical objects. For example, Murray [7] has compared the theoretical predictions for the precession rates of eccentric discs with the observed superhump periods. It was found that the inclusion of a retrograde pressure contribution improves

the fit to the data and the consistency with the suggestion that the eccentricity is generated at the 3:1 Lindblad resonance.

It may be supposed that the detailed analytical treatment of the more simple model developed by Lyubarskij et al. [3] would be suggestive for finding analytical solutions to more complicated models like that worked out by Ogilvie [4]. The difficulties and limitations inherent to attempts to resolve the more simplified (and probably easier to solve!) problem would also be indicators of how perspective are the efforts to attain analogous progress in the investigation of the complicated situation. The true answer of this puzzle is expected to be achieved through a series of improved step-by-step analytical and numerical evaluations of the particular accretion disc models.

References

1. B a b t i s t a, R., C. S i l v e i r a, J. E. S t e i n e r, K. H o r n e. Spatially resolved spectra of the accretion disc of the nova-like variable UU Aquarii. – Monthly Not. Royal Astron. Soc., 314, 2000, № 4, p. 713.
2. O g i l v i e, G. I. Tidally distorted accretion discs in binary stars. – Monthly Not. Royal Astron. Soc., 330, 2002, № 4, p. 937.
3. L y u b a r s k i j, Yu. E., K. A. P o s t n o v, M. E. P r o k h o r o v. Eccentric accretion discs. — Monthly Not. Royal Astron. Soc., 266, 1994, № 2 , p. 583.
4. O g i l v i e, G. I. Non-linear dynamics of eccentric discs. – Monthly Not. Royal Astron. Soc., 325, 2001, № 1, p. 231.
5. D i m i t r o v, D. V. One possible simplification of the dynamical equation governing the evolution of elliptical accretion discs. – Aerospace Research in Bulgaria, 17, 2001, p. 17.
6. D w i g h t, G. B. Tables of Integrals and Other Mathematical Data. New York, Mc Millan Company, 1961.
7. M u r r a y, J. R. The precession of eccentric discs in close binaries. – Monthly Not. Royal Astron. Soc., 314, 2000, № 1, L1.

ТЪНКИ ВИСКОЗНИ ЕЛИПТИЧНИ АКРЕЦИОННИ ДИСКОВЕ С ОРБИТИ ИМАЩИ ОБЩА ДЪЛЖИНА НА ПЕРИАСТРОНА. ДИНАМИЧНО УРАВНЕНИЕ ЗА ЦЕЛОЧИСЛЕНИ СТОЙНОСТИ НА СТЕПЕНИТЕ В ЗАКОНА ЗА ВИСКОЗИТЕТА

Димитър Димитров

Резюме

Ние разглеждаме модел на тънък стационарен вискозен акреционен диск около компактен обект със звездна маса, разработен от Любарски и др. [3]. Орбитите на газовите частици са елипси чиито ексцентрицитети могат да варират от вътрешната към външната част на диска и чиито апсидни линии лежат върху една права. Приетият коефициент за вискозитета η удовлетворява зависимостта $\eta = \beta \Sigma^n$, със Σ - повърхностната плътност на акреционния диск, β и n - константи. Нашите разглеждания третират случаите когато експонентата n приема целочислени стойности, а именно n = - 1, 0, 1, 2 и 3, които лежат във физически обоснована област. Ние получаваме в явен вид спомагателните функции въведени от Любарски и др. За две стойности на n = - 1 и n = + 2 ние също сме написали в явен вид динамичното уравнение обуславящо радиалната структура на диска. За другите случаи ние се ограничаваме с графични представяния на отношенията на коефициентите на това уравнение.

Bulgarian Academy of Sciences. Space Research Institute.
Aerospace Research in Bulgaria. 19, 2005, Sofia

REPRESENTATION OF THE CONVEX RADIAL PROFILES OF GALACTIC DISKS BY MEANS OF SERSIC FORMULA: GALAXIES M 31, M 33, LMC, SMC AND M 83

Tsvetan Georgiev

Institute of Astronomy, Bulgarian Academy of the Sciences

Abstract

Iterative one-dimensional decomposition technique for radial galactic profiles in the spirit of Kormendy (1977) is presented and applied on the profiles of nearby galaxies. Both the bulge and disk components are modelled by the Sersic (1968) formula. The free parameters of the model – central brightness, scale length and optimal exponential number N=1/n are derived by internal iterative procedure. The total magnitudes of the bulge and the disk components are derived by numerical integration. The method is applied for decomposition of 22 published profiles of nearby galaxies and for estimation of the errors of their parameters. A hint of correlation is found between the disk exponential number or the disk central brightness, on the one hand, and the total luminosity of the disk, on the other hand. The disks of the big galaxies Milky Way and M 31 show convex shape with some depressed central brightness, while the disks of the dwarf galaxies SMC and LMC show almost exponential shapes with peak of the central brightness. The galaxy M 33 is an intermediate case.

1. Introduction

Usually, the structures of the galaxies are investigated by decomposition of their radial profiles into bulge and disk components. It is deemed that there is no strong physical basis for such a procedure, but this approach is an universal way for describing and comparison of galaxies by means of a small number of well defined parameters. Generally, the objective here is to represent quantitatively the Hubble sequence (de Vaucouleurs 1959a, Freeman 1970, Kormendy 1977, Bagget et al.1998, Simard et al. 2002, Balcells et al. 2003).

On the base of ≈30 profiles of nearby galaxies, Freeman (1970) introduced in use the exponential shape of radial disk profiles as a first approximation, known till now as "Freeman Law". It is considered that the exponential shape of the bright part of the disks may be understood from theoretical point of view (Freeman 1970, Mo et al, 1998, Reshetnikov 2000). However, it is known that the disk scale lengths of exponential disks, derived by different authors, show discrepancies by factor of two (Knapen and van der Kruit 1991), and that the disk scale length does not correlate with the Hubble type (van der Kruit, 2002). Moreover, the deep profiles of galactic disks have convex shapes and Freeman Law is in fact a very rough approximation. Generally, the truncation of the surface brightness of the outer part of the disks may be explained by decreasing the star forming rate, due to insufficient matter concentration or/and lack of reasons for disk instabilities (Bottema 1993, Geressen et al. 1997, Bizyaev and Zasov 2002).

The models of truncated shapes of disk profiles were introduced by van der Kruit and Searle (1981ab) and were applied widely by Barteldrees and Dettmar (1994) by means of a special parameter - cut-off radius. However, when the deepness of the observation increases, the cut-off radius increases, too. For this reason, Pohlen et al. (2000) introduced a presentation of the disk shape with two exponents - inner, corresponding to the Freeman disk, and outer, more steep. The deep observations of 3 face-on galaxies, up to ~29 mag/arcsec^2 in R band of Pohlen et al. (2002) supported this "double exponent model".

Another possibility to describe disk shapes is to use a smooth model of the convex shape of the disk. Fig.1a shows the deep profile of the edge-on galaxy ESO 189-G12 and the respective edge-on view of its face-on exponential model, reproduced from the paper of Barteldrees and Dettmar (1994). The inconsistency between the exponential model in the periphery of the profile is very large - > 2.5 mag or > 10 times in intensity. A parabolic fit of the general shape of the profile is also shown in Fig.1a and it shows that the outer part of the profile is close to parabola. Fig.1b shows the major axis profiles of the galaxies M 31 and M 33 from the papers of de Vaucouleurs (1958, 1959a). The outer parts of these profiles are well fitted by parabolas, too.

After visual analysis of ~ 150 deep major axis profiles of edge-on galaxies, given in the papers of van der Kruit and Searle (1981ab), Karachentsev et al (1992), Barteldrees and Dettmar (1994), Pohlen et al. (2000), we found that 80% of the profiles have parabola-like shapes (Stanchev et al. 2003). In the other 20% of the cases, the profiles seem to be approximately exponential, i.e. they are particular cases of parabola.

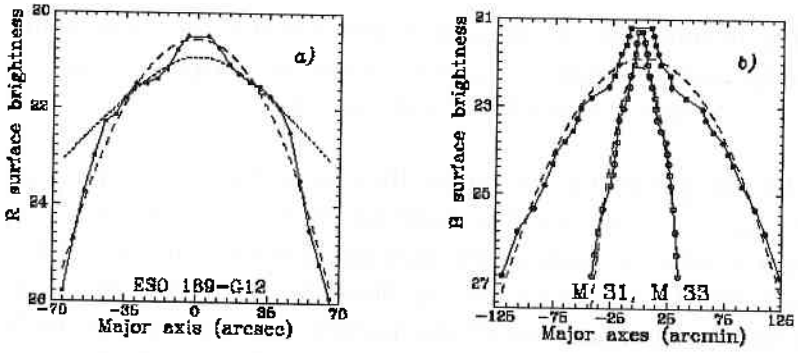

Fig. 1 a) Deep major axes profile of the edge-on galaxy ESO 189-G12 (solid line), the edge-on view of the respective exponential model of the bright part of the disk (dotted line) (Barteldress & Dettmar 1994) and the general shape of the profile, modelled by parabola (dashed line); b) - deep major-axis profiles of galaxies M 31 and M 33 (de Vaucouleurs 1958; 1959b) (solid lines), and their general shapes, modelled by parabolas (dashed lines).

Let us assume that in the magnitude scale, the edge-on disk profile is parabola. Therefore, in the intensity scale, the profile must be Gaussian. However, notice, if the edge-one major-axis disk profile is just Gaussian, than the respective face-one radial disk profile must be again just Gaussian, and the radial disk profiles in magnitudes must be the respective parabola. Obviously, the Gaussian model of the radial face-on profile, which allows simple presentation of the integral of the total luminosity, is very attractive. However, the nature of galactic disks seems more complicated and we introduced flexible modelling of the convex disk profiles, based on the formula of Sersic (1968) (see Part 2). The possible presence of galactic bar is not accounted for in this paper.

The goals of the presented work are: (i) to introduce a one-dimensional decomposition fitting method in the spirit of Kormendy (1977), but including derivation of optimal Sersic exponential degrees both for the bulge and the disk, (ii) to apply this method on numerous published profiles of nearby galaxies, including deriving the fundamental shape and magnitude parameters and (iii) to give an empiric estimations for the standard errors of the derived amplitude parameters.

2. The models and the method of decomposition

It is well known that the apparent profiles of an elliptical galaxy or the bulge of a spiral galaxy may be described by the formula of Sersic

(1968). The formula may be presented in two ways - in linear scale, i.e. in intensities I_R, and in magnitude scale, i.e. in surface brightness, μ_R:

(1) $I_R = I_0 \exp(-(R/H)^N)$ or $\mu_R = \mu_0 + C R^N$

The free parameters in (1) are the central intensity I_0 (or the central brightness $\mu_0 = -2.5 \log I_0$), the scale length $H = (1.0857/C)^{1/N}$) and the exponential number N, which describes the curvature of the profile. These parameters may be derived from the observations by the MLS, applying decomposition techniques. Notice that usually, the exponential number N is noted as 1/n, but following Lauberts and Valentijn (1989) we prefer notation, which are simpler in interpretation of the dependences and correlations with the participation of log N.

The Sersic formula (1) is able to present various shapes of profiles. The case N=1/4, which is known as "1/4 Law" of de Vaucouleurs (1948), describes the profiles of giant ellipticals. N≈1/2 corresponds to the profiles of big ellipticals or bulges of early type spirals. N≈1 corresponds to some ellipticals and bulges of late type galaxies. N≈2 corresponds to some dwarf ellipticals and to some bulges of the very late type galaxies. Generally, the shape of the bulge changes smoothly with Hubble type of the galaxy (Andredakis et al. 1995, Graham 2001). Notice also that N=1 represents just Freeman's (1970) exponential law and N=2 represents just the Gaussian function.

The model (1) may be completed by higher order terms and named "second order Sersic formula" (2) and "third order Sersic formula" (3):

(2) $I_R = I_0 \exp(-(R/H_1)^N-(R/H_2)^{2N})$ or
$\mu_R = \mu_0 + C_1R^N + C_2R^{2N}$

and

(3) $I_R = I_0 \exp(-(R/H_1)^N-(R/H_2)^{2N}-(R/H_3)^{3N})$ or
$\mu_R = \mu_0 + C_1R^N + C_2R^{2N} + C_3R^{3N}$.

Generalizations (2) and (3) of the Sersic formula include two or three scale length parameters The connections between the parameters C_k and H_k have the same form as in case (1).

Different shapes of radial profiles of galaxies are presented in Fig.2. The solid curves that represent different radial shapes of bulges and disks are modelled by formula (1). The dashed curves that represent disks with central depression are modelled by formula (2).

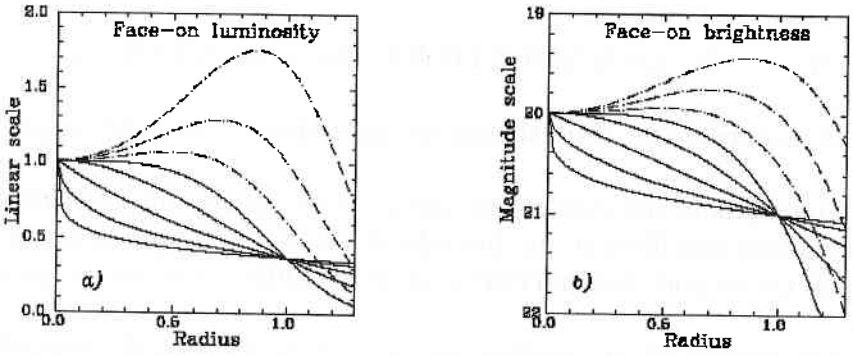

Fig. 2 Examples of models of bulge or disk radial profiles. The solid lines represent 5 shapes of radial profiles of "normal" bulges or disks, modelled by the Sersic formula (1) for N = ? , ? ., 1, 2 and 4, with I_0 = H = 1. The dashed lines represent 3 shapes of convex disk profiles with central depression, modelled by the second order Sersic formula (2), with different parameters. The profiles are presented in arbitrary intensity (a) and magnitude (b) scales.

The third order Sersic formula (3) is very useful, too. Our experience shows that it describes very well the general radial profile of galaxy with bulge and disk components. The value of N is usually between 0.5 and 1. Moreover, the inflex point between the bulge and disk, where the shape of the profile changes from concave to convex type, is usually the natural dividing point between the bulge and disk parts of the profile, necessary for the decomposition. We note that the same point, derived by means of the usual 3-rd order polynomial, corresponding to (3) with N=1, lies usually rather far from the bulge. Formula (3) may describe also various shapes of ring-like disks. For example, if C_2=0 complies with the formula of Kormendy (1977) for disk with exponential outer part and sharp inner truncation.

Having the estimation of the free parameters in (1), the total intensity I_T of the object (bulge or the disk) may be derived by integration along the polar angle and the radius:

$$\infty$$

(4) $I_T = b/a\ I_0\ 2\pi\ H \int_0 \exp(-(R/H)^N)dR$

Here *b/a* is the apparent axial ratio of the object. The total intensity may be written using the gamma function Γ (van der Kruit and Searle 1981ab; Barteldrees and Dettmar 1994):

(5) $I_T = b/a\ I_0\ 2\pi\ H/N\ \Gamma(1/N) = b/a\ I_0\ 2\pi\ H\ \Gamma(1/N+1).$

In practice, in the general case, we apply direct numerical integration of (4).

More details and connections between the system of parameters of de Vaucouleurs and these in the formula of Sersic (1) are given f.e. in the papers of Ciotti and Bertin (1999), Graham (2001) and the references therein.

For analysis of 1D profiles, we created an iterative decomposition procedure like that described by Kormendy (1977), which fits both the bulge and disk profiles from formula (1). Applying formulae (2) or (3) in some special cases is also possible. The number of main iterations of the disk and bulge fitting is usually < 10. In each case of fitting, the optimal exponential numbers are derived by iterative gradient method. The number of these "inner" iterations is usually < 50. As a special case of the procedure, the exponential numbers of the bulge and/or disk models may be fixed in advance by the user. In the applications presented here, we discuss only the models with optimal exponential numbers. The total computing time for one profile with 100–200 points, for computer of the class of Pentium 1 is up to 2 seconds.

In the case of smooth profile without prominent bar the results of the decomposition do not depend strongly on the choice of the dividing point. In these cases, the inflex point of the 3-rd order model (3) may be used automatically. In more complicated or "noised" cases, we execute the procedure sometimes, searching for the dividing point that gives the minimum RMS of the restored profile. Where needed, the decomposition procedure may remove automatically a few "noised" points close to the dividing point.

The results of the process in the presented work are the parameters μ_0, H and N, according to formula (1), both for the bulge and the disk, as well as the total magnitudes of the bulge, disk and galaxy by formula (4). The estimation of other parameters is derived, too (see Part 4). We note that the values of N and H do not depend on the Milky Way extinction. The

other parameters are estimated in two cases - with and without extinction correction of the profile.

3. The profiles and their decompositions

The nearby galaxies M 31, M 33, LMC and SMC play fundamental role in the knowledge about the Universe and the presented decomposition technique is applied first on their profiles. Additionally, a profile of the galaxy M 83 and a model of the Milky Way are included for comparison.

The basic parameters of the galaxies, collected from NED and LEDA, are given on Table 1, as follows: the galaxy name, the Hubble type, the distance modulus DM, the Milky Way foreground extinction in B-band A_B, the total apparent B-magnitude B_T, the total colour index $(B-V)_T$, the apparent blue diameter at surface brightness level 25 mag/arcsec^2 d_{25}, the apparent axial ratio *a/b*, the total B-magnitude, corrected for foreground and internal extinction $B_{0,C}$, the respective colour index $(B-V)_{0,C}$, and the respective corrected apparent diameter $d_{0,C}$.

Table 1. Basic data about the galaxies adopted from data bases NED and LEDA

Galaxy	Type	DM	A_B	B_T	$(B-V)_T$	d	*a/b*	$B_{0,C}$	$(B-V)_{0,C}$	$d_{0,C}$
M 31	Sb	24.43	0.46	4.36	0.92	186.2'	3.02	3.24	0.73	195.0'
M 33	Sc	25.06	0.18	6.29	0.56	66.0'	1.66	5.73	0.47	67.6'
LMC	SBm	19.66	0.26	0.90	0.51	647.7'	1.17	0.51	0.43	676.1'
SMC	SBm	18.41	0.20	2.75	0.45	371.5'	2.21	2,21	0.36	380.2'
M 83	SBc	29.57	0.29	8.53	0.66	14.1'	1.10	8.17	0.58	14.8'

Because of the large apparent sizes of the galaxies M31 and M 33, accurate CCD observations have not been made yet. For this reason, we have used available data: (i) the equivalent (elliptically averaged) profiles and the photometry sections along the axes and the direction Ease-West in B band, published by de Vaucouleurs (1958, 1959b), (ii) the equivalent profiles of M 31 in the U, B, V and R_C bands of Walterbos and Kennicutt (1988), and (iii) the photometry sections along the major of M 31 and M33 axis in Gunn r-band of Kent (1987). The data for the central part of M 33 of de Vaucouleurs (1959b) are completed by the data of Kent (1987) in the Gunn g-band. We have used the rough relation $B \approx g + 0.6$, derived from the data about the center of M31 of de Vaucouleurs (1958) and Kent (1987). The profiles of M 83 and the model of the Milky Way are used from the paper of Freeman (1970). We account for the foreground extinction through the relations $A_U=1.26\ A_B$, $A_V=0.77A_B$, $A_R=0.62A_B$ and $A_I=0.45A_B$ (Schlegel et al., 1998).

The graphs of the decompositions of the profiles of M 31 and M 33 into bulge and disk components are shown in Fig.3-6. The convex shapes of the disks and their good representation by the Sersic formula (1) can be seen well. The convex shape is not well enough prominent only in the case of M 33, in Fig.5b, because the used profile of Kent (1987) is obviously not deep enough.

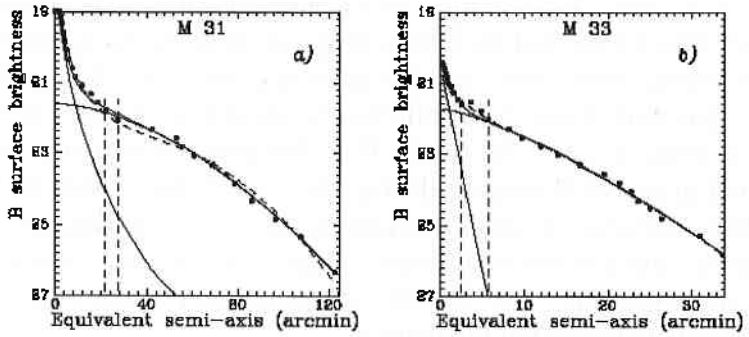

Fig. 3 Decomposition of the equivalent profiles of the galaxies M 31 (a) and M 33 (b) by data of de Vaucouleurs (1958, 1959b) in B band. The solid curves represent the shapes of the bulge, disk and restored profile. The dashed curves represent the fit of the whole profile with the polynomial (3). The vertical lines represent the last used point of the bulge and the first used point of the disk; the points between the vertical lines are not used in the decomposition.

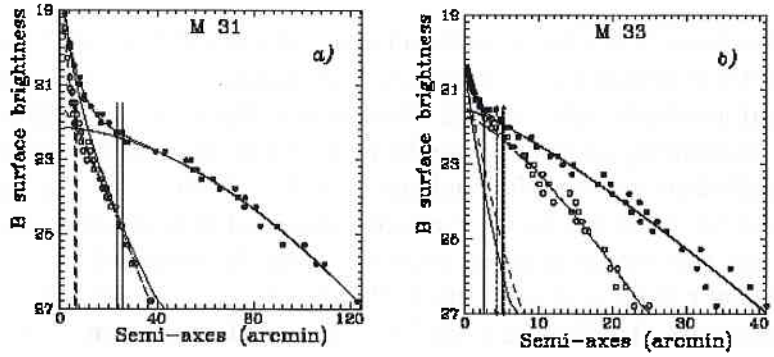

Fig. 4 Decomposition of the major axis profiles (dots, solid lines) and minor axis profile (circles, dashed lines) of the galaxies M 31 and M 33 by data of de Vaucouleurs (1958, 1959b) in B band. See also the caption of Fig.3.

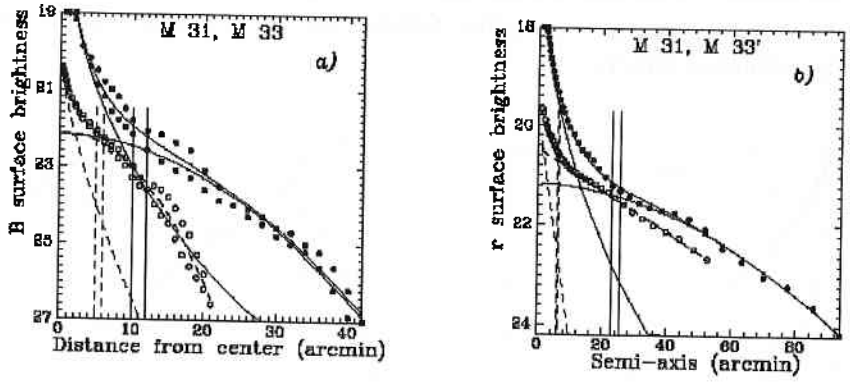

Fig. 5 a) Decomposition of the East-West sections of M 31 (dots, solid lines) and M 33 (circles, dashed lines) by data of de Vaucouleurs (1958, 1959b); b) Decomposition of the major (dots, solid lines) and minor (circles, dashed lines) axes profiles of the galaxy M 31 by data of Kent (1987) in r band. For better comparison, the abscissa data of M 33 is multiplied by factor of 3. See also the caption of Fig.3.

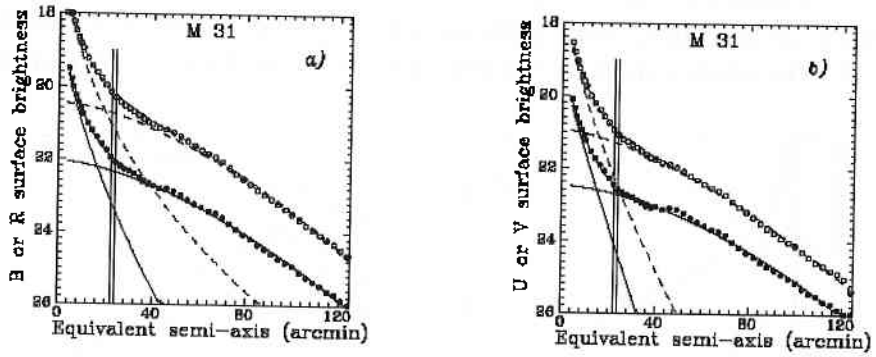

Fig. 6 Decomposition of the equivalent axis profiles of the galaxy M 31 by data of Walterbos and Kennicutt (1988): a) in B band (dots, solid lines) and R band (circles, dashed lines); b) in U band (dots, solid lines) and V band (circles, dashed lines). See also the caption of Fig.3.

The profiles of the LMC and SMC are presented in Fig.7. The disk parts of these galaxies are almost exponential, even LMC shows concave disk profile. We note that the LMC is the galaxy with the largest apparent size on the sky, which is the most difficult for surface photometry at low brightness levels. In the cases of LMC and SMC, two processings of the

data are made – with decomposition into bulge and disk, and without, only by fitting the whole profile by the Sersic formula (1). The results are very close (see Parts 4 and 5).

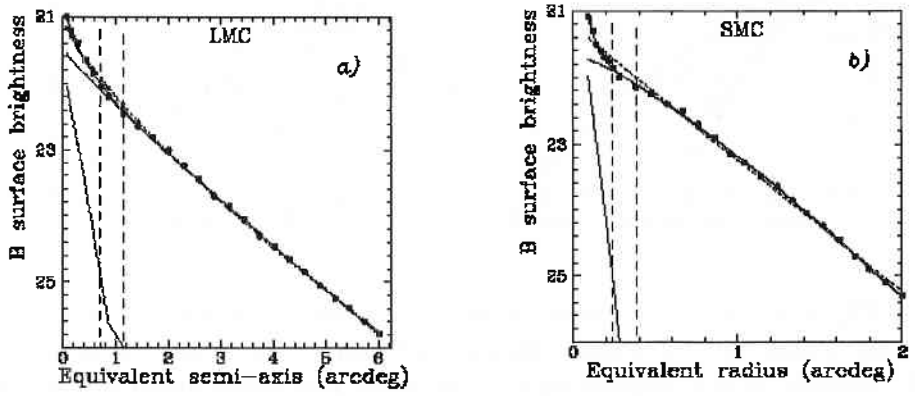

Fig. 7 Decompositions of equivalent profiles of the galaxies LMC (a) and SMC (b) by data of de Vaucouleurs (1960). The dotted lines show the fit of data by the Sersic formula (1) without decomposition.

Profiles of the SB galaxy M 83, as well as a model of the mass density of the Milky Way, published by Freeman (1970) are presented in Fig.8. The convex shape of the disk parts of the profiles is well represented.

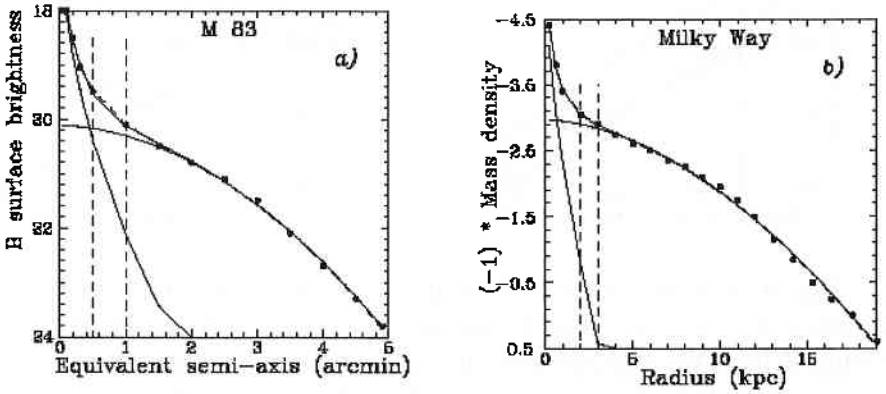

Fig. 8 Decomposition of the profiles of M 83 (a) and of the Milky Way model (b), from the graphs published by Freeman (1970).

The decompositions shown in Figs.3-8 are used to derive the shape, si e and magnitude parameters of the galaxies discussed in Parts 4 and 5.

4. Results about the shape and size parameters

The results from the decompositions are presented on Table 2, as follows. RMS is the standard error of the restored profile, N_b and N_d are the exponential numbers of the bulge and disk, respectively, $\mu_{0,b}$ and $\mu_{0,d}$ are the apparent central brightness of the bulge and disk, H_d is the scale si e of the disk, log H_d/H_b is the logarithm of the ratio of the scale si es of the disk and the bulge, d_{25} is the estimated diameter of the disk profile at 25 mag/arcsec^2, obtained from the intrinsic profile, $d_{25,0}$ is the diameter at the same level, but obtained after preliminary subtraction of the galactic extinction from the profile data and source in the referenced paper.

Table 2. Shape and si e parameters of the bulge and the disk

Galaxy	Band	RMS	N_b	N_d	$\mu_{0,b}$	$\mu_{0,d}$	H_d	log H_d/H_b	D_{25}	$D_{25,0}$	Source
M 31	B	0.11	0.32	1.75	14.72	21.65	52.8'	3.26	185.1	201.4	1
M 31	U	0.07	0.90	1.66	19.31	22.51	59.0'	2.01	194.8	220.5	2
M 31	B	0.05	0.64	1.57	17.95	22.07	54.2'	1.45	203.5	228.2	2
M 31	V	0.05	0.68	1.48	17.15	20.96	48.5'	1.32	235.9	245.9	2
M 31	R	0.04	0.44	1.58	14.98	20.46	52.3'	2.07	258.2	268.9	2
M 31	r	0.05	0.41	1.82	15.12	21.16	53.7'	2.60	214.6	223.6	3
M 33	B	0.06	0.99	1.36	20.55	21.74	12.8'	1.14	57.5	59.8	4
M 33	r	0.02	0.93	1.01	15.80	20.48	8.8'	1.08	71.9	73.7	3
M 31	B	0.12	0.52	1.75	17.13	22.17	53.8'	1.97	185.8	202.5	1a
M 31	B	0.16	0.24	1.30	9.29	21.87	11.5'	4.87	51.9	57.7	1b
M 31	B	0.26	0.40	1.96	14.81	22.21	19.9'	2.51	64.2	69.4	1c
M 33	B	0.23	0.73	1.22	20.26	21.55	10.9'	1.32	56.4	58.8	4a
M 33	B	0.17	0.85	1.35	20.49	21.74	7.6'	0.92	34.6	36.0	4b
M 33	B	0.21	0.72	2.10	20.27	22.15	10.9'	1.09	34.5	35.5	4c
LMC	B	0.02	1.16	0.92	20.84	21.48	81.0'	0.66	576.0	624.0	5
LMC	B	0.07	-	0.78	-	21.02	54.0'	-	576.0	630.0	5d
SMC	B	0.03	1.10	1.25	20.24	21.64	45.0'	0.98	204.0	234.0	5
SMC	B	0.10	-	0.99	-	21.21	31.8'	-	228.0	240.0	5d
M 83	B	0.06	0.50	1.90	16.18	20.12	2,6'	1.90	11.3	11.7	6
Milky Way		-	0.61	1.78	-	-	9.9 kpc	1.68	-	-	6

Sources of data: 1 - de Vaucouleurs (1958); 2 – Walterbos and Kennicutt (1988);

3 - Kent (1987); 4 - de Vaucouleurs (1959b); 5 - de Vaucouleurs (1960); 6- Freeman (1970). The notations 'a','b' and 'c' correspond to the photometry sections along the major axis, minor axis and the direction east-west in the respective works, the notation 'd' corresponds to parameters, derived without decomposition, as a result of fit of the whole profile by means of (1).

Table 2 shows that the standard error (RMS) of the restored equivalent profiles is small, while the photometry sections of M 31 and M 33 are significantly noised. The errors of the derived photometry parameters

of galaxies are due mainly to the data incompleteness and/or the errors of the magnitude scale zero point. For this reason, the theoretical standard deviations of the parameters, estimated only based on the application of the MLS, is underestimated, but comparison of the results, obtained from different data sets may give empiric error estimation.

The values of N_b, $\mu_{0,b}$ and log H_d/H_b depend strongly on the completeness of the data about the central part of the galaxy and they show significant differences (see also the discussion of Graham, 2001). The estimations of the disk parameters N_d and $\mu_{0,d}$ depend mainly on the deepness of the profiles. In the cases of the most deep profiles – these along the direction East–West for M 31 and M 33, we derive $N_d \approx 2$, corresponding to the Gaussian function. The disk size parameters – H_d, D_{25}, and $D_{25,0}$ have various estimations, too. In the cases of LMC and SMC, both methods, with decomposition and with general fit only, show approximately exponential disks and relatively high central brightness. In the case of the Milky Way, only the shape parameters N_b, N_d, H_d and log H_d/H_b are derived.

Table 2 contains numerous estimations of shape and size parameters about M 31 and M 33 and gives possibilities for estimation of their mean values and the standard errors. The results are collected in Table 3 where the notations of the parameters and the sources are the same as in Table 2. In the greatest number of cases, the average of two estimations, using equivalent profiles and major axis profiles, is given. For N_b and $\mu_{0,b}$, suggesting that the axis ratio of the bulge is just unit, we include in the estimation also the profiles along the minor axes and the directions East-West, using all data of de Vaucouleurs (1958, 1959b). The mean values from the data of Walterbos and Kennicutt (1988) about M 31 are given for comparison.

Table 3. Mean values and errors of the shape and size parameters of M 31 and M 33

Galaxy	Band	N_b	N_d	$\mu_{0,b}$	$\mu_{0,d}$	H_d	log H_d/H_b	D_{25}	$D_{25,0}$	Source
		+/-	+/-	+/-	+/-	+/-	+/-	+/-	+/-	
M 31	B	0.37	1.75	13.99	21.91	53.3	2.62	185.4	202.0	1
		0.12	0.10	3.32	0.37	1%	0.90	0.3%	0.2%	
M 31	UBVR	trend	1.57	trend	trend	53.5	1.71	trend	trend	2
		-	0.07	-	-	8%	0.38	-	-	
M 33	B	0.82	1.29	20.39	21.64	11.8	1.23	57.0	59.4	4
		0.13	0.10	0.15	0.13	11%	0.13	1%	1%	

The estimation of the N_b of a distant galaxy depends strongly on the resolution, the completeness of the data, etc. In the cases of M31 and M33, the most nearby spiral galaxies, these effects are not strongly revealed. The data of Kent (1987) occur also close to the data of de Vaucouleurs (1958)

(Table 2). The error of the estimation of N_b may be considered < 0.15. However, the data of Walterbos and Kennicutt (1988) shows well manifested trend - the value of N_b decreases from U band toward R band from 0.9 to 0.4. Obviously, in comparison with the R band, in the U band, the bulge of M31 seems more truncated, with shape of the equivalent profile near to exponential. Generally, the values of N_b for M31 and M33 on Table 3 (as well as those of M83 and the Milky Way on Table 2) correspond well to the dependence "log n_b – Hubble type" and "log n_b – log (D/B)" of Andredakis et al. (1995) and Graham (2001) (n=1/N and D/B is the disk-to-bulge luminosity ratio). Here, these values are log $(1/N_b) = 0.43$ +/- 30% for M31 and log $(1/N_b) = 0.09$ +/- 25% for M33. Generally, the relative error of the values of log n_b or log N_b may be considered <30%.

Generally, the value of N_d depends on the inclination of the galaxy - the most convex shapes of the disks are visible in the cases of the edge-on galaxies (see f.e. Pohlen et al 2000). The value of N_d depends also on the deepness of the observation. Here the most convex profiles, with $N_d \approx 2$, are visible in the cases of the miost deep observations - along the EW directions of M 31 and M33 of de Vaucouleurs (1958, 1959b). No significant dependanse of N_d on the photometry band in Walterboss and Kennicutt (1988), but their mean value - $N_d = 1.57$ +/- 0.07 - is lower, then in the data of de Vaucouleurs (1958) - $N_d = 1.75$ +/- 0.10. Generally, the error in the estimation of log N_d may be considered to be <10%.

The central bulge brightness $\mu_{0,b}$ is very poorly defined, especially in cases of small N_b. Our estimation of $\mu_{0,b}$ for M 31 is very uncertain. In the case of M33, the estimation of $\mu_{0,b}$ seems to be better, within an error of 0.15 mag. The intrinsic values of $\mu_{0,d}$ depend strongly on the inclination angle of the galaxy and/or position angle of the section. Here, for M31 and M33 we obtain estimations with different uncertainties. The used material is not sufficient for good estimation of the error of $\mu_{0,d}$, but we assume the error to be <0.3 mag. The error of log H_d/H_b seems to be <30%. Table 4 shows also that the scale length may be estimated within a standard error <2% and the error of the diameters at low isophote levels is less - ≈1%.

5. Results about the total magnitudes

The estimations of the total magnitudes of the bulges, disks, the sum of bulge plus disk, as well as the D/B ratio, may be derived from the equivalent profiles only. The respective results are presented on Table 4, as follows: m_{lim} is the limiting surface brightness magnitude of the published photometry data, m_b ,m_d and m_T are the total magnitudes of the bulge, disk and the sum of the bulge and disk, estimated by the formula (2), m_{b0}, m_{d0}

and m_{T0} are the same total magnitudes, but estimated upon extraction of the respective foreground extinction, and $\log(D/B)_{T0}$ is the respective disk-to-bulge luminosity ratio. The sources of data: the same as with Table 2.

Table 4. Magnitude parameters derived from the equivalent profiles

Galaxy	Band	m(lim)	m_b	m_d	m_T	m_{b0}	m_{d0}	m_{T0}	$\log(D/B)_{T0}$	Source
M 31	B	26.8	9.83	3.94	3.93	9.37	3.48	3.47	2.36	1
M 31	U	26.2	5.18	4.09	3.75	4.61	3.52	3.18	0.44	2
M 31	B	26.0	5.30	3.84	3.58	4.84	3.38	3.12	0.58	2
M 31	V	24.6	4.16	2.96	2.64	3.81	2.60	2.30	0.48	2
M 31	R	25.4	4.82	2.30	2.20	4.52	2.00	1.90	1.01	2
M 31	r	24.2	6.55	2.95	2.91	6.59	2.65	2.62	1.57	3
M 33	B	25.8	9.82	5.97	5.94	9.64	5.79	5.76	1.54	4
M 33	r	24.7	9.58	5.34	5.32	9.48	5.33	5.30	1.66	3
LMC	B	25.8	4.76	1.19	1.15	4.50	0.93	0.89	1.43	5
SMC	B	25.3	6.54	3.01	2.98	6.34	2.81	2.76	1.42	5
M 83	B	23.8	11.97	7.42	7.41	11.68	7.13	7.12	1.82	6

Table 4 show that the total magnitudes of the bulges of M 31 and M 33, as well as the respective disk-to-bulge ratios are poorly derived. In the case of disks, as well of total magnitudes when the contribution of the bulge is small, the accordance of the results is better. In R-band, the different deepness of the profiles and different photometry systems for M31 make the total magnitudes much different.

The galaxy M31 has large apparent size and its photometry investigations are very difficult. Here, we may compare the total magnitudes and colours from some sources. According the LEDA, the data about M31 are B_T = 4.36 mag, $(U-B)_T$ = 0.50 and $(B-V)_T$ = 0.92. Walterbos and Kennicutt (1988), applying the "1/4 law model" for the bulge and exponential model for the disk, derived from their equivalent profiles B_T = 5.21 mag, $(U-B)_T$ = 0.34 and $(B-V)_T$=0.74. Using the data of Walterbos and Kennicutt (1988) and decomposing the profiles with optimal polynomial degrees, we obtain B_T =3.58 mag, $(U-B)_T$ = 0.17 and $(B-V)_T$ = 0.94. The large differences between total magnitudes and color indexes, derived from the different data and methods underline again the problem with the accurate photometry of M31 and M33. Our results in B and R bands are collected in Table 5, where the notations are the same as in Table 4.

Table 5. Mean values and errors of the magnitude parameters of M31 in B and R bands

Galaxy	Band	m_b	m_d	m_T	m_{T0}	$\log(D/B)_{T0}$	Source
		+/-	+/-	+/-	+/-	+/-	
M31	B	7.65	3.89	3.76	3.30	1.47	1,2
		3.20	0.07	0.25	0.25	1.26	
M31	R,r	5.68	2.62	2.56	2.26	1.29	2,3
		1.22	0.46	0.50	0.51	0.40	

Based on available data about M31 and M33, we consider the error of the estimations of the total magnitudes of the disks or the whole galaxies to be about 0.5 mag.

6. Conclusions

In the presented paper, we present the results about the photometry parameters of nearby galaxies upon decomposition of their profiles into bulge and disk components, accounting for the convex shape of the disk profiles. We should expect that this method does not overestimate the central disk brightness and that it will provide for more real estimation of the total disk brightness. Therefore, we must expect a hint of some "scaling relations" between disk luminosity or size and its shape parameters.

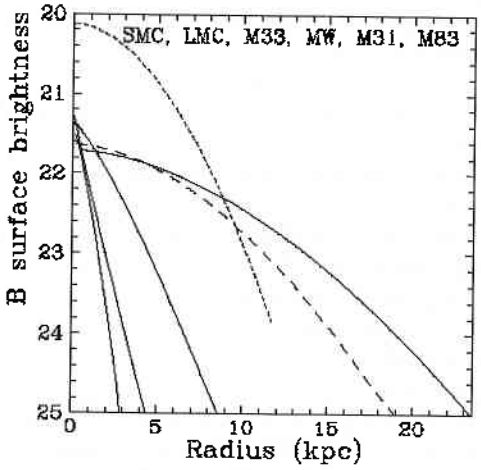

Fig. 9 Comparison of the disk models of the galaxies. The solid curves, from left to right, correspond to the galaxies SMC, LMC, M33 and M31. The model of the Milky Way disk, shifted arbitrarily along the ordinate axis is shown by dashed curve. The disk of the SB galaxy M83, modelled not accounting for the presence of bar, is shown by dotted line.

The true shapes of the disks of the galaxies, included in the presented work, are shown in Fig.9. We see that the disks of the giant galaxies, M31 and the Milky Way, display well manifested convex shapes (or depressed central brightness), while the disks of the dwarf galaxies SMC and LMC display almost exponential shapes with high central brightness. M33 is an expected intermediate case. However, we include M83 to show that the situation is more complicated. The disk of M83, having approximately the size of M33, seems to be very bright and very convex. The reason may be in the fact, that the profile of the SB galaxy, M83 is decomposed not accounting for the presence of bar.

Generally, the central brightness and the exponential number of the disk shape seem to be potential photometric indicators of the galaxy's gigantism. This conclusion should be confirmed or rejected based on rich and uniform number of disk profiles.

References

1. Andredakis Y. C., Peletier R. F., Balcells M., 1995, MNRAS 275, 874
2. Bagget W. E., Bagget S. M., Anderson K. S. J., 1998, AJ 116, 1626
3. Balcells M., Graham A. W., Dominguez-Palmero L., Peletier R.F., 2003, ApJ 582, L79
4. Barteldrees A., Dettmar R. -J. 1994, A&AS 103, 475
5. Bizyaev D. V., Zasov A. V., 2002, Astron. Reports 46,721
6. Bottema R. 1993, A&A 275, 16
7. Chiotti L., Bertin G., 1999, A&A 352, 447
8. Geressen J., Kuijken K., Merrifield M., 1997, MNRAS 288,618
9. Graham A. W., 2001, AJ 121,820
10. de Vaucouleurs G., 1948 Ann. d'Astrophys. 11, 247
11. de Vaucouleurs G., 1958, ApJ 128, 465
12. de Vaucouleurs G., 1959a, in: Handbuch der Physik LIII, ed. Flugge S.,
13. Springer-Verlag Berlin, p.275, 311
14. de Vaucouleurs G., 1959b, ApJ 130, 728
15. de Vaucouleurs G., 1960, ApJ 131, 574
16. Freeman K. C., 1970 ApJ 160, 811
17. Kent S. M. 1987 AJ 94, 306
18. Karachentsev I., Georgiev T., Kajsin S., Kopylov A., Shergin V. and Riadchenko V., 1992, Astron.Astrophys.Transactions, 2, 265
19. Knapen J. H., and van der Kruit P. C., 1991, A&A 248,57
20. Kormendy J., 1977 Ap.J 217, 406
21. Lauberts A., Valentijn E. A., 1989, The surface photometry catalogue of the ESO-Uppsala galaxies, Garching bei Munchen, ESO
22. Mo H. J., Mao S., White S. D. M., 1998, MNRAS 295,317
23. Pohlen M., Dettmar R.-J., Luttlcke R., Schwarzkopf U., 2000, A&AS 144,405

24. Pohlen M., Dettmar R.-J., Lutticke R., Aronica G., 2002, A&AS 392,807
25. Reshetnikov V. P., 2000, Astron.Letters 26, 485
26. Sersic J. -L., 1968, Atlas de Galaxies Australes (Cordoba: Obs. Astron. Univ. Nat. Cordoba)
27. Schlegel D. J., Finbeiner D. P., Davies M., 1998, ApJ 500, 525
28. Simard L., Willmer C. N. A., Vogt N. P. et al. (10 authors) 2002 ApJS 142,
29. Stanchev O. I., Groanova Yu. B., Georgiev Ts. B., 2003, Publ.Astron.Obs.Belgrade No.73, 231
30. van der Kruit P. C., 2002, in eds. G.S.Da Costa & E.M. Saadler,
31. The Dynamics, Structure & History of Galaxies, ASP Conference Serries
32. van der Kruit P. C. & Searle L., 1981a, AA 95, 105
33. van der Kruit P. C. & Searle L., 1981a, AA 95, 116
34. Walterbos R. A. M., Kennicutt R. C, Jr., 1988, A&A 198, 61

ПРЕДСТАВЯНЕ НА ИЗПЪКНАЛИТЕ РАДИАЛНИ ПРОФИЛИ НА ГАЛАКТИЧНИТЕ ДИСКОВЕ ЧРЕЗ ФОРМУЛАТА НА СЕРСИК: ГАЛАКТИКИТЕ M 31, M 33, LMC, SMC И M 83

Цветан Георгиев

Резюме

Представена е итеративна едномерна декомпозиционна процедура за профили на галактики в духа на Корменди (1977) и е приложена за близки галактики. Компонентите на балджа и диска се моделират чрез формулата на Серсик (1968). Свободните параметри на модела – централната яркост, мащабният размер и оптималният експоненциален показател – се получават чрез итеративна градиентна процедура. Тоталните звездни величини на диска и балджа се получават чрез числено интегриране. Методът е приложен за декомпозиция на 22 публикувани профила на близки галактики и за оценки на грешките на техните параметри. Намерен е намек за корелация между дисковия експоненциален показател и централната яркост на диска от една страна и тоталната светимост на диска от друга. Дисковете на големите галактики – Млечния път и M31 показват изпъкнали профили с понижена централна яркост, докато дисковете на галактиките джуджета – LMC и SMC имат почти експоненциални профили с пикове на централната яркост. Галактиката M33 е междинен случай.

Bulgarian Academy of Sciences. Space Research Institute.
Aerospace Research in Bulgaria. 19, 2005, Sofia

ALGORITHM FOR HIGH-PRECISION GEOREFERENCE AND RECTIFICATION OF HIGH-RESOLUTION SPACE IMAGES

Nikola Georgiev

Space Research Institute, Bulgarian Academy of Sciences

Abstract

The current state-of-the-art of high-resolution space images enables the performance of large scale mapping, map updating, monitoring of the Earth cover and the environment, and other practical, scientific, and defence-related tasks requiring to determine with great accuracy the mutual position of individual discrete points [2, 3, 4, 5, 6, 7, 8, 9].Based on a number of studies conducted at home and abroad [4, 7, 9], it was proven that the space images obtained upon their processing by the supplier and accordingly, upon their high-precision georeference and rectification by the user, differ substantially in their precision. This happens when the user determines the coordinates of the ground-based CPs using GPS measurements and dedicated software, accounting for the recommendations made during processing.Based on the designed mathematical model [1, 3, 5], an algorithm is suggested that may be used to prepare software for processing and assessment of collected observational material after the Least Square Method (LSM).

***Key words**: GPS, georeferenc, rectification, LSM*

1. Introduction

In a series of studies [1, 2, 3, 5, 6], a mathematical model for georeference and rectification of high-resolution space images was developed. Based on this model, we shall present here an algorithm for preparation of software intended for processing of space images (scanner and photo images) and obtaining the coordinates of identified terrain control points (CPs) on the terrain and on the space image, and rectification of the geometric deformations.

Therefore, to ensure that high-resolution space images will accomplish their nowadays task in large-scale topographic mapping, map revision, monitoring of the environment, study of the outer space, ecology, safety, precise monitoring of earth cover changes etc., these images must be subject to preliminary processing [2,3,4,5,6,7, 9] comprising:

-high-precision coordinate georeference of the images of CPs, measured by GPS;

-rectification of the images by approximation functions, or by accounting for the changes in the scale factors along the scene's directions and the relief's configuration;

-using the Earth (reference) ellipsoid as a projection plane;

-accounting for the ellipsoid heights of the CPs;

-precise processing and result assessment after the Least Square Method (LSM).

The observance of these conditions will provide to obtain ultimate results with accuracy corresponding to the potentials of these modern space images.

2. Orientation and stabilization of the space aircraft.

The information which is obtained and used with space images is diverse with respect to both the elements to be defined and their location in space and time. For this reason, the coordinate systems in which the SA elements are determined refer to various space rectangular coordinate systems, namely:

1. *Greenwich Equatorial Geo-Centric Coordinate System - O, X, Y, Z.*
2. *Inertial Equatorial Geo-Centric Coordinate System - O, X'_k, Y'_k, Z'_u.*
3. *Geodetic Rectangular Geo-Centric Coordinate System - O, X_j, Y_j, Z_j.*
4. *Satellite-Centric Inertial Coordinate System - $j-(x, y, z)kj$ (Fig.1,2).*

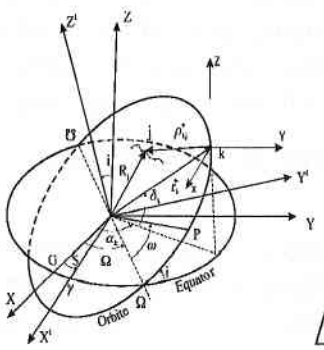

Fig. 1

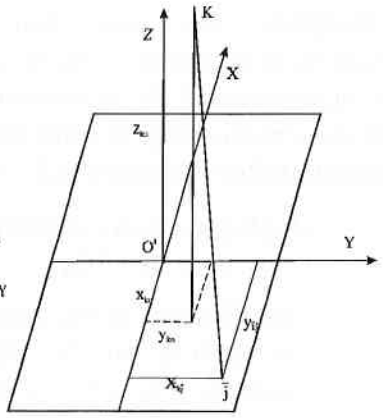

Fig. 2

According to Fig.1 we may write the following relation between the satellite-centric radius-vector $\vec{\rho}_{kj}$, the geo-centric radius-vector $\vec{r}_k$, and the topo-centric radius-vector $\vec{R}_{kj}$ in coordinate form with respect to the *inertial geo-centric system (I)*, namely:

$$\vec{\rho}_{kj} = (\vec{R}_j - \vec{r}_k) = \begin{vmatrix} X'_j - X'_k \\ Y'_j - Y'_k \\ Z'_j - Z'_k \end{vmatrix} = \rho_{kj} \begin{vmatrix} \cos\alpha_k \sin\delta_k \\ \sin\alpha_k \cos\delta_k \\ \sin\delta_k \end{vmatrix} = \rho_{kj} \begin{vmatrix} \xi_{kj} \\ \eta_{kj} \\ \zeta_{kj} \end{vmatrix}, \tag{1}$$

where:

$$\xi_{kj}^{\ 2} + \eta^2_{kj} + \zeta^2_{kj} = 1; \tag{2}$$

$$\rho_{kj} = \sqrt{(X_j - X_k)^2 + (Y_j - Y_k)^2 + (Z_j - Z_k)^2}$$

α_{kj} and δ_{kj} are the SA's rectascence and declination

$\vec{R}_j = (X', Y', Z')_j^T$ - the coordinates of the CP - j *in the inertial geo-centric system*

$\vec{r}_k = (X', Y', Z')_k^T$ - the coordinates of the SA - k *in the inertial geo-centric system.*

Let us assume that the vector $\vec{D}_{kj}$ by the image $\bar{j}$ on the space image (Fig.2), of terrain point *j* in the *inertial satellite-centric coordinate system* is expressed as follows:

$$\vec{D}_{kj} = \begin{vmatrix} x_{k\bar{j}} - x_{ko} \\ y_{k\bar{j}} - y_{ko} \\ z_{k\bar{j}} - z_{kj} \end{vmatrix} = D_{k\bar{j}} \begin{vmatrix} \xi_{kj} \\ \eta_{kj} \\ \zeta_{kj} \end{vmatrix}, \tag{3}$$

$$D_{k\bar{j}} = \sqrt{(x_{k\bar{j}} - x_{ko})^2 + (y_{k\bar{j}} - y_{ko})^2 + (z_{k\bar{j}} - z_{ko})^2}$$

where:

$(x, y, z)_{kj}$ - coordinates of the CP's image - j on the space image;

$(x, y, z)_{ko}$ - coordinates of the photo's main point O, obtained by drawing a perpendicular from the object glass's back point.

Actually, the main point does not coincide with the origin O of the coordinate system on the space image (Fig.2).

From expressions (1) and (3), upon adequate solution, we obtain:

$$\vec{\rho}_{kj} = \rho_{kj} \begin{bmatrix} \xi_{kj} \\ \eta_{kj} \\ \zeta_{kj} \end{bmatrix} = \frac{1}{D_{kj}} \rho_{kj} \vec{P}_o \begin{bmatrix} x_{k\bar{j}} - x_{ko} \\ y_{k\bar{j}} - y_{ko} \\ z_{k\bar{j}} - z_{ko} \end{bmatrix} = \begin{bmatrix} X_j - X_k \\ Y_j - Y_k \\ Z_j - Z_k \end{bmatrix} \tag{4}$$

Formulae (1)-(4) make it possible to determine the points from the space image in *satellite-centric inertial coordinate system.* But the coordinate georeference of the image must take place in the defined *Greenwich geo-centric coordinate system,* in which the satellite-centric radius-vector has the form:

$$\vec{\rho}_{kj} = \rho_{kj} \begin{vmatrix} \cos(\alpha_{kj} - S_k) \sin \delta_{kj} \\ \sin(\alpha_{kj} - S_k) \cos \delta_{kj} \\ \sin \delta_{kj} \end{vmatrix} = \rho_{kj} \begin{vmatrix} \xi_{kj} \\ \eta_{kj} \\ \zeta_{kj} \end{vmatrix} = \begin{vmatrix} X_j - X_k \\ Y_j - Y_k \\ Z_j - Z_k \end{vmatrix}, \tag{5}$$

S_k is the Greenwich star time, corresponding to the time t_k of receiving the space image. The coordinates of the SA - $(X,Y,Z)_k$ and the CP - $(X,Y,Z)_j$ are in the *Greenwich geo-centric coordinate system.*

From (4), the following relation may be written:

$$(6)\qquad \begin{bmatrix} x_{kj}-x_{ko} \\ y_{kj}-y_{ko} \\ z_{kj}-z_{ko} \end{bmatrix} = \frac{D_{kj}}{\rho_{kj}} \vec{P}_o^{\,T} \begin{bmatrix} X_j - X_k \\ Y_j - Y_k \\ Z_j - Z_k \end{bmatrix} = m\vec{P}_k \begin{bmatrix} X_j - X_k \\ Y_j - Y_k \\ Z_j - Z_k \end{bmatrix},$$

where:

$$(7)\qquad m_{kj} = \frac{D_{kj}}{\rho_{kj}} \text{ - scale factor and}$$

$$(8)\qquad \vec{P}_k = \vec{P}_o^{\,T} = \begin{bmatrix} a_1 & a_2 & a_3 \\ b_1 & b_2 & b_3 \\ c_1 & c_2 & c_3 \end{bmatrix}$$

The operator $\vec{P}_k = \vec{P}_o^{\,T}$ is an orthogonal matrix, performing the transition from the *Greenwich* into the *satellite-centric geo-centric coordinate system* through the *Euler angles* (Ω, w, i), namely (Fig.1):

(9)

$$\begin{cases} a_1 = \cos w\cos\Omega - \sin w\sin\Omega\cos i, & b_1 = -\sin w\cos\Omega - \cos w\sin\Omega\cos i, \\ a_2 = \cos w\sin\Omega + \sin w\cos\Omega\cos i, & b_2 = -\sin w\sin\Omega + \cos w\cos\Omega\cos i, \\ a_3 = \sin w\sin i, & b_3 = \cos w\sin i, \\ c_1 = \sin\Omega\sin i, & c_2 = \cos\Omega\sin i, \qquad c_3 = \cos i \end{cases}$$

From formula (6), according to formulae (7) and (8), we obtain:

$$(10)\qquad \begin{cases} x_{kj} = m_{kj}[a_1\Delta X_{kj} + a_2\Delta Y_{kj} + a_3\Delta Z_{kj}] + x_{ko} = m_{kj}\overline{N}_{kj} + x_{ko} \\ y_{kj} = m_{kj}[b_1\Delta X_{kj} + b_2\Delta Y_{kj} + b_3\Delta Z_{kj}] + y_{ko} = m_{kj}\overline{P}_{kj} + y_{ko} \\ z_{kj} = m_{kj}[c_1\Delta X_{kj} + c_2\Delta Y_{kj} + c_3\Delta Z_{kj}] + z_{ko} = m_{kj}\overline{Q}_{kj} + z_{ko} \end{cases},$$

where we have:

$\Delta X_{kj} = X_j - X_k$, $\Delta Y_{kj} = Y_j - Y_k$ and $\Delta Z_{kj} = Z_j - Z_k$

x_{kj}, y_{kj}, z_{kj} - coordinates of the images of the CP on the space image;

x_{ko}, y_{ko}, z_{ko} - coordinates of the main point of the space image;

X_j, Y_j, Z_j - geo-centric Greenwich coordinates of the CP from the Earth's surface;

X_k, Y_k, Z_k - geo-centric Greenwich coordinates of the SA's projection centre

a_i, b_i, c_i, i = 1,2,3 - elements of the orthogonal matrix $\vec{P}_k$, function of the Euler angles Ω, w, i

3. Preparation of an Algorithm to Determine the Equations of the Corrections and Unknown Variables for the Sought Quantities

To solve this problem, we shall start by assuming a number of settings and requirements, namely:

For each point $\bar{j}$ of the space image, which appears to be the image of a CP-j from the Earth's surface, we have twelve unknown variables, according to equations (10):

(11) $$X_j,\ Y_j,\ Z_j,\ X_k,\ Y_k,\ Z_k,\ \Omega_k,\ w_k,\ i_k,\ x_{ko},\ y_{ko},\ z_{ko}$$

whereas we shall denote their approximate values in the following way:

(12) $$X_j^o, Y_j^o, Z_j^o, X_k^o, Y_k^o, Z_k^o, \Omega_k^o, w_k^o, i_k^o, x_{ko}^o, y_{ko}^o, z_{ko}^o$$

Linearizing expressions (10) for each terrain control point j with coordinates $\bar{j} = (x \quad y \quad z)^T_{kj}$, projected onto the space image, the corrections equation is obtained:

(13) $$\vec{V}_{U_{kj}} = \begin{pmatrix} \vec{A}_k & \vec{B}_k & \vec{C}_j & \vec{D}_{ko} \end{pmatrix} \begin{pmatrix} d\vec{S}_k \\ d\vec{r}_k \\ d\vec{R}_j \\ d\vec{n}_{ko} \end{pmatrix} + \vec{L}_{kj}; \qquad P_{kj}$$

P_{kj} - weighing factor

The quantities $\vec{A}_k, \vec{B}_k, \vec{C}_j, \vec{D}_{ko}$ in the corrections equation (10) must be considered as partial differentials of the coordinates $x_{k\bar{j}}$, $y_{k\bar{j}}$, $z_{k\bar{j}}$, namely :

(14) $$\vec{A}_k = \frac{\partial(x,y,z)_{kj}}{\partial(\Omega,w,i)_{kj}}$$; (15) $$\vec{B}_k = \frac{\partial(x,y,z)_{kj}}{\partial(X,Y,Z)_{k(j)}}$$; (16) $$\vec{D}_{ko} = \frac{\partial(x,y,z)_{kj}}{\partial(x,y,z)_{ko}}$$

whereas $\vec{\bar{B}}_k = -\vec{C}_j$, the index "$k$" is differentiation along the coordinates of the SA, and the index "j" - differentiation along the coordinates of a CP from the terrain.

$$(17)\qquad \begin{cases} \vec{V}_{U_{kj}} = \left(v_x \quad v_y \quad v_z\right)_{kj}^T; \qquad d\vec{S}_k = \left(d\Omega \quad dw \quad di\right)_k^T; \\ d\vec{r}_j = \left(dX \quad dY \quad dZ\right)_K^{T'}; \quad d\vec{R}_j = \left(dX \quad dY \quad dZ\right)_j^T; \\ d\vec{n}_{ko} = \left(dx \quad dy \quad dz\right)_{ko}^T \end{cases}$$

$d\vec{S}_k, d\vec{r}_k, d\vec{R}_j, d\vec{n}_{ko}$ are the corrections for the approximate values (12) of the known (10) and unknown variables (11).

For the vector of the free term $\vec{L}_{kj}$ we have:

$$(18)\qquad \vec{L}_{kj} = \vec{U}_{kj} - \vec{U}'_{kj} = \begin{vmatrix} x_{kj} - x'_{kj} \\ y_{kj} - y'_{kj} \\ z_{kj} - z'_{kj} \end{vmatrix},$$

where:

$\vec{U}_{kj} = \left(x \quad y \quad z\right)_{kj}^T$ - the determined values for the coordinates x_{kj}, y_{kj}, z_{kj} after (10),

$\vec{U}'_{kj} = \left(x' \quad y' \quad z'\right)_{kj}^T$ - the measured coordinates from the space image.

4. Deriving expressions to determine the values $\vec{A}_k, \vec{B}_k, \vec{C}_j$

To obtain the private differentials according to expressions (14), (15) and (16), the following coordinates must be successively differentiated: x_{kj}, y_{kj}, z_{kj} with respect to the Euler angles (Ω, w, i); the space coordinates of the terrain CP-j with respect to $\left(X \quad Y \quad Z\right)_j$, *the Greenwich coordinates* of the SA with respect to $\left(X \quad Y \quad Z\right)_k$ and also with respect to the coordinate origin of the image $\left(x \quad y \quad z\right)_{ko}$.

4.1. Private differentials for the quantity $\vec{A}_k$

According to expression (14), it is not necessary to differentiate the image coordinates from (10) with respect to (Ω, w, i), accordingly - (9). But since only the quantities $a_i, b_i, c_i, (i = 1,2,3)$ are function of the Euler angles, we must differentiate $\overline{N}_{kj}, \overline{P}_{kj}, \overline{Q}_{kj}$ by the expressions:

$$(19)\left\{\frac{\partial x_{kj}}{\partial(\Omega,w,i)_k}=\frac{\partial(m_{kj}\overline{N}_{kj})}{\partial(\Omega,w,i)_k};\ \frac{\partial y_{kj}}{\partial(\Omega,w,i)_k}=\frac{\partial(m_{kj}\overline{P}_{kj})}{\partial(\Omega,w,i)_k};\ \frac{\partial z_{kj}}{\partial(\Omega,w,i)_k}=\frac{\partial(m_{kj}\overline{Q}_{kj})}{\partial(\Omega,w,i)_k}\right.$$

4.2. Private differentials for the quantities $\vec{B}_k = -\vec{C}_j$

As already mentioned above, to obtain the differentials of the image coordinates $(x,y,z)_{kj}$ with respect to $(X \quad Y \quad Z)_k^T$ and $(X \quad Y \quad Z)_j^T$, we must use expressions (10), from which it follows that both the scale $m_{kj}=\frac{D_{kj}}{\rho_{kj}}$, according to formula (7), and $\overline{N}_{ij}, \overline{P}_{kj}, \overline{Q}_{kj}$ are function of the Greenwich coordinates. Accounting for this fact, we shall differentiate by expressions

(20):

$$\left\{\frac{\partial x_{kj}}{\partial(X,Y,Z)_{k(j)}}=\frac{\partial(m_{kj}\overline{N}_{kj})}{\partial(X,Y,Z)_{k(j)}};\ \frac{\partial y_{kj}}{\partial(X,Y,Z)_{k(j)}}=\frac{\partial(m_{kj}\overline{P}_{kj})}{\partial(X,Y,Z)_{k(j)}};\ \frac{\partial z_{kj}}{\partial(X,Y,Z)_{k(j)}}\right.$$
$$\left.=\frac{\partial(m_{kj}\overline{Q}_{kj})}{\partial(X,Y,Z)_{k(j)}}\right.$$

5. Determination of the elements of the private differentials during coordinate georeference of space images

5.1. Formulae for the private differentials of the coordinates $(x,y,z)_{kj}$ with respect to the Euler angles $(\Omega,w,i)_k$

According to expressions (19), in order to obtain the elements of the differentials of linear equation system (10) with respect to $a_i, b_i, c_i, (i = 1,2,3)$, we must differentiate (9) with respect to the Euler angles $(\Omega,w,i)_k$, which results in:

$$(21)\qquad \begin{vmatrix} \frac{\partial x_{kj}}{\partial \Omega_k} \\ \frac{\partial x_{kj}}{\partial w_k} \\ \frac{\partial x_{kj}}{\partial i_k} \end{vmatrix} = m_{kj} \begin{vmatrix} \frac{\partial \overline{N}_{kj}}{\partial \Omega_k} \\ \frac{\partial \overline{N}_{kj}}{\partial w_k} \\ \frac{\partial \overline{N}_{kj}}{\partial i_k} \end{vmatrix} = m_{kj} \begin{vmatrix} -a_2 & a_1 & 0 \\ b_1 & b_2 & b_3 \\ c_1 \sin\omega_k & -c_2 \sin\omega_k & c_3 \sin w_k \end{vmatrix} \begin{vmatrix} \Delta X_{kj} \\ \Delta Y_{kj} \\ \Delta Z_{kj} \end{vmatrix}$$

$$(22)\qquad \begin{vmatrix} \frac{\partial y_{kj}}{\partial \Omega_k} \\ \frac{\partial y_{kj}}{\partial w_k} \\ \frac{\partial y_{kj}}{\partial i_k} \end{vmatrix} = m_{kj} \begin{vmatrix} \frac{\partial y_{kj}}{\partial \Omega_k} \\ \frac{\partial y_{kj}}{\partial w_k} \\ \frac{\partial y_{kj}}{\partial i_k} \end{vmatrix} = m_{kj} \begin{vmatrix} -b_2 & b_1 & 0 \\ -a_1 & -a_2 & -a_3 \\ b_3 \sin\Omega_k & -b_3 \cos\Omega_k & c_4 \end{vmatrix} \begin{vmatrix} \Delta X_{kj} \\ \Delta Y_{kj} \\ \Delta Z_{kj} \end{vmatrix}$$

$$(23)\qquad \begin{vmatrix} \frac{\partial z_{kj}}{\partial \Omega_k} \\ \frac{\partial z_{kj}}{\partial w_k} \\ \frac{\partial z_{kj}}{\partial i_k} \end{vmatrix} = m_{kj} \begin{vmatrix} \frac{\partial \overline{Q}_{kj}}{\partial \Omega_k} \\ \frac{\partial \overline{Q}_{kj}}{\partial w_k} \\ \frac{\partial \overline{Q}_{kj}}{\partial i_k} \end{vmatrix} = m_{kj} \begin{vmatrix} -c_2 & c_1 & 0 \\ 0 & 0 & 0 \\ c_3 \sin\Omega_k & -c_3 \cos\Omega_k & -c_4 = \sin i_k \end{vmatrix} \begin{vmatrix} \Delta X_{kj} \\ \Delta Y_{kj} \\ \Delta Z_{kj} \end{vmatrix}$$

5.2. Formulae for the private differentials of the coordinates $(x,y,z)_{kj}$ with respect to $(X,Y,Z)_{k(j)}$ at the time of receiving the image t_k

According to expressions (20), the elements of the private differentials may be obtained from expressions (10) with respect to the Greenwich coordinates of the SA - $(X,Y,Z)_{k(j)}$ at the time of exposure of the space image t_k, namely:

(24)

$$\begin{cases} \dfrac{\partial x_{k(J)}}{\partial (X,Y,Z)_{K(J)}} = \pm m_{K(J)} \left[\dfrac{\overline{N}_{KJ}}{\rho^2_{KJ}} (X_{KJ} + \Delta Y_{KJ} + \Delta Z_{KJ})^T \mp (a_1 + a_2 + a_3)^T \right] \\ \dfrac{\partial y_{K(J)}}{\partial (X,Y,Z)_{K(J)}} = \pm m_{K(J)} \left[\dfrac{\overline{P}_{KJ}}{\rho^2_{KJ}} (\Delta X_{KJ} + \Delta Y_{KJ} + \Delta Z_{KJ})^T \mp (b_1 + b_2 + b_3)^T \right] \\ \dfrac{\partial z_{K(J)}}{\partial (X,Y,Z)_{K(J)}} = \pm m_{K(J)} \left[\dfrac{\overline{Q}_{KJ}}{\rho^2_{KJ}} (\Delta X_{KJ} + \Delta Y_{KJ} + \Delta Z_{KJ})^T \mp (c_1 + c_2 + c_3)^T \right] \end{cases}$$

In expressions (24), for the indexes k and j we have accordingly k = 1, 2,...9 and j = 1,2,...9.

For the matrix C_j the values are the same, but the signs change, i.e., "+" becomes "-" and "-" becomes "+". In the above expressions, we have assumed that $\Delta x_{oj}, \Delta y_{oj}, \Delta z_{oj}$ are equal to:

(25) $$\Delta x_{oj} = x_{kj} - x_{ko}; \Delta y_{oj} = y_{kj} - y_{ko}; \Delta z_{oj} = z_{kj} - z_{ko}$$

The values of these quantities are determined from (14), i.e., these are the calculated coordinates of the images of the CPs.

The scale factor m_{kj} is determined from formula (10) for all terrain CP and their respective images on the space image.

5.3. Expression to determine the private differentials $(x,y,z)_{kj}$ with respect to $(x,y,z)_{ko}$

According to expression (16) and linear equation system (10), and taking into account that according to equation (10), in determining m_{kj} the distance D_{kj} from the image is used, formula (3), which is function of the coordinates of the main point x_{ko}, y_{ko}, z_{ko} of the image O assumes the form:

(25) $$D_{ko} = \begin{vmatrix} \dfrac{(x_{kj} - x_{ko})^2}{D^2_{ko}} & 0 & 0 \\ 0 & \dfrac{(y_{kj} - y_{ko})^2}{D^2_{ko}} & 0 \\ 0 & 0 & \dfrac{(z_{kj} - z_{ko})^2}{D^2_{ko}} \end{vmatrix}$$

The essential thing here is that the scale coefficient m_{kj} is calculated for each terrain CP, thereby providing us with the image deformation between each particular image point and the origin of the coordinate system.

The vector equation for the corrections (13) and the obtained values for the private differentials based on expressions (21)–(24) make it possible to present the corrections of the sought quantities and the corrections for the unknown variables in the following form:

(26)

$$V_{Xkj}=A_1d\Omega+A_2d\omega+A_3d\iota+K_1dX_k+K_2dY_k+K_3dZ_k+J_1dX_j+J_2dY_j+J_3dZ_j+dx_{k0}+l_{Xkj},$$

(27)

$$V_{Xkj}=B_1d\Omega+B_2d\omega+B_3d\iota+K_4dX_K+K_5dY_K+K_6dZ_K+J_4dX_J+J_5dY_J+J_6dZ_J+dy_{KO}+l_{Ykj}$$

(28)

$$V_{Zkj}=C_1d\Omega+C_2d\omega+C_3d\iota+K_7dX_K+K_8dY_k+K_9dZ_k+J_7dX_J+J_8dY_J+J_9dZ_J+dz_{kj}+l_{Zkj}$$

6. Calculation algorithm for the coordinates' georeference after the suggested mathematical model

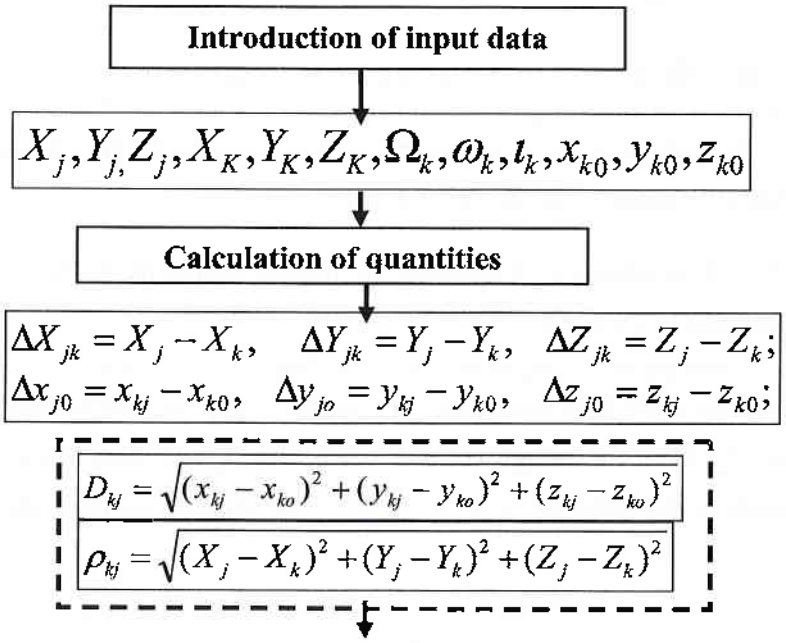

$$\begin{cases} a_1 = \cos w\cos\Omega - \sin w\sin\Omega\cos i, & b_1 = -\sin w\cos\Omega - \cos w\sin\Omega\cos i, \\ a_2 = \cos w\sin\Omega + \sin w\cos\Omega\cos i, & b_2 = -\sin w\sin\Omega + \cos w\cos\Omega\cos i, \\ a_3 = \sin w\sin i, & b_3 = \cos w\sin i, \\ c_1 = \sin\Omega\sin i, & c_2 = \cos\Omega\sin i, \quad c_3 = \cos i, \quad -c_4 = \sin i_k \end{cases}$$

$$\begin{cases} \overline{N}_{kj} = a_1\Delta X_{kj} + a_2\Delta Y_{kj} + a_3\Delta Z_{kj} \\ \overline{P}_{kj} = b_1\Delta X_{kj} + b_2\Delta Y_{kj} + b_3\Delta Z_{kj} \\ \overline{Q}_{kj} = c_1\Delta X_{kj} + c_2\Delta Y_{kj} + c_3\Delta Z_{kj} \end{cases}$$

Calculation
corrections equation (26) – (28)
and factors equation (21) – (24)

References

1. Георгиев, Н., Р. Недков, Ректификация на геометрическите деформации при космическите сканерни изображения чрез апроксимиращи функции, "Аеро-космически изследвания в България", 1998, кн. 15, София.
2. Георгиев, Н., Р. Недков, Д. Неделчева, Високоточен метод за координатно привързване и ректификация на космическите фотографски изображения, Сб. "30 год. организирани космически изследвания в България", ИКИ - БАН 2000, с. 124-131.
3. N. Georgiev, Nedkov R., Nedelcheva D. Using an Orbital Method and GPS Measurements of the Ground Control Point in Georeference of Space Images, Aerospace Research in Bulgaria, 16, 2001, pp. 70-80, Sofia.
4. П. Гецов, Космос, екология, сигурност, НБУ, Център за дистанционно обучение, С.,2002 г. с. 211.
5. N. Georgiev, Svetlin Fotev, Mathematical Model for Coordinate Attachment and Rectification of Space Images with High Resolution, Space Research Institute – BAS, 17, 2003, Sofia.
6. Petar Getsov, Space Technologies and the War in Iraq, Institute Research Space – BAS 2004, pp. 5 – 14, S.
7. N. Georgiev, Svetlin Fotev, Avram Stoyanov, Analysis of the Precision of the Georectification of the Satellite Imagery Using Distributory Data vs. Ground-Based GPS Measurements, Space Research Institute – BAS, 18, 2004.

8. У р м а е в, М. С., Орбитальные методы космического геодезии, М., "Недра", 1981, с. 286.
9. G o r d o n P e t r i e – Mapping Awareness, Nov.1999, Depart. of Topographic Science, University of Glasgow.

АЛГОРИТЪМ ЗА ВИСОКОТОЧНО ПРИВЪРЗВАНЕ И РЕКТИФИКАЦИЯ НА КОСМИЧЕСКИ ИЗОБРАЖЕНИЯ С ВИСОКА РАЗДЕЛИТЕЛНА ВЪЗМОЖНОСТ

Никола Георгиев

Резюме

Сегашното състояние на космическите изображения с висока разделителна способност, дават реална възможност за едромащабно картиране, обновление на съществуващи карти, мониторинг на земното покритие и окръжаващата среда и други практични, научни и отбранителни цели, при които е необходимо да се постигат високи точности при определяне взаимното разположение между отделни дискретни точки. [2,3,4,5,6,7,8,9]

На базата на многото изследвания у нас и в чужбина [4,7,9] се доказа, че резултатите от обработката на космическите изображения от доставчика и ползвателя, се различават чувствително по точност при привързването и ректификацията на изображенията. Това се получава когато ползвателя определя координатите на земните ОТ с GPS измервания и съответно вземе под внимание направените препоръки при обработката.

На основата на създадения математически модел [1,3,5] се разработи алгоритъм по който се изготвя софтуер за обработка и оценка на получения наблюдателен материал по метода на най-малките квадрати (МНМК).

Bulgarian Academy of Sciences. Space Research Institute.
Aerospace Research in Bulgaria. 19, 2005, Sofia

EARTH MAPPING – AERIAL OR SATELLITE IMAGERY COMPARATIVE ANALYSIS

Svetlin Fotev, Dimitar Jordanov, Hristo Lukarski

Space Research Institute, Bulgarian Academy of Sciences

Abstract

Nowadays, solving the tasks for revision of existing map products and creation of new maps requires making a choice of the land cover image source. The issue of the effectiveness and cost of the usage of aerial mapping systems versus the efficiency and cost of very-high resolution satellite imagery is topical [1, 2, 3, 4]. The price of any remotely sensed image depends on the product (panchromatic or multispectral), resolution, processing level, scale, urgency of task and on whether the needed image is available in the archive or has to be requested. The purpose of the present work is

- *to make a comparative analysis between the two approaches for mapping the Earth having in mind two parameters: quality and cost.*
- *to suggest an approach for selection of the map information sources – airplane-based or spacecraft-based imaging systems with very-high spatial resolution.*

Two cases are considered: area that equals approximately one satellite scene and area that equals approximately the territory of Bulgaria.

1. Introduction and purpose of the research

Launching into orbit the new generation of commercial satellite systems like IKONOS-2, EROS A1, SPOT 5, QuickBird and OrbView-3, opened a new era into Earth observation from open space. The optic sensors of these systems made it possible to combine very high-resolution (VHR) abilities with reduced revisit time. On the other hand, their navigation systems, GPS, gyro platforms and star trackers provide for precise geometrical modelling of the image assessment system. This allows extracting of geoproduct from raw data without using ground control points (GCP). This is possible at limited precision of the georectification. For example, the precision of the Standard product without GCP and 3D relief

model for IKONOS is 50 CE90 ± 25 m RMS [7]. *Table 1* contains the basic parameters of the currently active commercial satellites with VHR. It can be seen that the revisit time is between 1.5 and 5 days.
Now, the issue of the effectiveness and cost of the usage of aerial mapping systems versus the effectiveness and cost of VHR satellite imagery is topical. The price of any remotely sensed image depends on the product, resolution, processing level, scale, urgency of task, and on whether the needed image is available in the archive or has to be requested.
The aim of the present work is to make a comparative analysis between these two approaches for mapping the Earth having in mind two parameters: quality and cost. Two cases will be considered:

- Area that equals approximately to one satellite scene;
- Area that equals approximately to the territory of Bulgaria

2. Very High Resolution Satellite Imagery (VHRSI): products and prices

The prices of the satellite imagery we are received from the price lists of the distributor companies. As data for the analysis, we will use the prices of VHRSI for the four of the five commercial satellites (OrbView-3, of ORBIMAGE does not offer price list up to now). The data is presented on *Table 2*. The whole set of products offered by the companies is not presented on the table. Only two products are shown - radiometrically corrected and orthorectified. *Table 3* presents the prices for one scene and the estimated price for scenes covering the whole territory of Bulgaria (~ 111,000 km^2). The "losses" from scenes recovering will be compensated by price discounts for quantity. More information is available in the web sites [7, 8, 9, 10].
On *Table 2* and *Table 3*, the type of the product is shown with its original name from the price lists as follow:
For IKONOS [7]:

- *Geo Ortho Kit* – raw image that includes the camera geometry obtained at the time of image collection;
- *Precision* – the most positionally-accurate product, provides the spatial accuracy necessary for most urban planning applications, as well as cadastral and infrastructure mapping requirements (4.1 m CE90 ±1.9 m RMSE, require customer supplied GCPs and DEM);
- *Precision Plus* – the same as above (2.0 m CE90 ± 0.9 m RMSE, require customer supplied GCPs and DEM).

For EROS A1 [8]:

- *Archive* – product from archive

- *New* – product with coordinates and time required by the client

For QuickBird [9]:

- *Basic Imagery* – same as with the product *Geo Ortho Kit* of Space Imaging;
- *Standard Imagery* – radiometric, sensor and geometric correction, map projection with accuracy 23 m CE90 ±14 m RMSE;
- *Orthorectified Imagery* – same as above, but map projection accuracy is 12.7 m CE90 ±7.7 m RMSE, require customer supplied GCPs and DEM.

For SPOT-5 [10]:

- *Level 1A* – radiometric correction only;
- . *Level 3* – orthorectified, requires customer supplied GCPs and DEM.

3. Aerial Imagery: products and prices

We review aerial imaging systems from the type Wild RC10 and Zaiss RMK-TOP. The finest spatial resolution of the processed negative film is around 40 line pairs per mm (40 lp/mm). At scale 1:40,000, the finest resolution of 11 pl/mm on the film is equivalent to 1 m in terrain ground resolution. With the newer types of aerial cameras, such as Leica RC30 and Zaiss RMK-TOP, equipped with forward motion compensation (fmc) and gyro-controlled mounts, and utilising fine-grained film emulsions, the image resolution is 60 lp/mm. At scale1:60,000, the finest resolution on the film is again equivalent to a ground resolution of 1 m. It is important to note that for the newest commercial VHRSI the spatial resolution of 1m is equivalent to 2 m in terms of their actual ground resolution. In this context, the Kell factor gives the relationship that 1 line pair (lp) is roughly equivalent to 2 pixels [5]. The following international standard rates can be used to assess the cost of the digital photogrammetric mapping [2]:

- Aerial photography – 4,000 $ mobilization + 10 $ per image
- Scanning of photos – 15 $ per image
- Aerial triangulation – 25 $ per image
- Digital elevation model – 120 $ per image
- Digital orthophoto – 30 $ per image
- Mosaicking – 20 $ per image

The following strategy will be used for the price analysis (*Figure 1*),[11]:

1) At scale 1:40,000, the standard aerial photos sized 23x23 cm cover an area of 9.2x9.2 km and, at scale 1:60,000 - area of 13.8x13.8 km.
2) The photos are usually flown with overlap as follows:
   - Longitudinal – 60% ;
   - Lateral – 30%.

The neat area decreases by 72%, i.e. 0.40x0.70 = 0.28. At scale 1:40,000, the effective area is 23.6992 km^2 and, at scale 1:60,000 - 53.3232 km^2.

3) Longitude sampling:
$a_{1:40000} = 0.4 \cdot 9.2\ km = 3.68\ km$
$a_{1:60000} = 0.4 \cdot 13.8\ km = 5.52\ km$
4) Latitude sampling, b = 0.7 x 9.2 km = 6.44 km / 0.7 x 13.8 km = 9.66 km
$b_{1:40000} = 0.7 \cdot 9.2\ km = 6.44\ km$
$b_{1:60000} = 0.7 \cdot 13.8\ km = 9.66\ km$
5) Aerial span length (for one fuel charging), L=2,000 km,
6) Turnover, R~50 km [12].
7) For rough cost estimation of the area equalling approximately to one satellite scene we will use the square:
A x B = 11 km x 11 km
for IKONOS-2, EROS A1, QuickBird and
A x B = 60 km x 60 km
for SPOT-5.
8) For the territory of Bulgaria we will approximate using the square:
A x B = 430 km x 255 km.

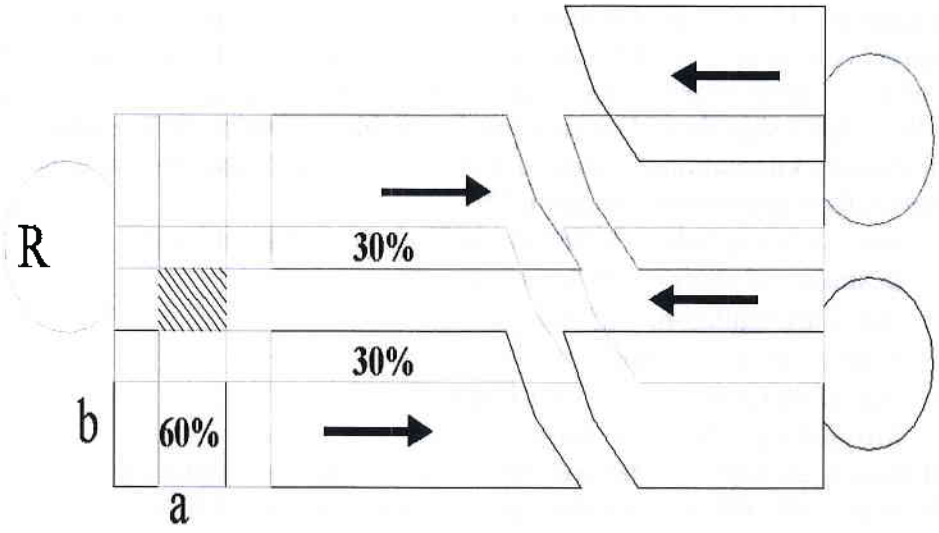

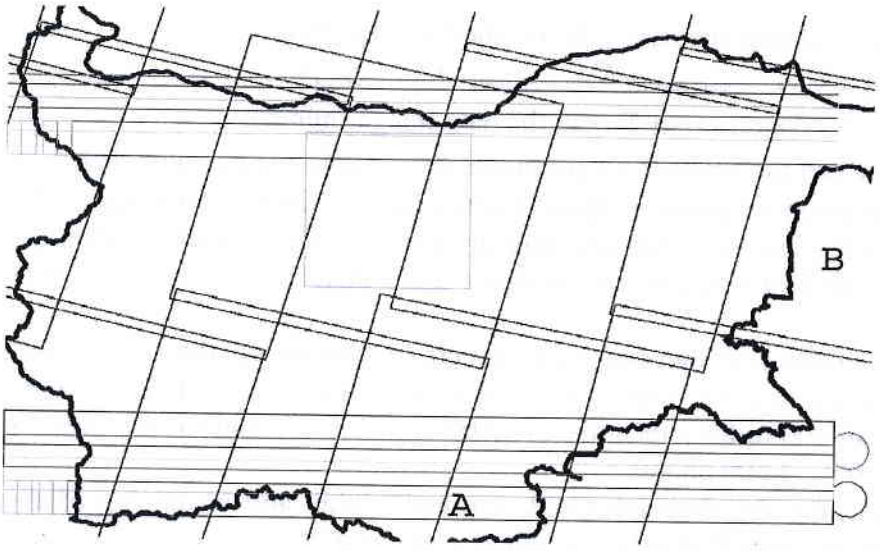

Fig. 1 Simplified model for fly all over the territory of Bulgaria – cost assessment

9) The number of the photos in one-track n_1:
$n_1 = \text{int}\{A/a\}$

10) The number of the tracks N:
$N = \text{int}\{B/b\}$

11) The number of the tracks for one take-off N_1:
$N_1 = \text{int}\{L/(A+R)\}$

12) The number of the photos n:
$n = n_1 \cdot N$

13) The number of the take-offs M:
$M = N/N_1$

14) Expenses for mobilizations C_a:
$C_a = M \cdot 4000\$$

15) Expenses for photo processing until photogrammetric processing C_i - they are determined by the total number of photos, the price of one photo and the price of scanning:
$C_i = n \cdot (C_{image} + C_{scanning\ of\ photos})$

16) Finally we can write down for the expenses on airplane and photos until photometric processing C_{raw}:
$C_{raw} = C_a + C_i$

17) The value of airplane triangulation and the mosaicing:

$$C_{ph} = n \cdot (C_{aerial\ triangulation} + C_{digitalorthophoto} + C_{mosaicking})$$

Note. int{...} - denotes rounding to the next integer number

The results from the analysis are presented on Table 4. We can note that:

- The price of aerial images depends mainly on the territory of the analyzed area. The price for analysis organization and implementation for areas between 100 and 500 km^2 is times more than the one for areas over 3,000 km^2.
- The time and the expenses related to converting the photos into digital type are also of importance. While for a territory of 121 km^2 their number is around 6, for a territory of 3,600 km^2 it is 170 and for the territory of the country – 4,800 photos.
- The time for choosing GCP, georectification and mosaicing of the different photos should also be taken into consideration.

4. Compatible analysis and conclusions

Taking into consideration the results presented on *Tables 2, 3, 4,* we shall make a compatible assessment between aerial images and VHRSI aiming at large scale mapping. While comparing costs, we shall use the price of different analyzed areas that equal 1 km^2 .We shall compare digital raw images (*Table 5*) and images that are georeferenced with defined precision (*Table 6*).

Conclusions relating to area-price factors:

- When the area that has to be photoed and analyzed equals one or several satellite scenes, it is better in terms of price to use satellites.
- When the area that has to be photoed and analyzed is times more than one or several satellite scenes, it is better in terms of price to use aerial imagery. At the same time, it is necessary to take into account the deadlines for fulfilling the task versus the volume of work into man months.
- The cost of the geoproduct from SPOT-5 satellite with pixel 2.5 m is comparable to the one of aerial imagery even for areas over 50,000 km^2;
- It is important to make very careful analysis of the necessary special resolution of the imagery that will be used. *Tables 6* and *7* show that a change-over in special resolution from ~ (0.61– 1) m to 1.8 m reduces the cost price 4-5 times and from ~ (0.61–1) m to 2.5 m - 9-10 times;

• The price of the product will increase 5-6 times to receive a georeferenced product with precision compatible with the pixel of the raw image. At the same time, it is necessary to present to the client the CGP and the 3D model of the relief.

Conclusions relating to time for execution factor:

• Thanks to the precise navigation systems, the new generation satellites allow obtaining rectified-to-a-datum and map-projected product ready for integration in GIS. The accuracy is much less than the pixel size of the scanning system, but for map scales like 1:50,000 it is completely satisfying [8]. This product could be obtained within less than 48 hours.

• Apart from the panchromatic channel, the new generation satellites have several multispectral channels with lower special resolution. Data fusion techniques allow express change detection and estimation of the land cover;

• To obtain the image throughout the territory of interest, aerial photos need in addition digital scanning, triangulation and mosaicing (overlapping - longitudinal – 60%, lateral – 30%); in relation with this, the processing of large number of aerial photos requires greater operation time and human resources.

Appendix

Таблица 1. **Satellites and Sensors – very-high resolution satellite imagery**

Satellite	Company Country Launching	Sensor	Pixel size, m	FOV along/across swatch, km	$H_{орб}$, км Revisit time, days
IKONOS-2	**Space Imaging EOSAT, USA 24.09.1999**	**Pan/MSI (13816/3454) Pushbroom,11 bit f=10000mm**	**0.82*/1 pan 3.2*/4 sp**	**±45⁰/±45⁰ 11**	**680 2,9 (1m)/ 1.5 (1.5m)**
EROS A1	**ImageSat Internat. N.V. Cyprus/Israel 05.12.2000**	**Pan (7000) Pushbroom**	**1.8 pan**	**±50⁰/±50⁰ 13.5**	**480 3**
QuickBird	**Earth Watch USA 18.10.2001**	**Pan/MSI (27000/6700) Pushbroom,11 bit**	**0.61 pan 2.44 sp**	**±30⁰/±30⁰ 16.5**	**450 1 - 3.5**
OrbView-3	**ORBIMAGE USA 26.06.2003**	**Pan/MSI (8000/2000) Pushbroom,**	**1 pan 4 sp**	**±50⁰/±50⁰ 8**	**470/3**
SPOT-5	**SPOTIMAGE France 02.05.2002**	**HRVIR (12000/6000) Pushbroom,**	**2.5, 5, 10, 20**	**±20⁰/±27⁰ 60-120**	**822 24 nadir/5**

Таблица 2. **Price list - IKONOS-2, EROS A1, QuickBird and SPOT-5, at 20. Jan 2004, [8,9,10,11].**
The prices are based on an area of 1 km^2.

Product, USD[*1]/km$_2$	IKONOS – 2 1 m		EROS A1 1.8 m	
	B&W	***All***	***B&W***	***All***
Radiometric correction	**21.50 Geo Ortho Kit**	**24.75 Geo Ortho Kit**	**5.00 Archive 8.25 New**	**N/A**
Radiometric correction & Georectified	**100 Precision 120 Precision Plus**	**110 Precision 125 Precision Plus**	**N/A**	**N/A**

Product, USD[*1]/km$_2$	QuickBird 0.61 m		SPOT-5 2.5 m	
	B&W	***All***	***B&W***	***All***
Radiometric correction	**22.50 Basic Imagery 23m CE90 ±14 RMSE**	**30.00 Basic Imagery 23m CE90 ±14 RMSE**	**1.875 Level 1A 2.15[*2] Level 1A**	**N/A**
Radiometric correction & Georectified	**90 Ortho Imagery 12.7m CE90 ±7.7 RMSE**	**117 Ortho Imagery 12.7m CE90 ±7.7 RMSE**	**2.125 Level 3 2.40[*2] Level 3**	**N/A**

[*1] **– The prices for SPOT - in USD (rate of exchange at 20.01.2004 EURO/USD – 1.25)**
[*2] **– require additional satellite programming = 3900$**
B&W **– panchromatic**
All **– panchromatic + all multispectral**

Table 3. **Approximate prices for VHRSI (0.61 – 2.5 m), radiometrically corrected, georectified.**
The prices are based on the territory of Bulgaria

Based on an area of 111000 km^2	IKONOS – 2[*1] 1 m		EROS A1 1.8 m	
	B&W	All	B&W	All
Raw product, per scene	2600 Geo Ortho Kit	3540 Geo Ortho Kit	910 Archive 1500 New	N/A
Raw product, all territory	2 386500 Geo Ortho Kit	3 246750 Geo Ortho Kit	555 000 Archive 915 750 New	N/A
Rectified per scene	12100 Precision 14520 Precision Plus	13310 Precision 15125 Precision Plus	N/A	N/A
Rectified all territory	11 100000 Precision 13 320000 Precision Plus	11 655000 Precision 13 875000 Precision Plus	N/A	N/A

Based on an area of 111000 km^2	QuickBird[*1] 0.61 m		SPOT-5 2.5 m	
	B&W	All	B&W	All
Raw product, per scene	6120 Standard Imagery 23m CE90 ±14 RMSE	8160 Standard Imagery 23m CE90 ±14 RMSE	6 750 Level 1A 7 750 Level 3	N/A
Raw product, all territory	2 500 000 Standard Imagery 23m CE90 ±14 RMSE	3 330 500 Standard Imagery 23m CE90 ±14 RMSE	208 000 Level 1A 240 000 Level 3	N/A
Rectified per scene	24 000 Standard Imagery 12.7m CE90 ±7.7 RMSE	32 000 Standard Imagery 12.7m CE90 ±7.7 RMSE	7 700 Level 1A 8 700 Level 3	N/A
Rectified all territory	9 990000 Standard Imagery 12.7m CE90 ±7.7 RMSE	12 987000 Standard Imagery 12.7m CE90 ±7.7 RMSE	236 000 Level 1A 266 000 Level 3	N/A

Table 4. **Rough estimation of an aerial photos price - GIS compatible data.**

Parameters		Photo 1:40 000 9.2 km x 9.2 km 1 m			Photo 1:60 000 13.8 km x 13.8 km 1 m		
		121 km²	3600 km²	111 000 km²	121 km²	3600 km²	111 000 km²
Photos per track, n_t		3	17	117	2	11	78
Number of the track, N		2	10	40	2	7	27
The number of the tracks for one takeoff, N_t		34	19	4	34	19	4
Total number of the photos, n		6	170	4680	4	77	2106
The number of takeoff, M		1	1	10	1	1	7
Airplane mobilization, C_a, $		4000	4000	40 000	4000	4000	28 000
Price of the photos , C_f, $		150	4250	117 000	100	1925	52 650
Raw data price $C_{raw} = C_f + C_a$, $		4150 34.20/km²	8250 2.30/km²	157 000 1.40/km²	4100 34.20/km²	5925 1.65/km²	80 650 0.75/km²
Processing price, C_{photo} , $	Triang + Mosaic	450 3.70/km²	4250 1.20/km²	351 000 3.20/km²	300 2.50/km²	5775 1.60/km²	158 000 1.40/km²
	DEM	720 5.60/km²	20 400 5.70/km²	562 000 5.10/km²	480 4.00/km²	9240 2.60/km²	252 000 2.30/km²
C [$], +Triang + Mosaic		~ 4 600 38.00/km²	~ 12 500 3.50/km²	~ 510 000 4.60/km²	~ 4 400 36.40/km²	~ 11 700 3.25/km²	~ 240 000 2.15/km²
C [$], +DEM		~ 5 320 44.00/km²	~32 900 9.10/km²	~1 072 000 9.70/km²	~ 4 880 40.30/km²	~ 20 940 5.80/km²	~ 492 000 4.45/km²
C_1 [$/km²], Raw		34.30	2.30	1.40	33.90	1.65	0.70
C_1 [$/km²], +Triang + Mosaic		38.00	3.50	5.60	36.40	3.25	2.20
C_1 [$/km²], +DEM		44.00	9.10	9.70	40.30	5.80	4.45

Table 5. **Comparison cost assessment between aerial photos and VHRSI, raw digital data.**
The prices are based on tested area of 121 km² , 3600 km² , 111 000 km² reduced to 1 km².

	Продукт	Пиксел	121 km²	3600 km²	111000 km²
Aerial photo	9.2 x 9.2 km 1:40 000	1 m	34.20	2.30	1.40
Aerial photo	13.8 x 13.8 km 1:60 000	1 m	34.15	1.65	0.75
IKONOS – 2	B&W	1 m	22,50	22.50	22.50
EROS A1 - Archive/New	B&W	1.8 m	5.00 / 8.25	5.00 / 8.25	5.00 / 8.25
QuickBird	B&W	0.61 m	22.00	22.00	22.00
SPOT-5 – Archive/New	B&W	2.5 m	1.90 / 8.70 + 2.10*1	1.90 / 1.10 + 2.20	1.90 / 2.20

Table 6. **Comparison cost assessment between aerial photos and VHRSI, rectification, mosaicing, DEM.**
Prices are based on tested area of 121 km^2 , 3600 km^2 , 111 000 km^2 , reduced to 1 km^2.

	Продукт	Пиксел	Точност	121 km^2	3600 km^2	111000 km^2
Aerial photo	9.2 x 9.2 km 1:40 000	1 m	1m	38.00	3.50	5.60
Aerial photo	13.8 x 13.8 km 1:60 000	1 m	1m	36.40	3.25	2.15
IKONOS – 2 Precision &Precision Plus	B&W	1 m	4.1 m CE90 2.0 m CE90	100.00 120.00	100.00 120.00	100.00 120.00
EROS A1	B&W	1.8 m	N/A	N/A	N/A	N/A
QuickBird Standard Imagery	B&W	0.61 m	23.0 m CE90 12.7 m CE90	22.50 90.00	22.50 90.00	22.50 90.00
SPOT-5 – Archive Level 3	B&W	2.5 m	5m	2.10	2.10	2.10
SPOT-5 – New Level 3	B&W	2.5 m	5m	8.70 + 2.40[*1]	1.10 + 2.40	2.40

[*1] **– The price increases as a result of satellite programming – 3900$.**
Sum total normalizes to the area (121 km^2 - to 450 km^2 – 1/8 scene, minimum required area)

References

1. Konecny, G. and J. Schiewe, 1996. Mapping from digital satellite image data with special reference to MOMS-02, ISPRS Journal of Photogrammetry & Remote Sensing, no. 51, pp. 173-181
2. Konecny, G., 2002. Mapping from Space, 23rd Asian Conference on Remote Sensing (Invited Paper), Kathmandu, Nepal, November 25-29, 2002
3. Jacobsen K., 2002. State-of-the-art Trends in Mapping – Past, Present, Future, INCA Workshop 2002, Ahmedabad, India
4. Konecny, G., 2001. Geodata and Information Systems – a German Perspective, United Nations Cartographic Conference for the Americas New York, N.Y., January 2001,pp.22-26,
5. Petrie, G. 1999, Characteristics and Applications of High-Resolution Space Imagery, Survey Ireland, Winter
6. High-Resolution Satellite Imagery and Resource Management, University of Minnesota, Remote Sensing & Geospatial Analysis Laboratory, Fact Sheet 3, http://rsl.gis.umn.edu/factsheet.html

КАРТИРАНЕ НА ЗЕМНАТА ПОВЪРХНОСТ - АЕРО- ИЛИ САТЕЛИТНИ ИЗОБРАЖЕНИЯ СРАВНИТЕЛЕН АНАЛИЗ

Светлин Фотев, Димитър Йорданов, Христо Лукарски

Резюме

Бързите промени в заобикалящата ни среда и навлизането на новите технологии намали изключително времевия интервал за актуализиране на съществуващите карти – топографски, тематични и други. Актуализацията на картната информация в момента е един от главните проблеми на картографията в световен мащаб [1,2,3,4]. Особено актуален в тази връзка става въпроса за ефективността и себестойността на използваните за тази цел аеро- и/или сателитни изображения. Цената на всяко изображение на земната повърхност, получено чрез дистанционни методи, зависи от спектралния тип на продукта, пространствената разделителна способност, нивото на обработка, мащаба, сроковете за решаване на задачата и, дали исканото изображение присъства в архива или тепърва трябва да бъде получено. Целта на представената работа е

- да направи сравнителен анализ между тези два подхода за картиране на земната повърхност, вземайки пред вид два параметъра – качество и цена;
- да предложи подход за избор на източника на картна информация – аеро- или сателитно изображение - в зависимост от типа на решаваната задача.

Разгледани са два случая: площ, съизмерима с площта на една или няколко сателитни сцени и площ, съизмерима с територията на България.

Bulgarian Academy of Sciences. Space Research Institute.
Aerospace Research in Bulgaria. 19, 2005, Sofia

METHOD FOR DETERMINATION OF THE FREQUENCY-CONTRAST CHARACTERISTICS OF ELECTRONIC-OPTIC SYSTEMS

Garo Mardirossian, Zhivko Zhekov

Space Research Institute, Bulgarian Academy of Sciences

Abstract

The frequency-contrast characteristics is an important criterion to judge the quality of electronic-optic systems, which boast an increasing application in space research, astronomy, martial art etc. The paper provides a brief description of the methods for determining the frequency-contrast characteristics of optic systems, developed at the Space Research Institute of the Bulgarian Academy of Sciences. The suggested methods have been used to develop a couple of electronic-optic systems participated in the designed ground-based and aerospace scientific-research equipment. Based on the obtained practical results, the conclusion was made that the methods provide to obtain sufficiently precise data, which coincide well with the results, obtained when using other methods.

Electronic-optic systems boast an increasing application in space research, astronomy, physics etc. [1, 2, 3]. They are used not only as amplifiers and converters of UV and IR emissions, for registration of continuous signals, but also as autonomous image receivers, inclusive for the purpose of determining the coordinates of remote subjects.

An important evaluation criterion for the quality of electronic-optic systems is the measured value of the frequency-contrast characteristics (FCC) [4, 5]. The well-known and most widely used methods to determine the FCC are based on using the Mira tables with sine contrast change and mechanical scanning of the generated image [6].

The paper provides a description of suggested methods for determination of the FCC of electronic-optic systems that has been developed at the Space Research Institute of the Bulgarian Academy of

Sciences in relation with the ongoing work on the developed electronic-optic systems for ground-based aerospace research apparata.

The image from the stroke Mira is projected by the object-glass onto the photocathode of the electronic-optic converter (EOC). Then, from the screen of the EOC, the image is scanned perpendicularly to the strokes and, through a photo-electronic multiplier (PEM), in photon-counting mode; the illumination brightness of the EOC's screen at some particular point (coinciding with the screen radius) of the Mira table image along the scanning axis is recorded.

Using a set of Mira touch tables of various spatial frequency υ, the contrast $K(\upsilon)$ may be calculated:

$$K(\upsilon)=\frac{L_{max}-L_{min}}{L_{max}+L_{min}}, \tag{1}$$

where L_{max} and L_{min} are accordingly the maximal and minimal brightness of the Mira touch image.

The FCC is determined by the expression [7, 8]:

$$F(\upsilon)=\frac{4}{\pi}[K(\upsilon)-K(3\upsilon)+K(5\upsilon)]. \tag{2}$$

Formula (2) makes it possible to determine theoretically the FCC.

In the present contribution, using Universal Night Vision Device Verification .Equipment (UNVDVE) [6], scanning the image from a single slit of width 2t, the amplitude corresponding to N touches from the Mira table has been recorded.

The FCC of an image representing a set of N touches of a slit of width 2 will be:

$$F(\upsilon)=\frac{\sin 2\pi\upsilon tN}{2\pi\upsilon tN}. \tag{3}$$

The analysis of (3) reveals that, when the number of touches in the Mira table is increased, the expression tends to zero; therefore, it is expedient to operate with a single slit. Moreover, at:

(4) $$\upsilon \to \frac{1}{2t} F(\upsilon) \to 0 \ .$$

Consequently, to expand the measured area of υ, 2t should be reduced.
Using the a.m. equipment [6] and the suggested formulae, the FCC of electronic-optic systems with a micro-channel plate (MCP) has been measured. When the size of the used Mira is commensurable with the diameter d of the MCP plate, the contrast of its image depends on the position with respect to the center of the MCP channel, whereas at coincidence with insensitive boundary between channels it is minimal, and at coincidence with the center it is maximal.

The determination of the FCC is reduced to measurement of the FCC of the overall system

(5) $$F(\upsilon) = F_1(\upsilon).F_2(\upsilon).F_3(\upsilon) \ ,$$

where: $F_1(\upsilon)$ – the FCC of the object glass;

$F_2(\upsilon)$ – the FCC of the EOC with MCP;

$F_3(\upsilon)$ – the FCC of the eye-lens of the electronic-optic system.

The most essential and precise moment here is to determine the $F_2(\upsilon)$, accounting that $F_1(\upsilon)$ and $F_3(\upsilon)$ feature higher resolution, i.e. higher FCC. The measurement time of the FCC of the EOC with MCP with spatial frequency of 2 to 22 double lines per mm is 5 min.
The results from the measurement of the FCC are shown in Fig. 1, Fig. 2 and Fig. 3.

A major factor determining the FCC is the system's focusing property. As a result of the insignificant dissipation by direction and energy of the outgoing electrons from the MCP channels, a point at the MCP's input is pictured on the EOC's screen as a circle.

Apart from this, the FCC is influenced by system noises, mostly spatial ones. Temporary noises are caused by the fluctuations of the recorded emission and by the channels' amplification factor. They are manifested when weak signals are recorded and they deteriorate the resolution of the electronic-optic system.

Spatial noises are caused mostly by dissipation depending on the diameter of the MCPs and accordingly, the amplification factor K, depending on the ratio between the channel length l and diameter d.

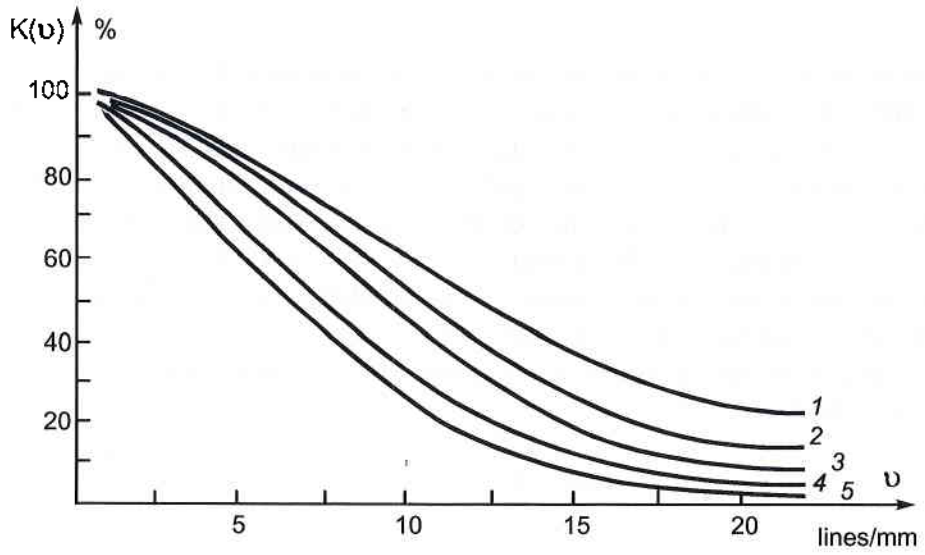
K(υ)
%
100
80
60
40
20
5
10
15
20
lines/mm
υ
1
2
3
4
5

Fig. 1

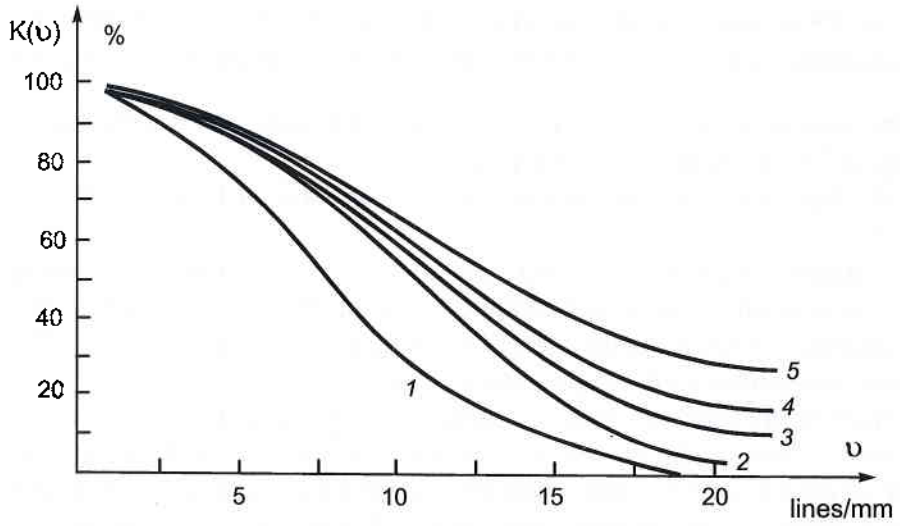
K(υ)
%
100
80
60
40
20
5
10
15
20
lines/mm
υ
1
2
3
4
5

Fig. 2

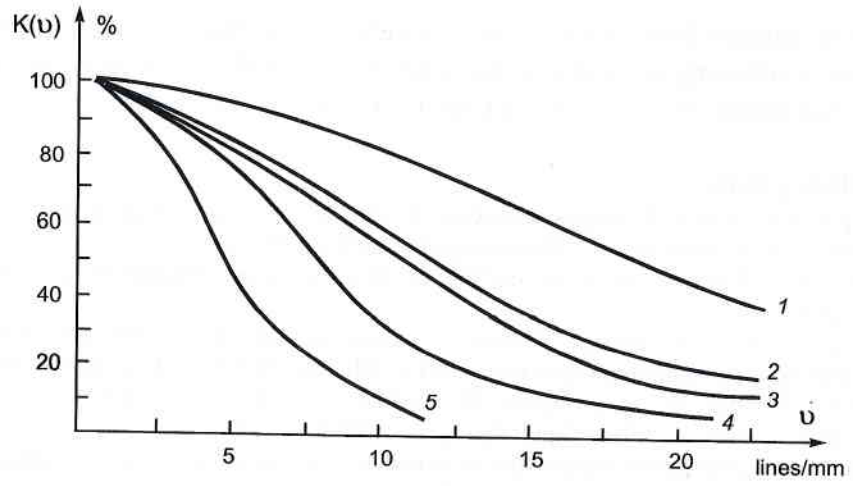

Fig. 3

The dependence of the FCC of an electronic-optic system with MCP on the voltage of the MCP is shown in Fig.1. It can be seen from the shown curves that when increasing the electric voltage u, the system's FCC gradually deteriorates. This can be attributed to the increase of the dissipation by direction and energy of the outgoing electrons from the MCP channels.

The dependence of the FCC on the potential difference applied between the MCP and the cathode-luminescence screen is shown in Fig.2. Increasing the voltage up to a certain value enhancing the focusing properties of the electrostatic lens and contributes to a more contrast image of the Mira table touches on the cathode-luminescence screen, whereas the FCCC increases as well.

In Fig. 3, the FCC of an EOC with MCP depending on the diameter d of the MCP channel is shown. The measurements were performed by an EOC with MCP with channel diameter d of 8 μm, 10 μm, 12 μm, 20 μm and 40 μm. Because there is no EOC with MCP with d = 6,4 μm, no such study was performed. Comparing curves 2, 3, 4 and 5, it may be seen that, when the MCP channel diameter is increased, the FCC deteriorates as a result of lowering the FCC of the individual channel [9].

Finally, based on the obtained results it may be concluded that the suggested method provides to obtain data with sufficient reproducibility and precision, coinciding well enough with the results obtained by using other methods.

The authors believe that it is expedient to use the FCC as a unified parameter in selecting electronic-optic systems for construction of scientific-research equipment, inclusive for aerospace application.

References

1. Мардиросян, Г. Аерокосмически методи в екологията и изучаването на околната среда. Акад. издат. "Марин Дринов", 2003, 208 стр.
2. Гецов, П. Космос, екология, сигурност. Нов български университет, София, 2002, 211 с.
3. Филипов, Л. Проект "Шипка" – експерименти по космическа физика. Сб. доклади "10 години космически проект "Шипка", ИКИ – БАН, София, 1999, с. 29–32. Wilcock, W., D. Emberson, B. Weekly. Trans. Inst. Radio. Engvs., N 5–7, 126, 2000. Mandel, L., J. Brit. Appl. Phys., N 10, 1990, p. 233.
4. Универсална контролна апаратура за проверка на прибори за нощно виждане УКНП. Военно издателство, София, 1995.
5. Fowle, F. Appl. J., 42, 2000, p. 233.
6. Meinel, A. Appl. J., 13, 1999, p. 241.
7. Drangard, R. JOSA, 1994, vol. 54, N 7, pp. 907–916.

МЕТОДИКА ЗА ОПРЕДЕЛЯНЕ НА ЧЕСТОТНО-КОНТРАСТНАТА ХАРАКТЕРИСТИКА НА ЕЛЕКТРОННО-ОПТИЧНИ СИСТЕМИ

Гаро Мардиросян, Живко Жеков

Резюме

Честотно-контрастната характеристика е важен критерий за качеството на електронно оптичните системи, които намират все по-голямо приложение и в космическите изследвания, астрономията, военното дело и т.н. В статията е описана накратко разработената в Институт за космически изследвания при Българска академия на науките една методика за определяне на честотно-контрастната характеристика на оптичните системи. Предложената методика е използвана при създаването на няколко електронно-оптични системи в състава на разработените наземни и аерокосмически научно-изследователски апаратури. На базата на получените резултати от реалната практика резултати е направен изводът, че методиката позволява получаване на достатъчно точни данни, които добре съвпадат с резултатите, получени при използването на други методи.

Bulgarian Academy of Sciences. Space Research Institute.
Aerospace Research in Bulgaria. 19, 2005, Sofia

ALGORITHM FOR DARK CURRENT CHARACTERIZATION OF IMAGING SPECTROMETER MODULE

Valentin Atanassov, Georgi Jelev

Space Research Institute, Bulgarian Academy of Sciences

Abstract

The paper presents some of the results obtained in the process of laboratory tests of an imaging spectrometer model for remote sensing applications. The main dark current characterization procedures are described and highlighted. An algorithm for dark current characterization is proposed and implemented and the obtained results are shown.

Keywords: *remote sensing, imaging spectrometers, dark current characterization.*

1. Introduction

Imaging spectrometry (spectroscopy) has established itself as a basic method for studying the Earth's surface [1, 2]. At the same time, imaging spectrometry measurements, as a new area in remote sensing, require new approaches with regard to data handling, preprocessing and information extraction from spectral images. These approaches are an important part of the analysis of imaging spectrometry data and are binding on a quantitative estimation of the data. They imply accomplishment of characterization procedures, including sensor-detected effects corrections, such as offset and dark current corrections, spectral and geometric corrections, etc.

Measurement quality is the toughest problem in imaging spectrometry. Practical instruments which are used are always non-ideal and optical measurements are only approximated. Consequently, interpretation of obtained data is somewhat undetermined and is often dependent on the adopted assumption about the measured object [1]. Therefore,

characterization procedures are carried out in parallel with the main instrument development to allow an efficient trade-off between the instrument's complexity and the system's performance, leaving correct interpretation of obtained data [3, 4]. It is strongly recommended that the instrument's development be attended by characterization process, since characterization methods are critically dependent on the instrument's design and construction, and performance requirements [5].

2. Dark current characterization

Characterization procedures start in parallel with the major instrument's development with planning and implementing methods for laboratory characterization and foreseen methods for on-board characterization.

The "dark current" term comes from the fact that this current is not relevant to sensor-surface-incident radiation. It is caused by thermo-generated electrons in silicon CCD structures, a process observed equally well in complete darkness. Some of the charge will collect in the sensor potential holes where useful-signal image-related electrons are collected. At the detector output, dark-current-generated electrons appear, identical to signal-generated electrons, so dark current appears as noise in the image.

At given temperature and sensor operating condition, dark current is relatively constant for each pixel and it appears as fixed signal offset. On the other hand, dark current varies spatially across the array. By capturing a series of images in complete darkness and averaging a pixel-to-pixel representation of the average dark current can be obtained at given temperature (Fig.1). Subtracting this reference dark image from subsequently captured real images partially eliminates the influence of the dark current (Fig.2). This is so the called dark current correction.

Unfortunately, dark current influences not to be completely eliminated. Except for the relatively constant component Uccij, dark current has a second randomly varying component ΔUcij, which is approximated as the square root [6] of the dark current, collected in the pixel (Fig.2).

Another complicating fact is that dark current will change when changing the sensor's operation mode, such as integration time, shift rate (Fig.1, 3). The size of the charge packet Q_p collected on a definite element is proportional to the integration time t, when the photo generated charges fill only partly the potential well within the integration period of the luminous flux Φ:

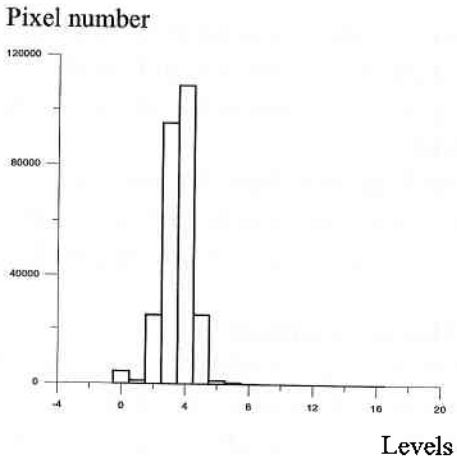

Fig. 1 Distribution of dark current levels for imaging spectrometer operating condition at integrated time t_i = 80ms.

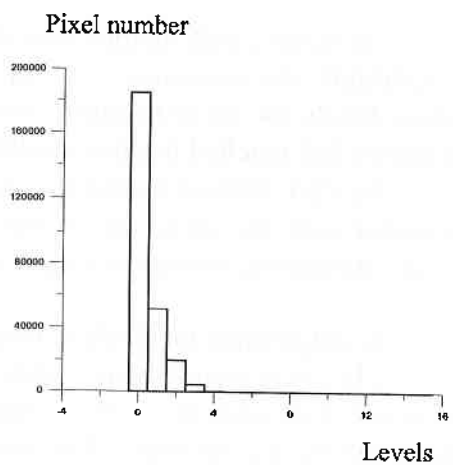

Fig. 2 Distribution of dark current levels after dark current correction, integrated time t_i = 80ms.

$$Q_p = q\Phi T_{tr}\eta t[1-\exp(-a\chi)/(1+aL_n)], \qquad (4),$$

where: a is the absorption coefficient of the material, T_{tr} – the transmission coefficient of the multi-layer structure, η - the quantum yield of the photo-emissive effect, χ - the depletion layer width, L_n – the diffusion length.

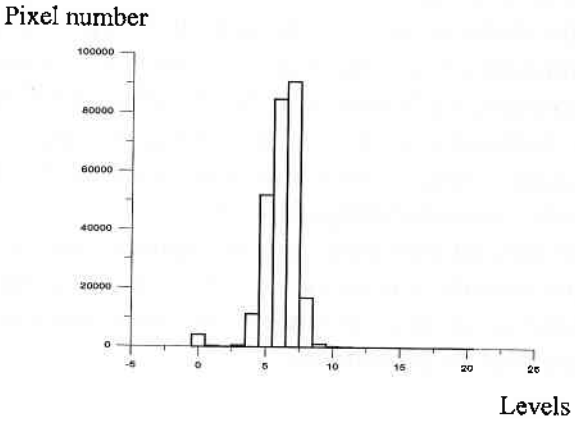

Fig. 3 Distribution of dark current levels for imaging spectrometer operating condition at integrated time t_i = 100ms.

Therefore, with change of operation mode, noise levels also change. To calibrate the instrument for these variations, one should store dark current levels for each operation mode and these should not be valid until the sensor had reached thermal equilibrium.

As dark current increases twice with temperature increase of 8°C, it decreases with the same rate when the sensor is cooled. For that reason, sensor cooling and operation temperature stabilization [7, 8] are required.

3. Algorithm for dark current characterization

The measurements are made in laboratory conditions; they aim to determine dark current levels' variation for each pixel of the sensor array. These laboratory-obtained data are stored for reference with on-board obtained data. In operation mode, during nominal observation, offset correction is performed by subtracting the dark level component from the signal. Dark current correction coefficients are obtained by closing the shutter, dark current levels Ucij are given by the detector response and are stored for further processing. The processing involves calculation of the average dark current level for each pixel in image and storage data for implementation of the characterization algorithms. These procedures must be performed for each possible sensor operation mode. The process of dark current characterization is indicated in the flow chart shown in Fig. 4.

The process of dark current characterization - capturing images, subtracting, storage (Fig.4) takes time and computational power, but in the corrected images, the dark current's effect is partially eliminated and quality is dramatically improved (Fig.5, 6). For example, in a system with 8-bit (256 levels) quantization, each level can hold 1/256 of full-well capacity. Each pixel has a dark-current-caused amounting to approximately 6.21 levels. Following dark current correction, dark current is reduced to 0.4 levels, as shown in the corrected image (Fig.5b).

It should be noticed that dark current characterization is only a part of a complex characterization process typical of an imaging spectrometer and it can be regarded as an integral component of the following radiometric and spectral characterization procedures.

4. Conclusions

1. The dark current characterization procedures, carried out as indicated in the proposed algorithm, result in an essential decrease of dark current levels in the corrected spectral images.

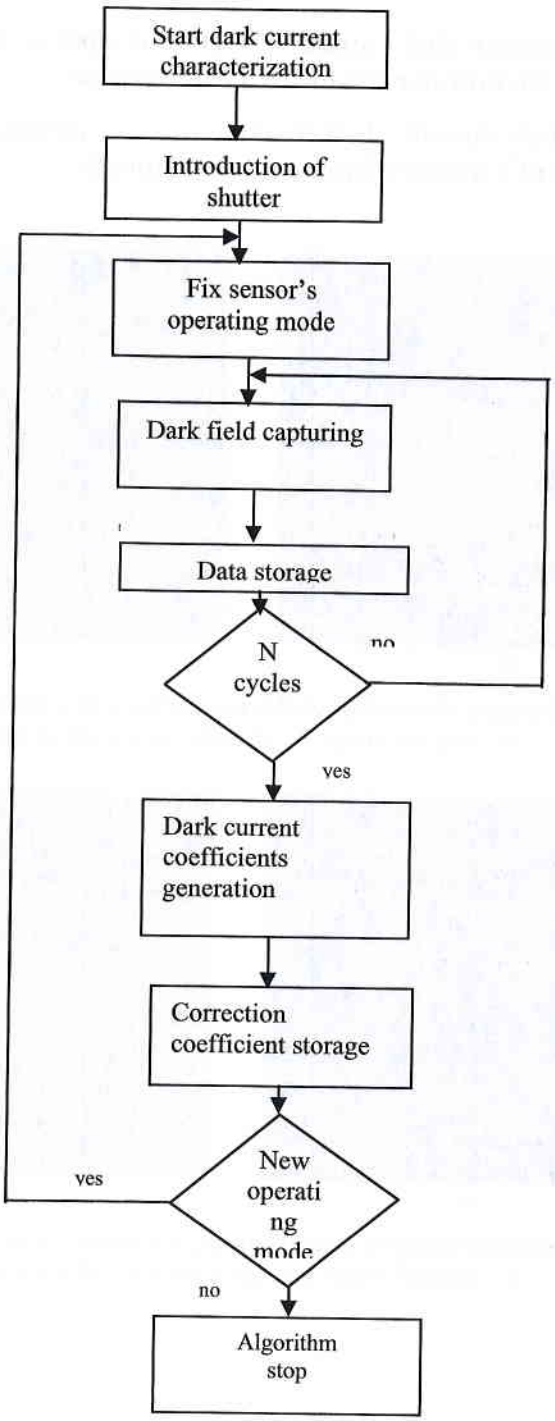

Fig. 4 Dark current characterization flow chart

2. The foreseen dark current correction in operation mode results in improvement of the instrument's metric characteristics.

3. The dark current characterization is an inseparable part of the spectral instrument's overall characterization process.

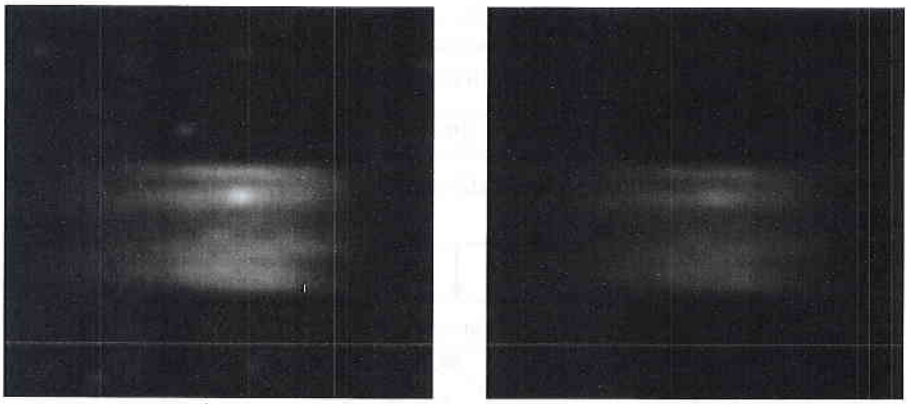

a/ b/

Fig. 5 Laboratory obtained spectral images (fragments), spectral band 550nm, a – original image, б – dark current corrected image.

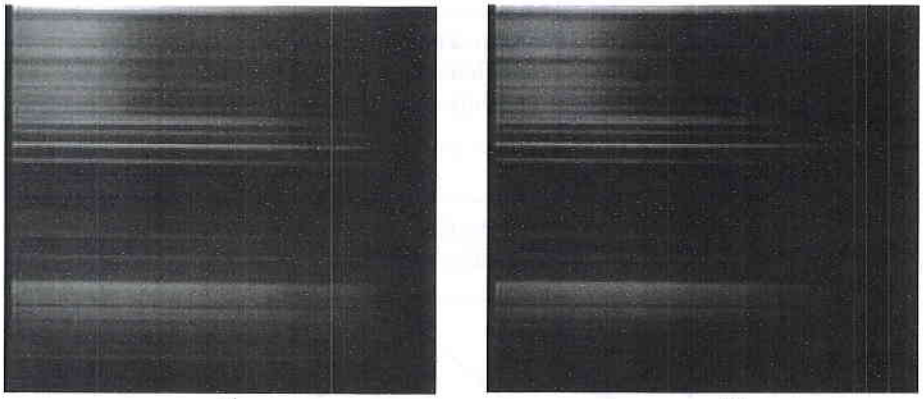

a/ b/

Fig. 6 Spectral images of natural objects, in spectral region 450 – 650nm, a – original image, б – dark current corrected image.

References

1. Kramer, H. J. Observation of the Earth and Its Environment. Springer, Berlin. 1996.
2. Mardirossian G. Aerospace Techniques in Ecology and the Study of the Environment. Marin Drinov Acad. Publ. House. Sofia, 2003.
3. W. Posselt et al. PRISM on-board characterization. SPIE, Vol.2957, 1997. pp.278-286.
4. Baudin G. et all., Medium Resolution Imaging Spectrometer (MERIS): Calibration Sequence. IAF Conference Proceedings, 1996.
5. Atanassov. V., G. Jelev, V. Ivanov. Characterization of Imaging Spectrometer Module. Proceed. of the Conf. G. Benkovski VNVVU, April, 2003..(in print).
6. Gardner D. CCDs Make the Most of Every Photon. Photonics Spectra vol. 36, June 2002.
7. Des Jardin W. Does Your CCD Camera Need Cooling. Photonics Spectra vol. 36, August 2002.
8. Atanassov. V et all. CCD sensors applicable in tracking and imaging spectrometers: Study and correction of their spectral characteristics. Compt. Rend. Acad. Bulg. Sci., T.48, №9-10, 1995. pp. 43-46.

АЛГОРИТЪМ ЗА ХАРАКТЕРИЗАЦИЯ НА ТЪМНИННИЯ ТОК НА ВИДЕОСПЕКТРОМЕТРИЧЕН МОДУЛ

Валентин Атанасов, Георги Желев

Резюме

В работата са представени част от резултатите, получени през времето на провеждане на лабораторни изследвания и тестове на модел на видеоспектрометър за дистанционни изследвания. Това са преди всичко резултати свързани с характеризационния процес при изграждане на прибора и по специално отнасящи се до характеризацията на тъмнинния ток. Описани са основните характеризационни процедури, предложен е алгоритъм за характеризация на тъмниния ток и са показани получените резултати.

Bulgarian Academy of Sciences. Space Research Institute.
Aerospace Research in Bulgaria. 19, 2005, Sofia

MODERN CCD SENSORS APPLIED IN IMAGING SPECTROMETERS

Valentin Atanassov, Georgi Jelev

Space Research Institute, Bulgarian Academy of Sciences

Abstract

In the paper, the state-of-the–art tendencies for design and construction of CCD types of sensors and their usage in spectroscopy applications is considered. The main performance characteristics of such devices when operating in imaging spectrometers on-board aircraft or satellites are highlighted and the requirements regarding their operating conditions are discussed. The experimental results obtained in the process of laboratory testing are shown and the basic CCD types are described.

1. Introduction

CCD (charge coupled device) sensors are widely applied in some scientific areas, such as spectroscopy, astronomy, etc. As a rule, these applications' operation modes involve device performance under low light illumination and limited integration time depending on the craft trajectory temporary characteristic [1, 2]. This fact imposes severe requirements towards their basic characteristics. The most important characteristics of CCD detectors when operated in imaging spectrometers are response, resolution, readout noise, dynamic range.

As a rule, in spectroscopy applications, CCD detectors are combined with a proper optical system to create a spectral image. A CCD can simultaneously collect spectrally dispersed light over a wide range at high speed. The two-dimensional CCDs used in such systems enable simultaneous measurement and analysis at multiple spectra from several spatial sources.

2. Basic CCD characteristics

Spectral response. The spectral response of CCD sensors is determined by the quantum efficiency. It is wavelength-dependent, because the absorption coefficient of silicon is wavelength-dependent. The absorption coefficient is approximately zero at wavelength shorter than 400nm and wavelength longer than 1100nm. The maximum of the quantum efficiency depends on geometrical and technological parameters and usage materials.

Dark current. The term "dark current" comes from the fact that the current is generated equally well in complete darkness. Depending on where in the silicon unwanted electrons are generated, some of the charges will collect in the CCD wells and, jointly with signal-generated electrons, will form output signal.

Dynamic range. Another important characteristic of the CCD, when operating in low–light conditions is its dynamic range. It may be defined as the ratio of the largest measurable useful signal to the smallest detectable signal. The smallest detectable signal is limited by the readout noise. The largest signal depends on full-well capacity.

3. Type of CCD sensors

Most modern scientific spectroscopy applications use two-dimensional full-frame- or frame-transfer CCD detectors, which are photo-sensitive across their full active surface area. A variety of devices are available, including front-illuminated devices, back-illuminated devices, virtual phase technologies, etc.

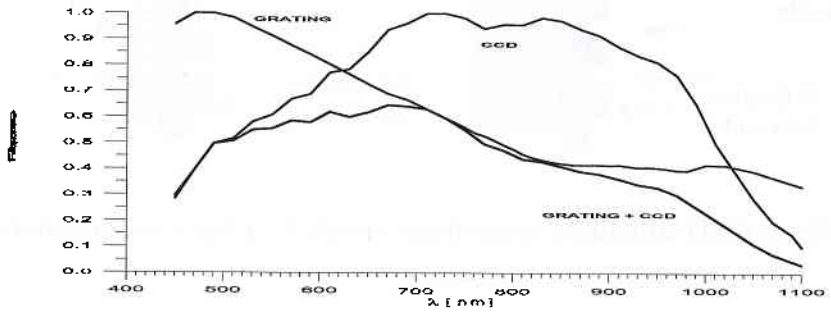

Fig. 1 Spectral response characteristic of CCD 221 (Fairchald)

Conventional CCDs are less sensitive (Fig. 1) compared to recent devices, because part of their surface area is coated with non-transparent electrodes [3].

Another type of front-illuminated CCDs are large-format, full-frame detectors, These devices are photosensitive across their full active surface area, because the gates, placed over the sensitive area, are typically composed of semi-transparent polysilicon (Fig. 2 – left). These sensors accommodate long exposure times. They offer the lowest dark current of all available sensor technologies and produce the best signal-to-noise ratios in low-light condition. Their light sensitivity, high charge capacity and low dark current also deliver a very large dynamic range. Unfortunately, polysilicon gates absorb or reflect incident light at wavelengths below 500 nm and the trade-off for large sensing areas has reduced sensitivity at shorter wavelengths (Fig. 3 – KAF1400) [4].

A type of CCD that offers a higher UV (ultra-violet) sensitivity is the so-called front-illuminated UV CCD, in which the detector is coated with phosphor, or the sensors with indium oxide gates, a material which is more transparent than polysilicon at short wavelengths (Fig. 3 – KAF1401E).

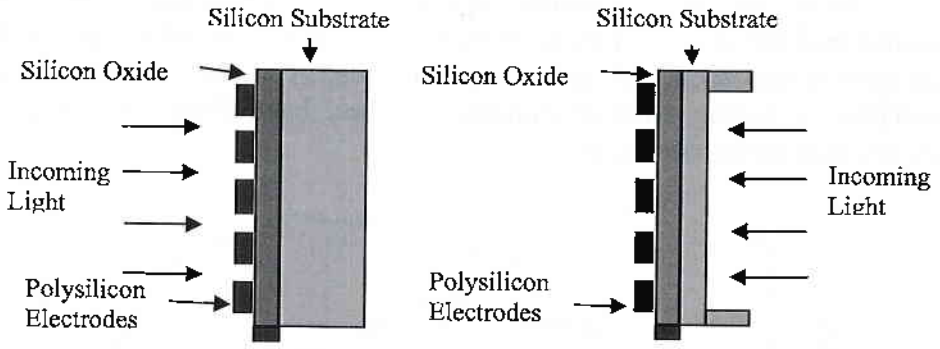

Fig. 2 CCD structures: front-illuminated (left), back-illuminated (right).

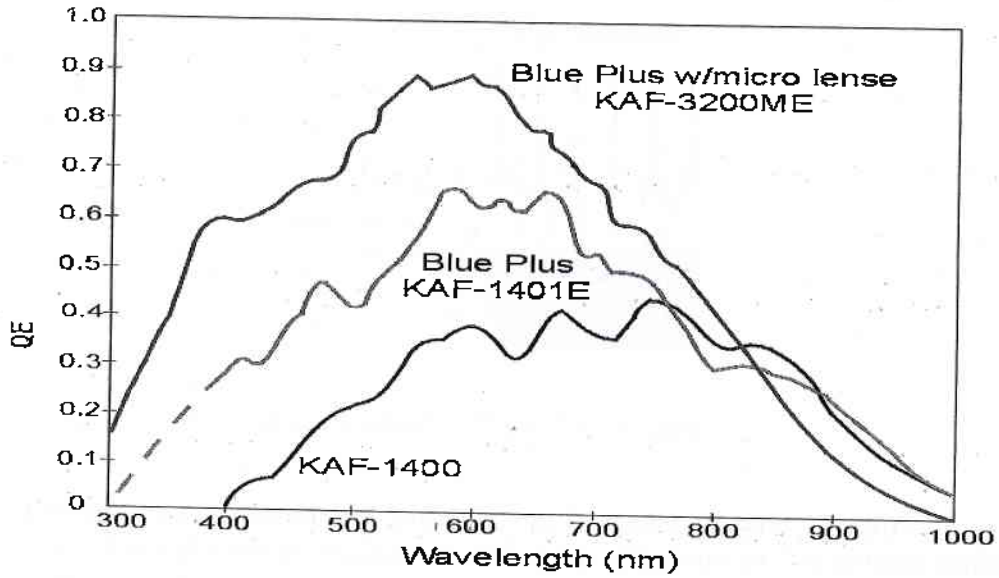

Fig. 3 Spectral response characteristics of KAFxxxx (Kodak) CCDs [4].

Another type of CCDs, using microlens array to direct light to photosensitive area, have improved efficiency over the whole spectral range (Fig. 4). This approach does not sacrifice other performance parameters. [5].

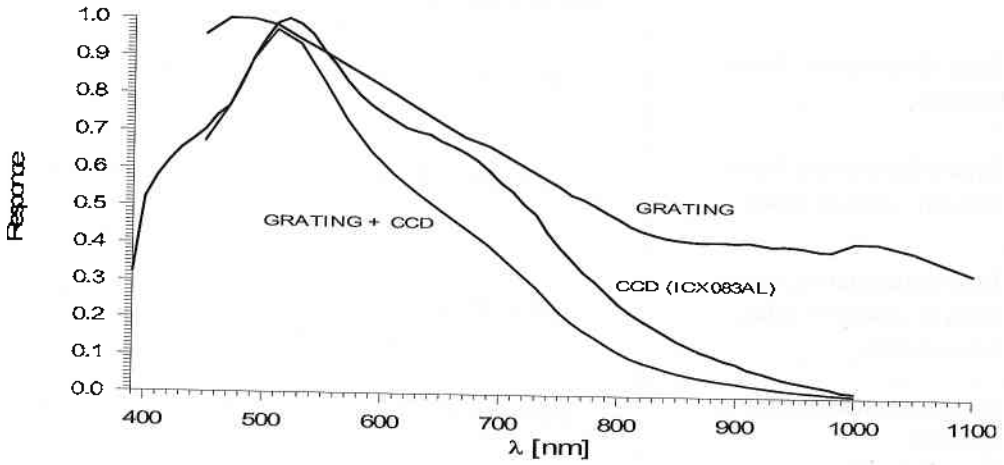

Fig. 4 Spectral response characteristic of ICX083AL (Sony) CCD

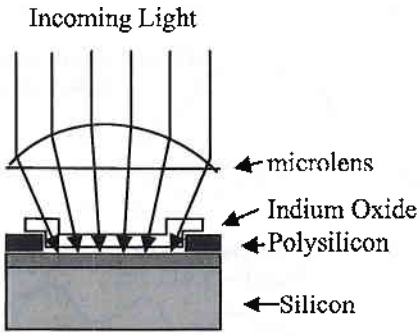

Fig. 5 CCD KAF3200ME structure

Another type of CCDs (Fig. 5), using a combination of the two above-mentioned technologies (the use of indium oxide electrodes and microlenses) have dramatically improved efficiency over the whole spectral range (Fig. 3 – KAF3200ME). These combined changes raised the peak quantum efficiency to 85 percent, a level previously possible only to back-illuminated sensors

Table 1.

Sensors' Type	**Quantum Effisiency 400 nm max 800 nm**	**Dark Current**	**Price**
front-illuminated, frame transfer	0% 45% 35%	*	*
front-illuminated, frame transfer, indium oxide	30% 65% 30%	*	**
front-illuminated, frame transfer, indium oxide, microlenses	60% 85% 45%	*	**
back-illuminated, frame transfer	65% 90% 75%	***	***

Legend: * - low, ** - midle, * - high**

They also improved quantum efficiency for blue and NIR (near-infra-red) regions.Back-illuminated CCDs, in which the substrate is thinned (Fig. 2 – right), feature enhanced response in the UV and the NIR regions (Table 1). Back-illuminated CCDs are much more expensive than their front-illuminated counterparts because they are difficult to make. These devices often require liquid nitrogen cooling to reduce noise. They have large pixel sizes, which limits resolution.

An additional comparative review of CCD types and their most important characteristics is shown in Table 1.

4. Conclusions

New sensor technologies offer many types of CCDs appropriate to low-light applications, including imaging spectrometers on-board aircraft or satellites. There are two-dimensional, large-format, frame transfer, front-illuminated or back-illuminated CCD sensors.

The choice of the CCD sensor is related to the application's requirements. In general, the choice should be made based on the spectral range, resolution, the expected optical signal levels, and the type of the constructed imaging spectrometer, such as ground-based, airborne or space-borne system. These requirements determine the chip type, total active area, number of pixels, pixel size, etc.

References:

1. Kramer, H. J. Observation of the Earth and Its Environment. Springer, Berlin. 1996.
2. Mardirossian G. Aerospace Techniques in Ecology and the Study of the Environment. *Marin Drinov* Acad. Publ. House. Sofia, 2003.
3. Atanassov. V., A. Krumov, V. Vasilev, N. Vasilev. Prototype of a Vis-NIR Imaging Spectrometer. 1998 ASPRS-RTI Annual Conference, Tampa, Florida, March 30 - April 4, 1998, Conference Proceedings, pp.1402-1407.
4. Des JardIn W. Does Your CCD Camera Need Cooling. Photonics Spectra vol. 36, August 2002.
5. Atanassov. V B., B. Peev, N. N. Vassilev, V.K.Vassilev. Functional Mode Features of CCD Sensor Operating in Imaging Spectrometer. The Eighth National Scientific and Applied Science Conference "Electronics'99", Proceedings of the Conference, book 4, September, 1999, pp. 7-12.

СЪВРЕМЕННИ CCD ПРИБОРИ, ПРИЛОЖИМИ ВЪВ ВИДИОМЕТРИЧНИ СИСТЕМИ

Валентин Атанасов, Георги Желев

Резюме

В работата са разгледани съвременните тенденции в развитието и изграждането на CCD прибори от гледна точка на приложимостта им във видеоспектрометрични системи. Посочени са специфичните условия на функциониране на сензорите и произтичащите от тях изисквания към по-важните им характеристики и параметри. Показани са основните типове прибори и е направена сравнителна оценка на техните характеристики. Приведени са експериментално получени резултати от изследвания на различни типове CCD сензори.

Bulgarian Academy of Sciences. Space Research Institute.
Aerospace Research in Bulgaria. 19, 2005, Sofia

MONITORING OF GREEN AREAS IN THE CENTRAL PART OF PLOVDIV CITY USING HIGH RESOLUTION SATELLITE DATA

Rumen Nedkov, Eugenia Roumenina, Georgi Jelev

Space Research Institute, Bulgarian Academy of Sciences

Abstract

Information updating for the biggest municipality's green areas' size and position is a problem related with two main characteristics of the municipality's ecosystem status. The green area and plantation system is an important space structure and functional part of the inside and outside of Plovdiv city's residential territory. It serves as a basis in the decision-making process on environmental improvement, recreation, and their connection with city architecture. The normalization of the green area system, which performs various functions, is of basic importance for all residential areas in Plovdiv city, which experience aggravated microclimatic conditions. The paper provides brief description of the methodology and the results of a scientific study of the central part of Plovdiv city.

The study was carried out based on aerospace, ground-based, and GPS data.

Key words: *satellite images, green areas, GIS, GPS.*

Introduction

A scientific and application research of the green areas status on the territory of the Plovdiv municipality was carried out, using aerospace, ground-based, and GPS data from various time periods.

The objects of the present paper are the green areas situated in the central region of the Plovdiv municipality.

The main objective is to update the area, position and dynamics of the green areas in the studied region using aerophoto and satellite images. For the purposes of change detection analysis, a 21-year interval is used, providing to best reveal the developmental tendency in the studied region.

Major tasks:

1. To create a GIS database comprising information on green area dynamics;
2. To monitor green areas using aerophoto and satellite images with very high spatial resolution alongside with the previously created GIS;
3. To create maps, reflecting the contemporary structure of the green areas in the central region;
4. To analyze the spatial dynamics of the same region's green area for the year 2003 compared to the year 1982.

The performed scientific study is underlined by modern aerospace, GPS and GIS technologies. Their use enables to obtain unbiased and accurate results, providing for immediate practical application. (The study was assigned and funded by the Plovdiv municipality).

Input Data

To create the GIS database, both remote-sensing and ground-based information was used. Remote-sensing information consisted of panchromatic and multispectral aerophoto and satellite images; ground-based information included very-high-scale topomaps, field-check data (terrain data) and GPS measurements. (aerophoto 1982, very-high-scale topomaps, Landsat 1992, QuickBird 2003, GPS data).

The methodology used to create the geographic database included several work stages: radiometric and geometrical corrections of the aerophoto and satellite images; remote-sensing and ground-based data rectification; thematic computer-based visual image recognition; creation of green area maps for the years 1982 and 2003; assessment of the green areas' spatial dynamics.

For the geometric correction model, 28 GPS identical ground control points (GCPs) and 51 triangulation points (TP) were used, which were undoubtedly recognized on an aerophoto, satellite images, topomaps of scale 1:5,000 and Digital Elevation Model (DEM). All GCPs coordinates and TPs were defined in the Baltic altitude coordination system, 1970. All GCPs and TPs were defined and located in the green areas or in their close vicinity. The GCPs and TPs were placed normally to the territory of the studied region.

Geometric orthorectification and georeferencing of input data was performed, followed by thematic recognition and interpretation.

The data were arranged and described into two levels according to their territorial location and economical importance: first level - terrains located in residential or industrial areas and second level - terrains occupied with parks and forest; green areas (shrubbery, grass areas in sport

equipments); green areas near transport equipments; other kind of land cover.

Central Region

The total area of the central region amounts to 8,320.14 dca, whereas almost 99 % of it is occupied by residential districts and only 105.1 dca are occupied by industrial terrains. The green areas during 2003 constituted 27 % of the total region area (Fig.), while in 1982, this percentage amounted to 19 %. The terrains covered with parks and forests remained almost unchanged, but green areas increased by 66 %, due to the new alleys and gardens located in the central part of the city, as well as the transient free areas from the Maritsa river.

Summary and conclusion

The results from the study feature very high spatial and temporal resolution. They were obtained based on modern aerospace, GIS and GPS technologies. The RMS of the TPs is 0.45 m and the RMS of the GCPs is 0.65m. The basic RMS is 1.1m.

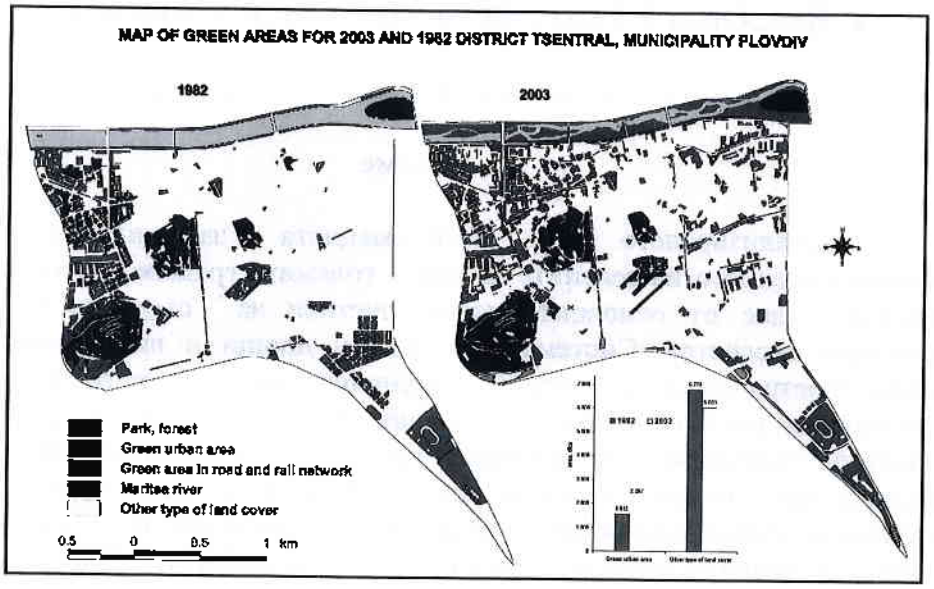

Fig.1 Thematics maps of green areas for 2003 and 1982 – Plovdiv.

A database was created, which contains information for the green areas of the Plovdiv Municipality (thematic maps of the various regions with very high scale of 1:5,000).

The dynamics of the green areas from 1982 to 2003 was assessed. The accuracy of the quantitative assessment is 4.5 %. The tendency revealed by the quantitative assessment shows an increase in the dimensions of the green areas not only in the central part but also in the inside and outside of the central part's residential territory.

References:

1. N e d k o v, R. Using GPS/GIS technologies in land reform (forest) in Bulgaria, Third International Conference on Geospatial Information in Agriculture and Forestry, Denver, Colorado, 5-7 November 2001.
2. Contracts № 01, 02/June 2003 – Municipality of Plovdiv, SRI BAS.
3. Contract № BG/47376451/23025 – Sovinformsputnic SRI BAS.

МОНИТОРИНГ НА ЗЕЛЕНИТЕ ПЛОЩИ НА ЦЕНТРАЛНАТА ЧАСТ НА ГРАД ПЛОВДИВ С ПОМОЩТА НА СПЪТНИКОВИ ДАННИ С ВИСОКА РАЗДЕЛИТЕЛНА СПОСОБНОСТ

Румен Недков, Евгения Руменина, Георги Желев

Резюме

Актуализирането на информацията за площта и местоположението на зелените площи в големите градове е проблем, свързан с две от основните характеристики за състоянието на градската екосистема.Системата от зелени площи и насаждения е важна пространствено-структурна и функционална част от селищната и извънселищната територия на Пловдив. Чрез нея се решават редица задачи за подобряване на околната среда, отдиха на населението, и връзката им с околната среда и естетиката на града. Нормирането на система от зелени площи, която изпълнява разнообразни функции е от голямо значение за всички селища и особено за големите градове като Пловдив, с утежнени микроклиматични условия на жилищната си среда. В работата накратко са изложени методиката и резултатите на проведеното от авторите изследване на територията на район централен от гр.Пловдив. Изследването е извършено на базата на аерокосмически, наземни и GPS данни.

Bulgarian Academy of Sciences. Space Research Institute.
Aerospace Research in Bulgaria. 19, 2005, Sofia

MEASUREMENT EQUIPMENT FOR QUASI-STATIC AND ALTERNATING LOW-FREQUENCY ELECTRIC FIELDS IN EARTH-SURROUNDING PLASMA

Boytcho Boytchev, Dimitar Teodossiev

Space Research Institute, Bulgarian Academy of Sciences

Abstract

The paper describes a method, sensors, and measurement equipment for quasi-static (DC) and alternating (AC) electric fields in the ULF/VLF frequency range in earth-surrounding plasma on-board satellites. The major requirements with respect to the equipment and electric fields' registration methods when using dedicated satellite scientific complexes are formulated. Moreover, the paper describes the major parameters of satellite on-board low-frequency electromagnetic effects measurement equipment, as well some original authors' developments intended for the a.m. purposes. The peculiarities of sensors' solutions, their interface with the measurement complex, the specific requirements for the latter resulting from the resolved scientific tasks, and the satellite's characteristics are also described.

1. Tasks solved

The designed equipment is intended to study the wave processes taking place in earth-surrounding plasma, the mechanisms of mass and energy transfer in the magnetosphere-ionosphere-atmosphere system and the influence of solar wind parameters; the processes of particles' acceleration and the mechanisms of generation, propagation and interaction of various types of electromagnetic waves and waves generated by geodynamic or anthropogenic activity [1,2,3].

It measures electric field components from 0 to 30 kHz. This frequency range is divided into several subranges of various maximal frequencies. The processing block also includes a 10-channel spectrum analyzer intended for preliminary processing and reduction of the device's output information flow under the monitoring operation mode [4,5].

A main task in modern space experiments is to carry out correlated observations, intended to separate spatial and time relationships, providing to highlight the causal relation between the studied processes, and guaranteeing the devices' high-resolution in phase space, thus enabling the study of small-specific-scale processes [6,7].

2. Measurement method and sensors

The device operates after the Langmuir double-probe method. The method is used to measure the potential difference between two opposite spherical sensors. Each component can be measured either by an individual sensor couple or using some other component's sensor couple. Each of the device's sensors measures the potential at the measurement point. When measuring the potential difference between two sensors, the intensity of the electric current for the individual components of the DC and AC fields is determined [8,9,10].

The electric sensors used in the device are made of glass-carbon-coated spherical monoblock and fixing elements. The construction of the spherical sensor is shown in Fig. 1. The major sensor components are: a sensitive element – sphere with diameter of 80 mm covered by glass-carbon; symmetry-providing electrodes; protective electrode; preamplifier PA, assembled within the sphere; preamplifier screening box, and disconnector. The use of spherical sensitive elements is substantiated by the requirement for high symmetry level. The symmetry-providing electrodes are intended to ensure identical conditions for the electrodes with respect to the Sun. The protective electrode is intended to reduce the influence of the photoelectrons from the satellite structure components.

The sensors' potential is determined by the balance of their surface electric currents, which depend on the material and the characteristics of the sensors' operating surface. For this reason, we use spherical sensors with glass-carbon coating obtained after a unique Bulgarian method [11]. Within the spherical sensor, a preamplifier is mounted, intended to harmonize plasma impedance with the input impedance of the satellite measurement block. The preamplifier is two-stage, containing high-resistance voltage reproducer, made of operation amplifier featuring a PEC input, and an alternating-current amplifier, amplifying the smaller-amplitude alternating-current voltage fluctuations. Thus, the sensor has two information outputs, one for constant, and one for alternating field. The diagram also contains high-voltage protection, switch-over and calibration circuits etc.

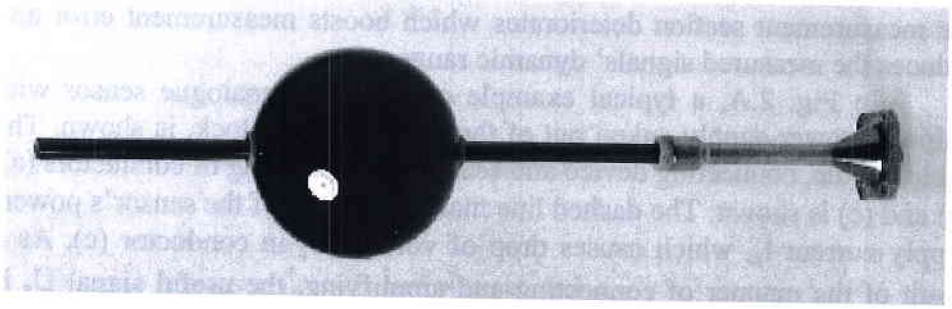

Fig.. 1

In electric-field-measurement experiments, the probes must be positioned sufficiently far off the satellite, so as to escape the disturbed area around it. For the purpose, it is sufficient that the distance d from the sensors to the closest convex part of the satellite be no less than 5 times the satellite's radius. Here, some of the most successful experiments measuring satellite electric fields may be given, where the distance between the sensors is, accordingly: GEOS – 42 m, S3-3 – 36 m, ISEE-1,2 – 74 m, GEOTAIL – 160 m, WIND –50 m, POLAR – 100 and 130 m, CLUSTER – 1,2,3,4 – 100 m.

To make potential distribution around the spherical sensors symmetrical, several solutions are applied depending on the satellite's type – whether it is a microsatellite or a large object. The relatively large satellites are fed shifting voltage. This method was used on the satellites S3-3, ISEE, GEOTAIL, INTERBALL, CLUSTER etc. In microsatellites, the preamplifier's output is connected to the protective and symmetry-ensuring electrode, which makes it possible to maintain one and the same potential over the whole sensor.

3. Connection between sensors and equipment

The electric fields and other quantities are measured by sensors with built-in amplifiers, transducers etc. Their power-supply is usually provided by the equipment to which they are connected. The equipment's power supply and the sensor's power supply are common and there is a galvanic link between them. Some of the circuits connecting the sensor with the measurement block participate in both the contour of the output signal and the sensor's power supply. As a result, these circuits interact and the accuracy of the analogue information's transfer from the sensor's output to

the measurement section deteriorates which boosts measurement error and reduces the measured signals' dynamic range.

In Fig. 2.A, a typical example of an active analogue sensor with unipolar power-supply, taken out of the measurement block, is shown. The cable bundle, connecting device and sensor and consisting of conductors (a), (b) and (c) is shown. The dashed line marks the route of the sensor's power-supply current I_z, which causes drop of voltage U_z in conductor (c). As a result of the manner of connecting and amplifying, the useful signal U_s is mixed with the voltage drop U_z in (c), and thus gets amplified by A.

To eliminate the problem, the following solution is suggested. Obviously, the adding up of U_s и U_z during the signal's transfer from the sensor to the device should be eliminated. The suggested solution is represented in Fig. 2.B; it is accomplished through additional link (d) and the signal's amplifying by differential amplifier DA, which carries away and amplifies the signal from sensor U_s, eliminating its mixing up with U_z.

This technical solution was applied to carry away the signals from the electric and magnetic sensors of the ULF/VLF complex of the COMPAS Project. It is reflected in the equipment's electric filed measurement block to be considered further on. The application of this solution resulted in material increase of the measurement accuracy of the sensor-fed signals.

4. Equipment parameters for studying ionospheric and magnetospheric fields

Measurement of electric fields are important as for the decision of questions in the ionosphere and magnetosphere plasma, and the processes connected from anthropogenous activity. Microsatellites, and heavy satellites are used to carry out complex measurements in the ionosphere and magnetosphere plasma. The parameters of the equipment for electric fields measurements on satellites of project CLUSTER and the planned project the RESONANCE are presented in Table 1. The results can be used for comparison of similar equipment for microsatellites (as example the COMPAS microsatellite).

5. Equipment parameters for studying ionospheric seismoelectromagnetic effects

***Frequency range*:** Electromagnetic emissions within the range from fractions of the hertz to dozens of kilohertz have been observed. The detailed analysis of experimental data evidences that persistent seismoelectromagnetic signals are observed at frequencies lower than 800

Hz, but alongside with them, signals with frequencies of 10 kHz and 15 kHz have also been recorded.

Table 1.

Measured quantity	Frequency range	Dynamic range	Satellite
DC Electric Field (2 components) AC Electric Field (2 components)	0 – 10 Hz 0 – 200 Hz 0 – 5000 Hz 0 – 10000 Hz 10 – 5000 Hz	700 mV/m – 0.1 mV/m 700 mV/m – 0.1 mV/m 700 mV/m – 0.1 mV/m 700 mV/m – 0.1 mV/m 10 mV/m ≈ 1 μV/m	CLUSTER
DC Electric Field (2 components) AC Electric Field (2 components)	0 – 30 Hz 0.01 Hz- 30 kHz	100 dB 80 dB	REZONANS

Amplitude: Judging from reference data based on the analysis of large arrays of satellite experimental results, seismic-activity-related signals are those for which the signal-to-noise ratio is > 3. The studies of the signal amplitude's dependence on Δt, the time offset between the earthquake's occurrence and the time of measurement, reveal that the seismoelectromagnetic effects are manifested most strongly at frequencies < 1 kHz in the vicinity of the earthquake's epicentre.

Spectral density: It varies with frequency, being higher with lower frequencies. For emissions within the frequency range from 0.1 kHz to 0.5 kHz, the absolute value of the magnetic component's spectral density is > 0.3 – 3 $pT/Hz^{1/2}$.

Duration: The earthquake electromagnetic precursors can be recorded within a couple of days prior to the earthquake's occurrence. The duration of observation of seismoelectromagnetic emissions on-board satellites depends on the satellite's orbital characteristics (height and inclination), i.e., the height at which it crosses a force tube related with the earthquake's epicenter.

Experiments have shown that it takes from a couple of seconds to a couple of minutes.

The separation of ionospheric seismoelectromagnetic effects from the background values of such emissions at satellite orbital height is a key task, since the field's generation mechanisms and the propagation

conditions for various types of waves are strongly influenced by solar activity, geomagnetic circumstances, season, local weather etc. Moreover, in earth-surrounding plasma, various physical processes take place, which generate signals similar to seismoelectromagnetic effects.

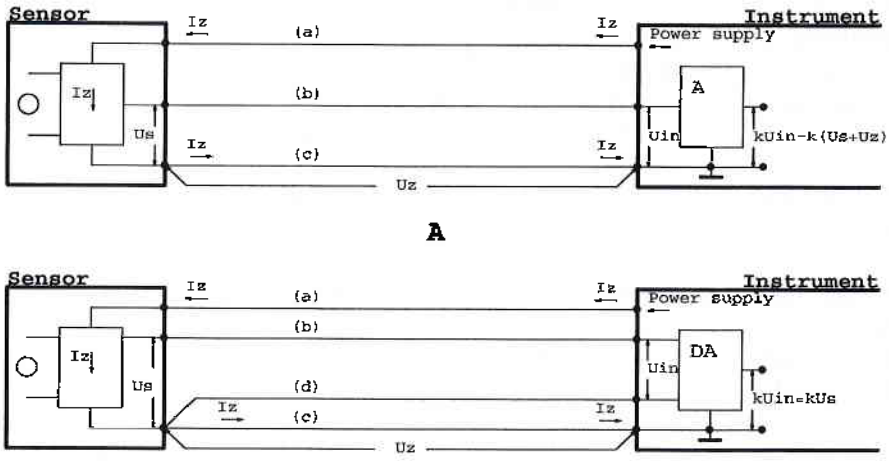

Fig. 2

6. Peculiarities of on-board equipment in recording geomagnetic-activity-related electromagnetic fields in earth-surrounding plasma

To solve the scientific tasks related with studying electromagnetic and plasma earthquake precursors, three basic on-board-satellite measurement modes should be used [12,13]:

Monitoring mode or minimal telemetry mode. Under this mode, key physical parameters are measured continuously on a 24-hour basis within selected channels and with a small inquiry frequency (of about one inquiry per second). This mode presumes continuous monitoring. In accordance with the selected mode the equipment measures the quasi-static field's components, while the alternating field' measurements include only measurement of local frequencies by a spectral analyzer to reduce data flow.

Local monitoring mode. Under this mode, the full set of the physical parameters provided by the scientific equipment complex is monitored, during all satellite orbits passing over some of the Earth's seismoactive regions. The EMC operates in its most informative mode, measuring the actual signal "wave" forms within a wide frequency range, but only for the time while passing over the region.

Physical experiment mode. This mode is used when targeted experiments are carried out, implying the use of other space or ground-based instrumentation. Under this mode, the satellite's full scientific complex operates with maximal telemetry and jointly with other on-board geophysical and radio-physical provision instrumentation. The operating mode resembles the description provided in item *Physical experiment mode.*

Operating conditions restrictions on-board small satellites. For the purpose of studying various environmental parameters and processes taking place in Earth-surrounding space and on Earth, recently, small satellites have been widely used.

The small size and mass of such space apparata call for reduction of some of their office systems, operation time, power resource, as well as for material telemetry restrictions etc. However, this results in significant reduction of the price per on-board load (equipment). The equipment to be mounted on such objects should comply with their specific features.

7. Structural diagram of the measurement complex

The structural diagram (Fig. 3) of the measurement complex provides for changing the number of the measured field components and their frequency range, making preliminary processing of collected data, such as spectral analysis of some components, switching over of components, selection and changing of operation regimes by a command from the Earth [14]. By varying the operation regime, the complex's options as well as the amount of output data vary greatly, too. Below, the major components and the operation of the ULF/VLF-complex are described. On the presented structural diagram, the analogue signals to be processed and converted in the digital section are shown. These signals are output at control coupling T.

The signals M1-M4 controlling the complex's operation regimes as well as the signals Ft, R, A, Ct, Fms, D0-D7 providing for the protocol and data exchange with on-board telemetry are also shown. They are duplicated and output at control couplings IO1 and IO2.

The ULF/VLF-complex is intended to measure one of two optional components of the AC electric field and one component of the alternating magnetic field in the following frequency ranges:

- from 1Hz to 30Hz - denominated on the flow-chart as MVF1 and EVF1;
- from 30Hz to 1000Hz - denominated on the flow-chart as MVF2 and EVF2;
- from 30Hz to 8000Hz - denominated on the flow-chart as MVF3 and EVF3;

- parallel spectral analysis of one electric and one magnetic field component with ten local frequencies (7.5, 14, 30, 70, 140, 560, 1300, 4500, 8500, and 15000Hz) - signals from ED1 to ED10 and from MD1 to MD10.

Apart from these, the ULF/VLF-complex measures: - two components of the quasi-DC electric field within the range 0-2Hz - signals PP1-2 and PP2-3; - the temperature in the electronic block and the electric and magnetic sensors coupled with it - signals BT1-BT5.

The complex consists of: - electric sensors ED1, ED2, and ED3 with preamplifiers for measurement of one of two optional electric components; - a block of magnetic sensors, BMD, consisting of two magnetic sensors in different frequency regions with preamplifiers for measurement of one magnetic component;- An electronic block housed within a single case, and consisting of a block for study of electric fields, EPS, a block for study of magnetic fields, MPS, a data acquisition block, BSD, consisting of a microprocessor system for collection of data from 36 analogous channels, generation of calibration signals, complex control, processing of obtained data, and connection with the object's telemetry, a block for galvanic disconnectio and duplication of signals for data exchange with telemetry - BGRD, and a power-supply block for galvanic disconnection from the on-board power-supply, VIZ.

The analogue data obtained at the outputs of the above-named blocks is processed by a quick 12+1 data acquisition bit system of the LM12458 type, and a microprocessor system based on the processor 80C188XL. The system also includes a block for generation of calibration signals providing for autocalibration during flight.

8. Approbation of equipment and sensors under the conditions of real experiments

Electric sensors measuring electric fields on-board satellites, that have been developed at the SRI – BAS with our participation have operated successfully on eight satellites: IC Bulgaria 1300 (1981); IC-24 Activen (1989); Magion-2 (1989); IC-25 – APEX (1991); Magion -3 (1991); Magion -4 (1995); INTERBALL-2 (1996) and Magion -5 (1996).

Measurement equipment and sensors intended for the COMPAS microsatellite, featuring the a.m. parameters, have been developed and have passed technological tests. The equipment is intended to study ionospheric electromagnetic effects caused by geodynamic activity.

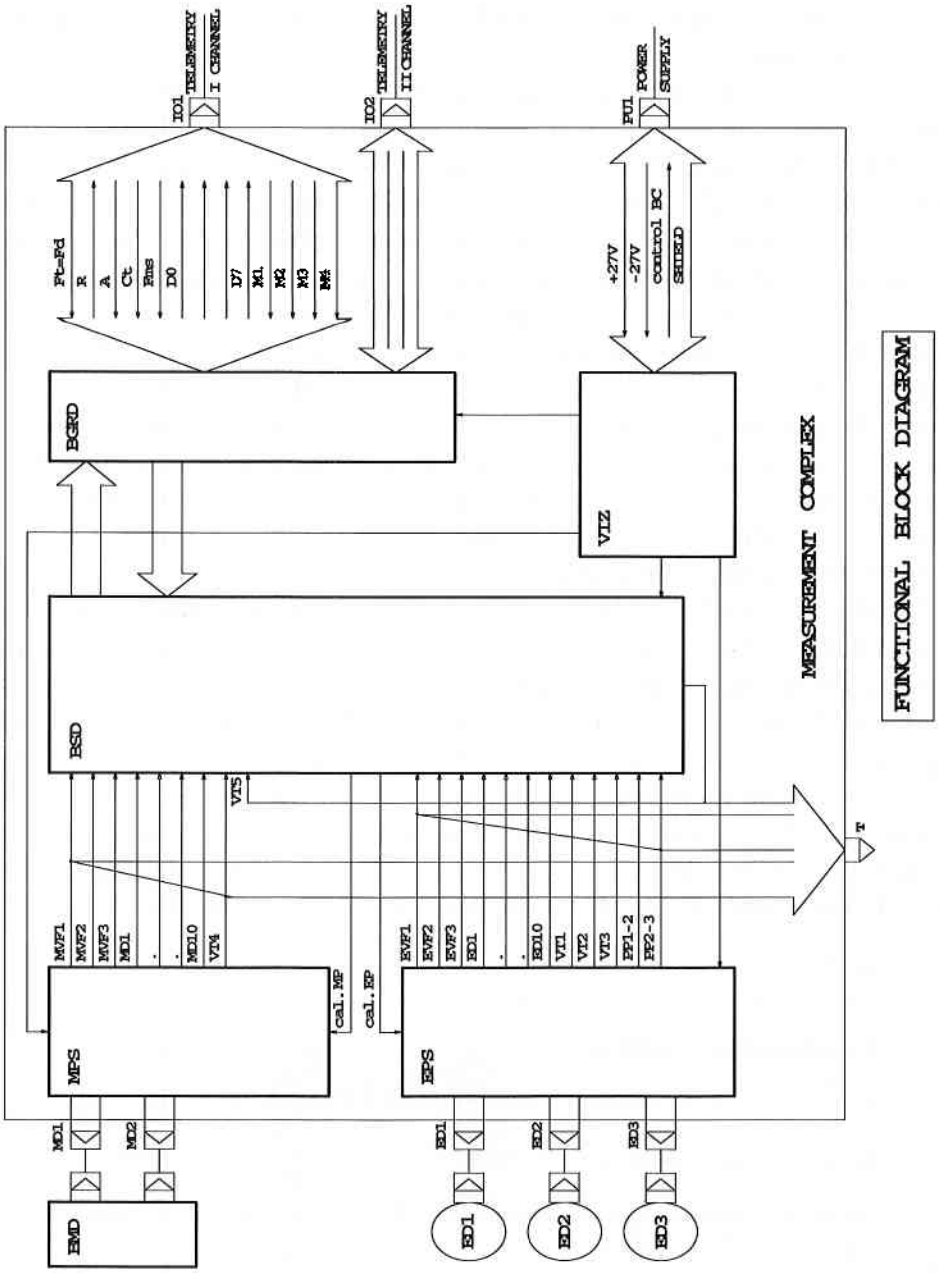
FUNCTIONAL BLOCK DIAGRAM
MEASUREMENT COMPLEX
IO1 TELEMETRY I CHANNEL
IO2 TELEMETRY II CHANNEL
PU1 POWER SUPPLY
Pt-Pd
R
A
Ct
Fms
D0
D7
M1
M2
M3
M4
+27V
-27V
control BC
SHIELD
BGKD
VIZ
BSD
VTS
T
MVF1
MVF2
MVF3
MD1
MD10
VT4
cal.MP
cal.EP
EVF1
EVF2
EVF3
ED1
ED10
VT1
VT2
VT3
PP1-2
PP2-3
MPS
EPS
MD1
MD2
ED1
ED2
ED3
EMD
ED1
ED2
ED3

Fig. 3

9. Measurements in the High-Latitude near-Earth Magnetotail Region

ULF measurements aboard Magion–4 were performed during UT 13:00 – 13:45 while the spacecraft crossed the high-latitude near-Earth magnetotail at distance 11 R_E in the pre-noon sector [15]. Data are presented in Fig. 4. Initially till 13:28 UT we observe ULF electric fluctuations which are purely electrostatic. Magion-4 position and plasma data (not shown here) suggest that during this period measurements take place on field lines connected with the lobes, though at higher latitudes than the Day 20.04.1997 case. A sharp increase of wave activity begins at UT 13:28, the spectrum of the waves changes to electromagnetic. Plasma instruments aboard Magion-4 register density enhancement. We interpret the changes in medium characteristics as spatial, due to s/c entering a magnetosphere boundary layer. As IMF Bz <0, the mantle is supposed to be well developed so we conclude that measurements after UT 13:28 take place in the plasma mantle. Unfortunately, magnetic field and plasma measurements on board the Interball-1 satellite, which could facilitate region identification, are absent for this period. While the electrostatic spectrum is below 1 Hz, the electromagnetic one is up to 5÷6 Hz and its intensity decreases for higher frequency. Note that the absence of electric field component at higher frequencies (above ω_{ci}) could be connected with the worse sensitivity of our ULF electric field measurements compared to the magnetic field one. The intensity of the E waves is structured, and the E field component is orientated in the meridian plane. The electromagnetic spectrum observed in the mantle belongs probably to electromagnetic ion cyclotron modes.

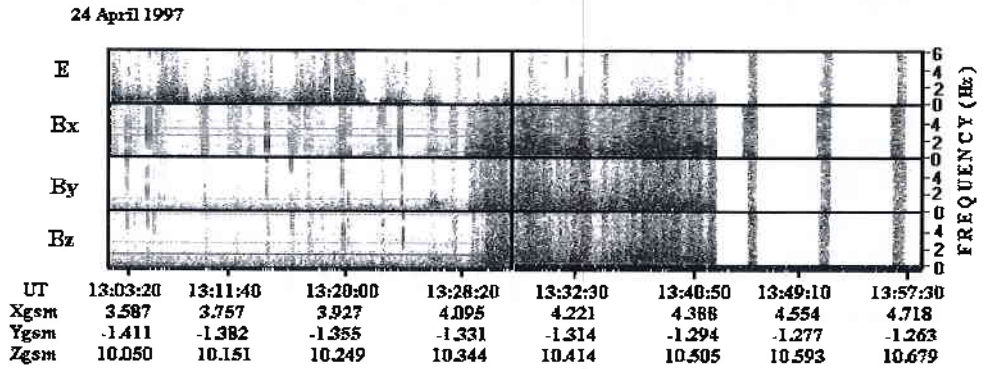

Fig. 4 Dynamic spectra of Magion-4 ULF electric and magnetic ield components on 24 April 1997 derived from waveform data. At ~ UT 13:28 the spectrum changes from electrostatic to electromagnetic.

References

1. Lakhina, G., B. Tsurutani, H. Kojima et al., *J. Gephys. Res.*, **105,** A12, 27791, 2000.
2. Tsurutani, B., E. Smith, R. Thorne et al., *Gephys. Res. Lett.*, **8,** 183, 1981.
3. Galeev, A., Y. Galperln, L. Zelenuy, *Cosmic Res.*, **34,** No 4, 339, 1996.
4. Boytchev, B., V. Chmyrev, G. Belyaev et al., Proceedings of Conference, "10th Anniversary of the Shipka Project", Sofia, Bulgaria, 67, 1999.
5. Boytchev, B., V. Boythev, Proceedings of the Conference, "30th Anniversary of Space Research in Bulgaria", Sofia, Bulgaria, 86, 2000.
6. Pedersen, A., P. Decreau, C. Escoubet et al., *Annalel Geophys.*, **19,** 1483, 2001.
7. Andre, M., R. Behlke, J. Wahlund et al., *Annalel Geophys.*, **19,** 1471, 2001
8. Pedersen, A., F. Mozer and G. Gustavson, AGU Gephys. Monograph **103,** 1-12, 1998.
9. Boehm, M. H., C. W. Carlson, J. McFadden et al., *Geophys. Rev. Lett.*, **11,** 511, 1984.
10. Teodosiev, D. T., I. Pecheniakov, J. Georgiev et al., *Bulgarian Patt.* No.36107, 1981.
11. Teodosiev, D. T., G. A. Stanev, G.K. Galev et al., *Cosmic Res.*, **18,** No 6, 614, 2000.
12. Chmyrev, V. M., N. V. Isaev, O. N. Serebriakova et al., *J. Atmous. Solar-Terr. Phys.*, **59,** 967, 1996.
13. Project COMPAS satelite, IZMIRAN, RAS, Troitsk, 1996.
14. Boytchev, B. V., PhD Thesis, Space Res. Institute BAS, Sofia, 2003.
15. Hristov, P. T., P. I. Nenovski, D. K. Teodosiev et al., *Space Sci. Rev*, **31,** , 2003.k

АПАРАТУРА ЗА ИЗМЕРВАНЕ НА КВАЗИПОСТОЯННИ И ПРОМЕНЛИВИ НИСКОЧЕСТОТНИ ЕЛЕКТРИЧНИ ПОЛЕТА В ОКОЛОЗЕМНАТА ПЛАЗМА

Бойчо Бойчев, Димитър Теодосиев

Резюме

В работата са представени метод, сензори и апаратура за измерване на квазипостоянни DC и променливи AC електрични полета в ULF/VLF честотните диапазони, в околоземната плазма, от борда на спътници. Апаратурата е разработена за целите на изследването на вълнови процеси, протичащи в околоземната плазма, механизмите на пренос на маса и енергия в системата магнитосфера-йоносфера-атмосфера и влиянието на параметрите на слънчевия вятър; процесите на ускоряване на частици и механизмите на генериране, разпространение и взаимодействия на различните видове електромагнитни вълни, както и такива предизвикани от геодинамична активност и антропогенна дейност.

Формулирани са основните изисквания към апаратурата и методите за регистриране на електрични полета с помощта на специализирани спътникови научни комплекси. Направено е разглеждане и обобщение на резултатите от характерните случаи на такива наблюдения. В работата са представени и основните параметри на апаратура за измервания на нискочестотни електромагнитни ефекти от борда на спътници, както и оригинални разработки на авторите за горепосочените цели.

Конкретно са разгледани особеностите на реализация на сензорите, свързването им към измервателния комплекс и специфичните изисквания към него, продиктувани от решаваните научни задачи, и характеристиките на спътника. Представената апаратура е резултат от натрупания опит на авторите от няколко спътникови експерименти, като предложените решения са илюстрирани с резултати от тях. В работата е направено обосновано предложение за прилагането на разработената апаратура в бъдещи проекти.

Bulgarian Academy of Sciences. Space Research Institute.
Aerospace Research in Bulgaria. 19, 2005, Sofia

METHOD AND SYSTEM FOR MEASUREMENT AND SELECTION OF MAGNETOSPHERIC AND LITHOSPHERIC SIGNALS OF THE EARTH'S SURFACE

Boytcho Boytchev

Space Research Institute, Bulgarian Academy of Sciences

Abstract

ULF signals are ubiquitous phenomena in the Earth's environment. These signals are of magnetospheric, ionospheric and lithospheric origin. Theoretical considerations concerning ground-based recording of ULF signals are made revealing the usefulness of electric field measurements. An instrument for electric field measurement is described and some preliminary data presented.

1. Introduction

There are several reasons for measuring electric and magnetic field variations on the ground. First, magnetosphere-ionosphere processes contribute to short-term variations of the Earth's magnetic field that are connected with external sources [1]. Second, we use electro-telluric measurements for geological purposes. Third, the Earth's electric potential variations are often treated as a possible precursor of earthquake events [8]. The frequency range of ULF electric and magnetic fields is less than 5 Hz. ULF electric and magnetic fields in the environment are of both natural and anthropogenic origin. The natural sources are solar activity, the magnetosphere and the ionosphere. The natural ULF fields, although weak, have the ability to penetrate through the atmosphere and the Earth's crust. Industrial fields are usually much stronger but they are confined to localized regions around technical systems (e.g., energy power cables, railway lines, transformer stations, etc.).

2. Theoretical Backgrounds

In the ULF range, there are also very long-period pulsations with periods of minutes to hours. Long-period (150-600 s) minute pulsations are observed near the geostationary orbit [3]. Junginger et al. [3] have suggested that these pulsations are solar-wind-driven surface waves that couple the field-line resonances near the geostationary orbit. It is left to future research to clarify whether cavity resonances or compressional oscillations are the modes observed at geostationary orbit. Yumoto [10] has reported Pi2 pulsations of dominant period ~135 s at high (L = 6.9) and low-latitude (L = 1.2) stations. He has concluded that Pi2 pulsations are global phenomena and interpreted them as magnetospheric cavity waves excited in the whole inner region bounded by the plasma sheet. Longer period pulsations (with periods T > 600 s) are usually connected with the oscillations in the ionosphere, produced by magnetospheric (sub)storms, or by influences produced in the lithosphere, or atmosphere (see Sorokin and Fedorovich, 1982). The latter are of electromagnetic nature, i.e., their electric field $\boldsymbol{E}$ is perpendicular to the propagation direction. These wave phenomena have typical periods of 600 – 6,000 s. They have been defined as gyrotropic waves (GW). These wave disturbances are sometimes transformed into usual magnetohydrodynamic (MHD) modes, otherwise wave disturbances of period T > 600 s are not transformed. The transformation conditions depend on the frequency and the ionospheric state. Inversely, MHD waves of very long period (above 100 seconds) and phase velocity of 10-1,000 km/s cannot penetrate into the ionosphere and the Earth's surface. It is thought that a MHD wave field of a very long period will possess a wavelength that is comparable to the scale size of the magnetosphere. Therefore, geometric effects are to be taken into account. If the latter are considered localized MHD waves of a very great period they could propagate to the ionosphere. In the ionosphere, these modes could partly be transformed into GW as examined by Sorokin and Fedorovich [5]. Thus, on the Earth's surface we could expect ULF disturbances of various origin – from the lithosphere (connected with the active seismic events) or from the magnetosphere.

In this study, we are examining the field properties of long-period disturbances produced on the Earth's surface. We are studying the electric and magnetic field distribution of the ULF wave disturbances in the system lithosphere-atmosphere-ionosphere. We will point out the amplitude differences connected with the sources of the ULF disturbances. We

introduce an electrostatic potential φ and a magnetic vector potential $\boldsymbol{A}$. According to the physical properties of the different regions, we are going to obtain quantitatively the effects on the electric and magnetic field distribution.

The ULF electro-telluric field is associated with the ULF magnetic field magnitude. The latter could be evaluated according to the relation [4, 6]

$$\boldsymbol{A} = \mu_0 \varepsilon_{crust} \partial \boldsymbol{\Pi} / \partial t + \mu_0 \sigma_{crust} \boldsymbol{\Pi}, \tag{1}$$

where $\boldsymbol{A}$ is the magnetic field potential and the Hertz vector $\boldsymbol{\Pi}_e$ ($\boldsymbol{\Pi} = -\varepsilon_{crust}^{-1} \boldsymbol{\Pi}_e$ is connected with the electric field potential φ by the relation $\varphi = \mathrm{div}\boldsymbol{\Pi}$; ε_{crust} and σ_{crust} are the crust dielectric permittivity and conductivity, respectively. In a medium of finite conductivity σ_{crust} ($\sigma_{crust} < \infty$) the equation that governs the Hertz vector is

$$\nabla^2 \boldsymbol{\Pi}_e - \mu_0 \varepsilon \partial \boldsymbol{\Pi}_e / \partial t - \mu_0 \sigma \partial \boldsymbol{\Pi}_e / \partial t = \boldsymbol{C} \exp(-\sigma_{crust} t / \varepsilon) \tag{2}$$

where $\boldsymbol{C}$ is a constant. This means that for times $t > t_0 = \varepsilon_{crust}/\sigma_{crust}$, the system will enter steady-state conditions. After t_0, $\boldsymbol{\Pi}_e$ will vary as the magnetic field vector potential $\boldsymbol{A}$. Because the vertical current $\boldsymbol{j}$ is assumed to be zero, the magnetic vector potential $\boldsymbol{A}$ has only horizontal components (A_x, A_y, 0). (The Hertz's vector $\boldsymbol{\Pi}_e$ has the same orientation as the magnetic vector potential $\boldsymbol{A}$). In eq. (2), the time derivative is proportional to $\gamma = -i\omega + \boldsymbol{k}^2/\mu_0\sigma_{crust}$, where ω is the ULF frequency and $\boldsymbol{k} = (k, 0)$ is the horizontal wave-vector. According to experimental evidence, ω varies from several mHz up to 1 Hz. The fields decay in the Earth with coefficient $\kappa = (k^2 + i\omega\mu_0\sigma_{crust})^{1/2} \cong k$. Under conditions of long-period pulsations ($\omega/2\pi < 0.02$ Hz), the magnetic field potential $\boldsymbol{A}$ (1) is controlled by the second term. Then, it follows that

$$\boldsymbol{A} \cong \mu_0 \sigma_{crust} \boldsymbol{\Pi}. \tag{3}$$

Attempting to compare the magnetic field ($\boldsymbol{B}$) and electric field potential (φ) magnitudes, we obtain the following relations:

$$B_{x,y} = \pm \kappa A_{y,x} \text{ and } \varphi = \kappa \Pi_x.$$

Hence $|B_{x,y}| \cong \mu_0 \sigma_{crust} |\varphi|$. (4)

For crust conductivity of 10^{-2} S/m, the magnetic field magnitude will be of the order of $4\pi \times 10^{-9}$ φ (in T) (conductivities of 10^{-2} S/m refer to soil conditions). If we use a value of 0.01 V for the observed ULF electric signals, we obtain a magnitude of the order of 1.10^{-10} T for the primary ULF magnetic field that penetrates into the soil. Such values correspond to geomagnetic pulsations magnetic field magnitude in the Pc3 range (with period T = 10–45 seconds). However, under rock conditions, the conductivity is of the order of 10^{-4} S/m. Thus, the primary ULF magnetic field magnitude requires greater electro-telluric field magnitudes. Therefore, under rock conditions, the observation of ULF pulsations is facilitated. In addition to ULF signals of magnetospheric origin, there are ULF electric signals from internal, lithospheric sources [8, 9]. According to eq. (4), the magnetic field magnitude would then be very low and its registration with a magnetometer is likely to be hampered. For this reason, the magnetic field potential $\boldsymbol{A}$ of the ULF signals of lithospheric origin has to be neglected. This makes preferable the ULF electro-telluric measurements for ULF signals of both the magnetospheric/ionospheric and lithospheric origin. The period of the lithospheric ULF signals varies from twenty minutes to several hours. Thus, ULF signals of magnetospheric origin have higher frequencies than those of lithospheric origin and hence they can be easily separated from each other. This peculiarity is used to design an integrated instrument for measuring ULF signals from internal and external sources.

3. Penetration of Signals of Lithospheric Origin

Upon solving the corresponding wave equation assuming homogeneous conductance, σ_{crust}, an illustration of the electric field amplitude distribution in the lithosphere is obtained (Fig. 1). The conductance σ_{crust} is assumed to be equal to 10^{-4} S.m. Fig. 1 shows the amplitude decrease (in relative units) versus distance r for varying frequencies: 0.001 Hz, 0.01 Hz, 0.1 Hz, and 1 Hz. For higher frequencies, the signal decrease is substantially stronger. Fig. 2 demonstrates the dependence of the decrease of a signal of given frequency when the signal penetrates through a medium of varying conductances. Such a dependence has to be observed for the spectral components of aperiodic electric field signals.

The frequency dependence of the ULF signal results in:

for periodic signals – different depth of penetration depending on the frequency; thus, signals of higher frequencies could not reach the Earth's surface and/or would not be detected at the measurement point;

for aperiodic signals – change of the spectral content of the signal; the disappearance of the higher frequencies would be observed like a smoothing of the signal envelope. This process depends on the distance between the source and the measurement point.

Following this general outcome, an important conclusion could be drawn. At a measurement point that is displaced at tens, or hundreds of kilometers away from the epicenter of the forthcoming earthquake, or the source of the ULF disturbance that accompanies the earthquake, only aperiodic, or quasi-static signals of large spatial scales and of frequency spectrum strongly limited from above can be detected. Since ULF electric disturbances of smaller scales (less than several km) cannot be periodic [2], at such measurement points, only aperiodic disturbance can be detected.

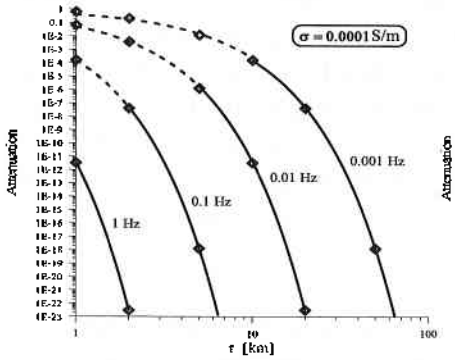

Fig. 1

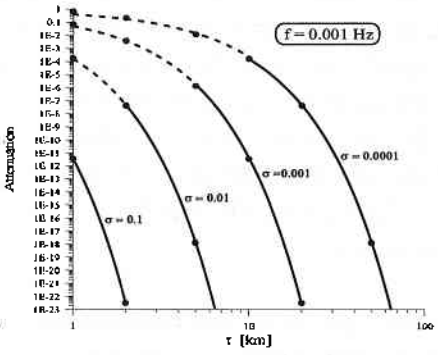

Fig. 2

4. Method of Frequency Selection of ULF Signals

The ULF signals of magnetospheric and lithospheric origin posses similar frequency spectra. The similarity of the frequency spectra suggests a discrimination of the signals using other signal features. A strategy for electric and magnetic field measurements of such ULF signals should rely on the locality of the signals of lithospheric origin and the relative homogeneity of the signals of magnetospheric origin because of the greater scales of the latter. The higher frequency components of the signal generated from the medium will disappear much faster than those of the lower frequency components. It follows that when the distance r changes, not only the overall amplitude should decrease, but the spectral content of the lithospheric signal should be altered. Irrespectively of the initial

amplitude and the spectral content, the amplitude of the higher components decreases up to 10^{-3} times the amplitude of the lower or zero frequency components for distances of 20–100 km and middle Earth conductance values. The ULF signals of lithospheric origin in the form of Earth electric potential (EEP) variations belongs to a limited frequency band usually below 0.02 Hz and have amplitude range of 0.01-100 mV depending on the lithospheric conductance and the distance between the sensors. As for the study of geomagnetic pulsations of magnetospheric origin, the following frequency interval of measurement is chosen: 0.002–1 Hz [2].

On the basis of the above considerations, a new method of discrimination of the ULF signals is suggested. This method is based on the frequency selection principle [2]. It is suggested that both types of signals be recorded by a common sensor system and common amplification, followed by filtration and treatment in separate frequency ranges. Then:

- At the measurement point, both signals are discriminated in different amplitude ranges. The comparison of their possible maximal amplitudes produces a ratio of 10^2 in favour of the lithospheric ones;
- Signals of different genesis are displaced in adjacent frequency regions overlapping in a tight frequency interval. An identification of the signals in the frequency interval where both signals overlap is possible by using additional characteristics depending on their genesis. Here are the different polarization characteristics and the local signature of the lithospheric signal.

5. Description of the Equipment and Operational Flow-Chart

We are presenting an instrument designed for selective measurement of the electric and magnetic components of ULF signals of lithospheric and magnetospheric origin at the Earth's surface. The electric pulsations are measured in DC – 1 Hz frequency range. Due to the large amplitude variations of the signals, the whole DC - 1 Hz frequency range is divided into 2 sub-bands: DC - 0.02 Hz (BW1) and 0.002 - 1 Hz (BW2). This allows for parallel processing of the signals from both sub-bands. Magnetic components are measured in BW2 sub-band only. Both the magnetic and the electric signals are measured in the East-West and the North-South direction. The instrument consists of sensors, analogue module, digital interface block, IBM compatible PC, and a modem. The instrument allows for:

1. Stand-alone operation at remote sites.

2. Multi-point synchronized observations and centralized data acquisition.

Sensors. The electrical sensors are corrosion-resistant metal bodies, buried in the ground. Depending on the soil's composition and the level of moisture saturation, the contact sensor-ground resistance varies in the range 50 Ω - 50 kΩ. The sensors are placed at a distance of several hundreds of meters from each other and from the instrument. The magnetic sensors are separate units with their own power supply.

Analogue Module. The analogue module is galvanically decoupled from the digital module and the PC through optocouplers, with a separate power supply. The overall flow-chart is shown in Fig. 3. The analogue module deals with the correct reception, amplification and subsequent discrimination of the signals derived from the electric and the magnetic sensors. The signals are divided into 2 sub-bands and converted into digital pulses of varying frequencies. The input resistance (Rin) of the electric sensors is greater than 10^{12} Ω. The filter (F) suppresses parasite signals outside the active DC-1 Hz bandwidth, especially those from industrial power lines 50 Hz/60 Hz and their respective harmonics. The Instrumentation Amplifier (IA) provides the signal difference between each pair of electric sensors for further processing. The Low Pass Filters (LPF), High Pass Filters (HPF) and the Amplifier (A) divide the signals from each pair of electric sensors into two sub-bands. The same procedure is followed for the signals from the magnetic sensors in the BW2 band. Each of the analogue signals is then converted into pulse sequences of varying frequencies, using Voltage-Frequency Converter (VFC) and then fed into the digital module via optocouplers (O).

Digital module. The digital module works as a frequency meter. The number of pulses in each pulse sequence, counted within a time frame of 0.1 s, defines the instant frequency of the respective channel. The digital module converts the instant frequencies into 12 bit words and stores them in the PC. The sampling rate of the BW1 range is 1/60 Hz, while that of the BW2 range is 5 Hz. The digital module is designed in such a way as to be directly integrated into the IBM AT PC. The digital module also generates commands controlling the calibration of the analogue module. In Fig. 3, the digital module is marked as INTERFACE

A supporting software package is developed to assure to proper functioning of the instrument. It consists of software, supporting the measurements (MS) and software, supporting the data acquisition (DAS).

MS performs the real-time astronomic synchronization and re-scaling of the measured signals and their storage in the local PC. MS provides a visualization of the measured signals from BW2 bands in the last 90 seconds and the signals from BW1 bands in the last 9 hours. DAS is responsible for acquisition and collection of the data from all measurement sites. DAS supports an operational database. The software package supports the transfer of data from the measurement sites and acquisition center through modems.

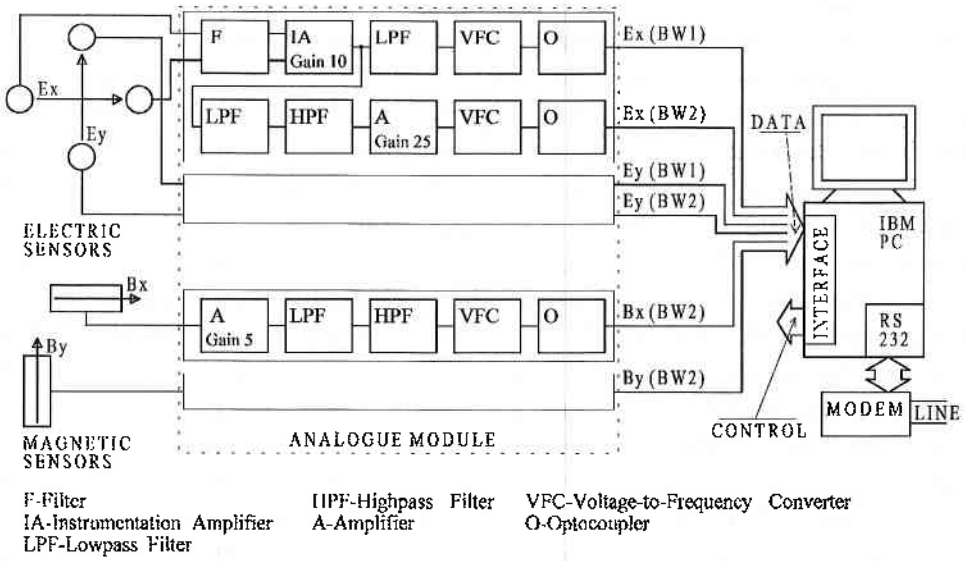

Fig. 3 The instrument's operational flow-chart.

6. Summary of the Instrument's Technical Characteristics

1. The input electric signals are differential voltage between two sensors placed in the ground at a distance of 100–500 m. The electric sensors are connected to the instrument by isolated non-shielded wires. The magnetic sensors, placed at a distance of 25 m from the instrument, are connected by shielded cables.

2. Dynamic range and frequency range:

2.1. The dynamic range of the quasi-static electric signals in the frequency band DC ÷ 0.02 Hz is -0.5 V ÷ +0.5 V.

2.2. The dynamic range of the electric signals in the frequency band 0.002 Hz ÷ 1 Hz is -0.02 V ÷ +0.02 V.

2.3. The dynamic range of the magnetic field signals in the frequency band 0.002 Hz ÷ 1 Hz is -2.10^{-6} T ÷ $+2.10^{-6}$ T with resolution: ± 1.10^{-9} T.

3. Filtering and electromagnetic compatibility:

The input filter (F) consists of two parts with a buffer repeater between them. The entire damping for disturbances in sin-phase with a power-line frequency of 50 Hz exceeds 100 dB.

7. Observational Data

The periodograms, shown in Figs. 4 and 5 for daytime and nighttime conditions respectively, illustrate the evidence of long-period pulsations observed by the measuring system. The spectrum in the figures is obtained during daylight and night hours. The daylight spectrum consists of three periods: ~ 300, 600 and 900 s. The spectral component with period T = 300 s is the most intense one. Under night conditions, the periods of the spectral components increase to 1,000 s and more.

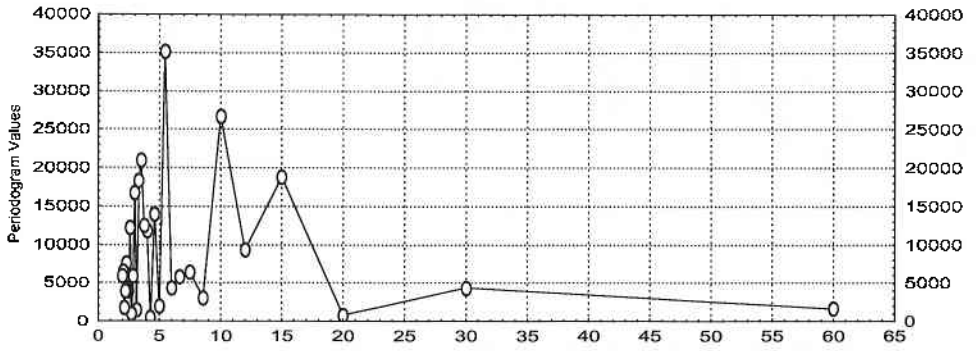

Fig. 4 Periodogram of day-hour pulsation (Period in minutes). Pulsations of period ~ 5 min and their harmonics at 10 and 15 min are clearly observed.

Our preliminary data set reveals the existence of geo-electric pulsations in the 60–1,800 s range. The period of these pulsations appears to vary from day to day. This means that the processes responsible for their generation have a time scale of several hours or less. Our preliminary conclusion is that their energy source is probably of ionospheric origin.

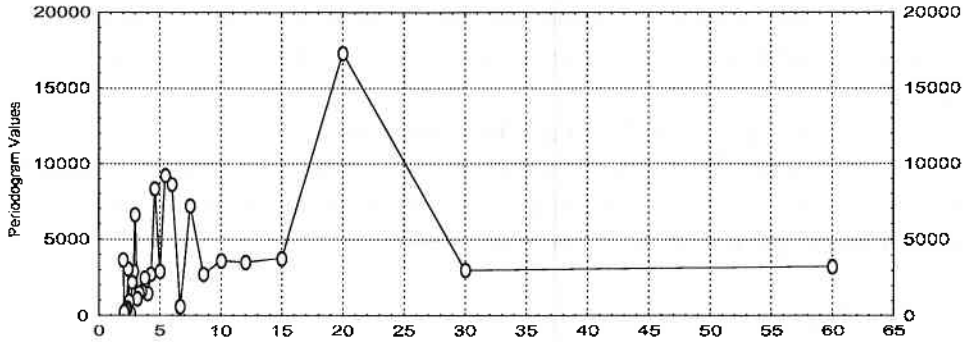

Fig. 5 Periodogram of night-hour pulsation (Period in minutes). Pulsations of period 20 min are observed.

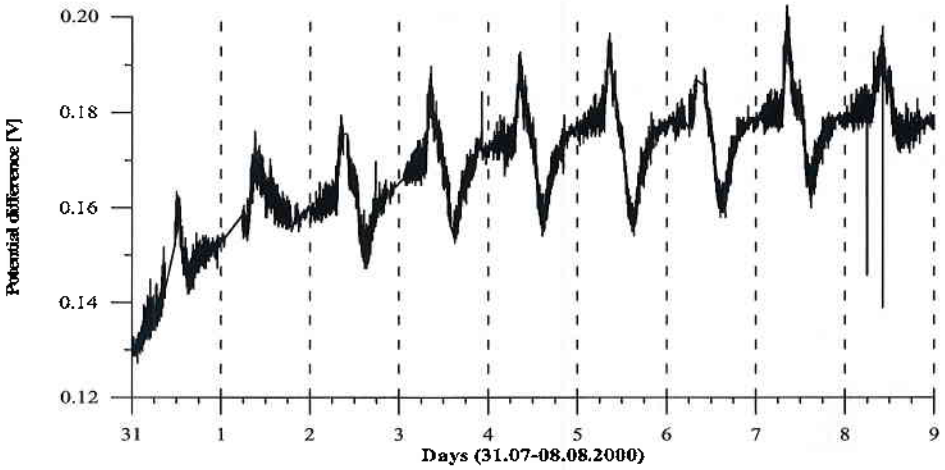

Fig. 6 Long-term drift of the Earth quasi-static electric potential.

Another feature of our ULF measurements during July 27 – August 08, 2000, is a slow increase (drift) of the magnitude of the Earth's electric potential φ (Fig. 6). This drift (measured over the whole interval) does not exceed the diurnal (regular) variations and is less than 20–30 percent of the mean potential. Ralchovski and Komarov [7] have already observed long-term drifts of the Earth's electric potential. A long-term change in φ at the same station (Vitosha) has had nearly half-a-month duration before the Vrancea earthquake in March 1986. This could be ascribed to possible changes in the Earth's conductivity during earthquake preparation processes. Our Earth electric potential drift is followed by two earthquakes of magnitude M > 5 which occurred on August 23, 2000, in Vrancea

(Romania) and Izmir (Turkey). Although our data set shows the same feature as in March 1986, the data set is insufficient to connect this drift to lithospheric conductivity changes.

8. Conclusion

We have provided theoretical grounds for the advantage of recording the electric field of ULF signals of both ionospheric (magnetospheric) and lithospheric origin.

We have designed an instrument that includes two principal measuring tracks: first, quasi-static geo-electric variations (originating from the magnetosphere and/or lithosphere) superimposed on the diurnal changes in pulsation dynamics; second, ULF geo-electric variations of periods 0.002 Hz to 1 Hz. It provides ULF wave measurements of higher sensitivity.

We have recorded ULF oscillations of period 300–1,200 s from both measurement tracks. Our preliminary conclusion is that these oscillations have unstable periods.

References

1. A k a s o f u, S. I., S. C h a p m a n, Solar-terrestrial physics, Oxford Univ. Press, Oxford, UK, 1972.
2. B o y t c h e v, B. V., Methods and means for measurement of low-frequency electromagnetic fields of magnetospheric and lithospheric origin, PhD Thesis, Space Research Institute, Sofia, Bulgaria, 2003. (In Bulgarian)
3. J u n g i n g e r, II., A statistical study of wave Pointing vectors measured during long-period magnetospheric pulsations at geostationary orbit, J. Geophys. Res., **90**, 8301-8307,1985.
4. S e m e n o v, A. A. Theoriya electromagnitnyh voln, Moscow University, Moscow, 1968. (In Russian)
5. S o r o k in, V. M. F e d o r o v i c h, G. V., Fizika bavnih magnitogidrodinamicheskih voln v ionosfernoi plazme, Energoizdat, Moscow, 1982. (In Russian)
6. S t r a t t o n, J. A., Electromagnetic Theory, Mc Graw-Hill, New York, NY, USA, 1941.
7. R a l c h o v s k i T., L. K o m a r o v, The Vranchea earthquake of 31.08.1986 and Its Possible Electrical Precursors, Bulg. Geophys. J., 13, 59-64, 1987.
8. V a r o t s o s, P. M. L a z a r i d o u, Latest aspects of earthquake prediction in Greece based on Seismic Electric Signals I, Tectonophysics, **188**, 321-347,1991.
9. V a r o t s o s, P., K. A l e x o p o u l o s, M. L a z a r i d o u, Latest aspects of earthquake prediction in Greece based on Seismic Electric Signals II, Tectonophysics, **224**, 1-37, 1993
10. Y u m o t o, K., Magnetospheric cavity resonances waves associated with substorm, Proc. Japan. Acad., **65**, Ser. B, 53-56, 1989.

МЕТОД И АПАРАТУРА ЗА ИЗМЕРВАНЕ И СЕЛЕКЦИЯ НА МАГНИТОСФЕРНИ И ЛИТОСФЕРНИ СИГНАЛИ НА ЗЕМНАТА ПОВЪРХНОСТ

Бойчо Бойчев

Резюме

В работата е направено изследване на параметрите на литосферните и индуцираните магнитосферни сигнали в земната повърхност. Изследвано е затихването на сигналите при тяхното разпространение. Предложен е метод за едновременното им измерване и селекция. Представени са и детайлно описани измервателна апаратура и система за многоточкови измервания реализиращи този метод. Представени са данни от измерванията, илюстриращи работата на апаратурата на два измервателни полигона.

Bulgarian Academy of Sciences. Space Research Institute.
Aerospace Research in Bulgaria. 19, 2005, Sofia

"OSCILLATOR-WAVE" MODEL AS AN INHOMOGENEOUSLY DRIVEN DYNAMICAL SYSTEM

Vladimir Damgov, Nikolay Erokhin**, Plamen. Trenchev**

** Space Research Institute, Bulgarian Academy of Sciences*
*** Space Research Institute, Russian Academy of Sciences*

Abstract

A generalized model of an oscillator is considered, subject to the influence of external waves. It is shown that the systems of diverse physical background, encompassed by this model, should belong by their nature to the broader class of "kick-excited self-adaptive dynamical systems". The theoretical treatment includes an analytic approach to the conditions for emergence of small and large amplitudes, i.e. weak and strong non-linearity of the system.

The article also considers the presence of a small horseshoe in the dynamics of a particle under the action of two waves. Originally, the problem comes from the plasma physics despite the existence of some other applications of the differential equation studied here.

1. Introduction

Here, the generalized "oscillator-wave" model is considered and it is shown that the inhomogeneous external influence is realized naturally and does not require any specific conditions. The systems covered by the "oscillation-wave" model immanently belong to the generalized class of kick-excited self-adaptive dynamical systems [1-5]. Attempting maximal clarity of the sequence of presentation, we consider the excitation of oscillations in a non-linear oscillator of the "pendulum" type under the influence of an incoming (fall) wave. We will show that, under certain condition, non-attenuated oscillations will arise in the system with a frequency close to the system's natural frequency and amplitude belonging to a defined discrete spectrum of possible amplitudes. A second important quality also appears - self-adaptive stability of the excited oscillations with given amplitude for a

where Ω is the frequency of free oscillations having an amplitude a,

$$\Omega^2 = \frac{2J_1(a)}{a}\omega_o^2 \cong \omega_o^2\left[1 - \frac{a^2}{8} + O(a^4)\right],$$

$J_n(\cdot)$ are Bessel functions of the first kind, $F_o = \frac{Eq}{m}$.

The excitation of continuous oscillations with frequency $\omega = \omega_s$ close to the oscillator's natural frequency is only possible under the condition $\frac{2\pi}{\lambda}a > 1$, where λ is the wavelength of the influencing wave. As result of the interaction of the oscillator with the wave a frequency components appears in the force spectrum that is close to its natural oscillation frequency. Then the action of these spectral components becomes dominant and the right-hand side of equation (1) attains the form:

$$\frac{1}{m}Eq\sum_{n=-\infty}^{\infty}J_n(ka)\sin(\nu t - n\theta) =$$

$$= F_o\left\{J_{\frac{\nu}{\omega}-1}(ka)\sin\left[\omega t - (\frac{\nu}{\omega}-1)\alpha\right] - J_{\frac{\nu}{\omega}+1}(ka)\sin\left[\omega t + (\frac{\nu}{\omega}+1)\alpha\right]\right\} \qquad (5)$$

Under the condition $\nu > \omega$ the resonance area of the nonlinear oscillator can be entered by several spectral components of the exciting wave each of which could excite the oscillator into stationary oscillations with amplitude belonging to a discrete sequence of possible amplitudes. For fixed parameters of the oscillator and the wave the excitation of oscillations with amplitude from the possible sequence of amplitudes is determined by the initial conditions. In accordance with relation (4), the values of the discrete sequence of stationary amplitudes can be calculated by the formula:

$$a_{s0} = \sqrt{8\left(1 - \frac{\nu^2}{s^2\omega^2}\right)} \cong 4\sqrt{1 - \frac{\nu}{s\omega_o}}, \quad s = 1,2,3... \qquad (6)$$

Averaging the right-hand side of equations (3) and taking into account (5), we determine:

$$\begin{cases} \frac{da_s}{dt} = -\delta_d a + \frac{F_o}{2\omega_s}\left[J_{s-1}(ka_s) + J_{s+1}(ka_s)\right]\sin(pt - \gamma_s) \\ \frac{d\alpha_s}{dt} = \frac{\Omega^2 - \omega_s^2}{2\omega_s} - \frac{F_o}{2\omega_s a_s}\left[J_{s-1}(ka_s) - J_{s+1}(ka_s)\right]\sin(pt - \gamma_s) \end{cases}, \qquad (7)$$

broad range of the incoming wave's intensity.

Leaving the details, the equation describing the motion of one particle in two electrostatic waves allows perturbation methods to be applied in its study. There are three main types of behavior in the phase space - a limit cycle, formation of a non-trivial bounded attracting set and escape to infinity of the solutions. One of the goals is to determine the basins of attraction and to present a relevant bifurcation diagram for the transitions between different types of motion.

2. Model of the interaction of an oscillator with an electromagnetic wave: approach applicable for small amplitudes of the system's oscillations.

Let us consider the interaction of an electromagnetic wave with a weakly dissipative nonlinear oscillator. Let the electric charge q having mass m oscillate along the x-axis under the influence of a non-linear returning force around a certain fixed point. The electromagnetic wave also propagates along the x-axis and has a longitudinal electric field component E. The equation of motion for the charge interacting with the wave can be represented as:

$$m(\ddot{x} + 2\delta_d \dot{x} + \omega_o^2 \sin x) = Eq \sin(\nu t - kx) \tag{1}$$

where $2\delta_d$ is the damping coefficient, ω_0 is the natural frequency of small oscillations of the charge, ν is the wave frequency and k is the wave number. The case considered is: $\nu \gg \omega_0$.

We assume that the excitation of charge oscillations by the influence of the wave does not perturb significantly the symmetry of the charge's motion around its equilibrium position and the coordinate of the charge changes according to the law

$$x = a\sin\theta, \quad \theta = \omega t + \alpha, \quad a = a(t), \quad \alpha = \alpha(t) \tag{2}$$

Substituting the solution (2) in the right hand side of equation (1) we obtain:

$$Eq \sin(\nu t - ka\sin\theta) = Eq \sum_{n=-\infty}^{\infty} J_n(ka)\sin(\nu t - n\theta).$$

Letting $\dot{x} = a\omega\cos\theta, \quad \dot{a}\sin\theta + \dot{\alpha}a\cos\theta = 0$

in accordance with the Krilov-Bogolyubov-Mitropolskii method [6], we obtain to first order:

$$\begin{cases} \dfrac{da}{dt} = -2\delta_d a + \dfrac{F_o}{\omega}\displaystyle\sum_{n=-\infty}^{\infty} J_n(ka)\sin(\nu t - n\theta)\cos\theta \\ \dfrac{d\alpha}{dt} = \dfrac{\Omega^2 - \omega^2}{2\omega} - \dfrac{F_o}{\omega}\displaystyle\sum_{n=-\infty}^{\infty} J_n(ka)\sin(\nu t - n\theta)\cos\theta \end{cases} \tag{3}$$

where $p = \nu - \frac{\nu}{\omega_s} << \omega_s$, $\gamma_s = \frac{\nu}{\omega_s}\alpha_s$ $\omega_s = \frac{\nu}{s}$.

In accordance with the familiar recurrence relations for Bessel functions, equations (7) can be represented in the form:

$$\begin{cases} \frac{da_s}{dt} = -\delta_d a_s - \frac{\nu F_o}{\omega_s^2 k a_s} J_s(ka_s)\sin(pt-\gamma_s) \\ \frac{d\alpha_s}{dt} = \frac{\Omega_s^2 - \omega_s^2}{2\omega_s} - \frac{F_o}{\omega_s a_s} J'_s(ka_s)\cos(pt-\gamma_s) \end{cases} \quad (8)$$

In the case of stationary oscillations ($\frac{da_s}{dt} = 0$ and $\frac{d\alpha_s}{dt} = 0$) from equations (8) we find:

$$tg\gamma_s = \frac{2\delta_d a_s \omega_s^2 k}{(\Omega_s^2 - \omega_s^2)\nu} \frac{J'_s(ka_s)}{J_s(ka_s)}$$

The connection between the intensity of the wave's longitudinal component and the amplitude of oscillations has the form:

$$F_o^2 = \left[\frac{a_{so}^2 \omega_s^2 \delta_d k}{\nu J_s(ka_{so})}\right]^2 + \left[\frac{a_{so}(\Omega_s^2 - \omega_s^2)}{2J'_s(ka_{so})}\right]^2. \quad (9)$$

For high intensities of the wave, equation (9) can be represented as:

$$F_o = \frac{a_{so}^2 \omega_s^2 (a_s - a_{so})}{8J'_s(ka_s)}.$$

The first term in formula (9) represents the minimal threshold value F_o of the wave's intensity. If the intensity of the wave is smaller than this threshold value only the excitation of forced oscillations with frequency equal to the wave's frequency is possible. For wave intensities above the threshold value depending on the initial conditions, the oscillator's motion is realized with one of the amplitudes from the discrete sequence (6). When $\nu > \omega_0$ each amplitude is realized for oscillation frequency close to the oscillator's natural frequency. Using the approach, developed in [3], it is not difficult to show that for fixed values of the frequency ν and the amplitude F_o of the external force the oscillator's motion with amplitude from the discrete sequence (6) is stable.

The performed analysis shows that the continuous wave having a frequency much larger than the frequency of a given oscillator can excite in it oscillations with a frequency close to its natural frequency and an amplitude belonging to a discrete set of possible stable amplitudes.

The settling of certain particular amplitude depends on the initial

conditions. When the motion becomes stationary the amplitude's value practically does not depend on the wave's intensity when the latter changes over a significant range above a certain threshold value. This is reminiscent of Einstein's explanation of the photoelectric effect using Planck's quantization hypothesis. In this case the absorption is also independent of the incoming wave's intensity. Besides, the absorbed frequencies can be expressed as integer multiples of a certain basic frequency reminding of resonance phenomena.

3. Approach for large amplitudes of the oscillations in a nonlinear dynamical system subjected to the influence of a wave

Let the nonlinear oscillator is an electric charge q with mass m and it is able to oscillate along the X-axis with a small friction force $2\delta_o \dot{X}$. Let an electromagnetic wave propagating along the X-axis acts upon the oscillating charge. Let us assume that the wave has a longitudinal component of the electric field E_X. The equation of the charge motion becomes

$$\ddot{X} + 2\delta_o \dot{X} + \omega_o^2 \sin X = P_o \sin(\nu t_r - kX - \varphi), \qquad (10)$$

where ω_o is the resonant frequency of small amplitude oscillations $P_o = E_X q / m$; ν, φ and k are the frequency, the initial phase and the wave number respectively, t_r is the real time. We assume $\nu >> \omega_o$.

Let us introduce the dimensionless time $t = \omega_o t_r$. In this case, Eq. (10) takes the form

$$\ddot{X} + 2\delta_d \dot{X} + \sin X = F_o \sin(\frac{\nu}{\omega_o} t - kX - \varphi),^{*)} \qquad (11)$$

where $2\delta_d = 2\delta_o / \omega_o$, $F_o = P_o / \omega_o^2$

In order to integrate the Eq. (11) with the methods of the Theory of nonlinear oscillations, we apply the approach developed in [3, 7]. We introduce a new variable y and nonlinear time τ,

$$y = \operatorname{sign} x \sqrt{2 \int_0^x \sin x' \, dx'} = 2 \sin \frac{x}{2}, \qquad (12)$$

---

*) Similar equations describe the behavior of cosmic charged particles in certain conditions, the processes in radio-frequency driven, quantum-mechanical Josephson junctions, charge density wave transport and other systems.

$$\frac{dt}{d\tau}=\frac{dX}{dy}=\frac{y}{\sin[X(y)]}=G(y) \qquad (13)$$

So, the nonlinear reactive term $\sin X$ in the Eq. (11) may be "excluded". The functions $X(y)$ and $G(y)$ in (13) are easily expressed by taking into account (12) in the form

$$X(y)=2\arcsin\left(\frac{y}{2}\right),\quad G(y)=\frac{1}{\sqrt{1-\frac{y^2}{4}}} \qquad (14)$$

Substituting (12) and (13) in (11) we obtain

$$\frac{d^2y}{d\tau^2}+y=\left\{-2\delta_d\frac{dy}{d\tau}+F_o\sin\left[\frac{\nu}{\omega_o}t(\tau)-kX(y)-\varphi\right]\right\}G(y) \qquad (15)$$

The further consideration will be performed for the following interval of y values: $-2<y<2$.

Before the integration of the Eq. (15) we will mention, that the solution will be quasi-harmonic with nominal frequency $\omega_n=\nu/N$, where $N>>1$ is a positive odd number, however $\omega_n\sim\omega_o$. That is why we will write the Eq. (15) in the following form:

$$\frac{d^2y}{d\tau^2}+\beta^2y=-2\delta_d\frac{dy}{d\tau}+F_o\sin\left[\frac{\nu}{\omega_o}t(\tau)-kX(y)-\varphi\right]G(y)+(\beta^2-1)y, \qquad (16)$$

where $\beta\sim1$ corresponds to the difference from the resonant frequency.

We assume that in excitation of the charge oscillations by the wave its motion is symmetric with respect to the equilibrium and the charge coordinate changes in agreement with

$$y=R\cos\beta\tau=R\cos\psi \qquad (17)$$

The dependence of the normalized time t on the angle ψ can be expressed in agreement with (13), (14) and (17) as

$$t=\frac{1}{\beta}\int_0^{\psi}\frac{d\Psi}{\sqrt{1-\frac{R^2}{4}\cos^2\Psi}}.$$

The normalized period of the oscillations is

$$T_o=\frac{1}{\beta}\int_0^{2\pi}\frac{d\Psi}{\sqrt{1-\frac{R^2}{4}\cos^2\Psi}}=\frac{4}{\beta}K\left(\frac{R}{2}\right), \qquad (18)$$

where $K\left(\frac{R}{2}\right)$ is a complete elliptic integral of first kind.

By use of (18) the coefficient β is expressed in the form

$$\beta = \frac{2\nu K\left(\frac{R}{2}\right)}{\pi\omega_o N}.$$

Now we can solve Equation (16).

The shortened (reduced) differential equations for the amplitude R and phase φ may be written as:

$$\frac{dR}{d\tau} = -\frac{1}{2\pi\beta}\int_0^{2\pi} L[R\cos\psi, -\beta R\sin\psi, e(\psi-\varphi)]\sin\psi d\psi, \qquad (19)$$

$$\frac{d\varphi}{d\tau} = -\frac{1}{2\pi\beta}\int_0^{2\pi} L[R\cos\psi, -\beta R\sin\psi, e(\psi-\varphi)]\cos\psi d\psi, \qquad (20)$$

where

$$L[R\cos\psi, -\beta R\sin\psi, e(\psi-\varphi)] = 2\delta_d\beta R\sin\psi + \frac{F_o}{\sqrt{1-R^2/4\cos^2\psi}}\sin\left[\frac{\pi N}{2K(R/2)}\right]$$

Let us introduce the following designations:

$$\begin{Bmatrix} H_1 \\ H_2 \end{Bmatrix} = \int_0^{K(R/2)} \sin(rZ)\cos[D(Z)]\begin{Bmatrix} \mathrm{sn}Z \\ \mathrm{cn}Z \end{Bmatrix} dz, \qquad (21)$$

$$\begin{Bmatrix} H_3 \\ H4 \end{Bmatrix} = \int_0^{K(R/2)} \cos(rZ)\sin[D(Z)]\begin{Bmatrix} \mathrm{sn}Z \\ \mathrm{cn}Z \end{Bmatrix} dZ \qquad (22)$$

$$\begin{Bmatrix} H_5 \\ H6 \end{Bmatrix} = \int_0^{K(R/2)} \cos(rZ)\cos[D(Z)]\begin{Bmatrix} \mathrm{sn}Z \\ \mathrm{cn}Z \end{Bmatrix} dZ \qquad (23)$$

$$\begin{Bmatrix} H_7 \\ H8 \end{Bmatrix} = \int_0^{K(R/2)} \sin(rZ)\sin[D(Z)]\begin{Bmatrix} \mathrm{sn}Z \\ \mathrm{cn}Z \end{Bmatrix} dZ \qquad (24)$$

where $Z = F(\psi, R/2)$ is an incomplete elliptic integral of the first kind,

$D(Z) = 2kE\left[\arcsin\left(\frac{R}{2}cnZ\right), \frac{2}{R}\right]$, E[·,·] is an incomplete elliptic integral of second kind, snZ and cnZ are sine and cosine of the amplitude

(the Jacobi elliptic functions),

$$r = \frac{\pi N}{2K(R/2)}.$$

Taking into account the expressions (21)-(24), the shortened Equations (19) and (20) for establishing the amplitude R and phase φ take the form

$$\frac{dR}{d\tau} = -\delta_d R - \frac{F_o}{2\pi\beta}\left[(H_1 - H_3)\cos\varphi - (H_5 + H_7)\sin\varphi\right],$$

$$\frac{d\varphi}{d\tau} = -\frac{F_o}{2\pi\beta R}\left[(H_2 - H_4)\cos\varphi - (H_6 + H_8)\sin\varphi\right] - (\beta - 1)..$$

For the stationary mode ($\frac{dR}{d\tau} = 0$, $\frac{d\varphi}{d\tau} = 0$) we obtain the following expressions for the established values of the amplitude R and the phase φ:

$$R = \frac{F_o\left[(H_1 - H_3)(H_6 - H_8) - (H_2 - H_4)(H_5 + H_7)\right]}{2\pi\beta\delta\sqrt{\left[\sigma(H_1 - H_3) - (H_2 - H_4)\right]^2 + \left[\sigma(H_5 + H_7) - (H_6 + H_8)\right]^2}} \quad (25)$$

$$\varphi = arctg\frac{\sigma(H_1 - H_3) - (H_2 - H_4)}{\sigma(H_5 + H_7) - (H_6 + H_8)} \quad (26)$$

where $\sigma = (\beta - 1)/\delta_d$.

4. Presence of a small horseshoe in the dynamics of a particle under the action of two waves

Originally the problem comes from plasma physics [8] even though that there exist and some other applications of the differential equation which we shall study. Leaving the details, the equation which describes the motion of one particle in two electrostatic waves is given by

$$\ddot{x} = -M\sin x - P\sin(x - t), \quad (27)$$

where x is the position of the particle measured in the frame of one of the waves, P and M are dimensionless amplitudes of the waves. We shall extend our model introducing a damping term in (27), and we shall also assume that $P << M$. Under these assumptions the equation that governs the motion of the particle can be written as

$$\ddot{x} + \varepsilon\delta\dot{x} + \sin x = \varepsilon f\sin(\nu t - x), \quad (28)$$

where x is again the position of the particle measured in the frame of one of the waves, whereas δ, f and ν are real non-negative constants. The form of the equation allows perturbation methods to be applied in

its study. Our preliminary numerical investigation of (28) revealed very rich dynamics depending on the change of parameters and initial conditions. There are three main types of behaviour in the phase space of (28) that can be observed:

- Approaching a limit cycle;
- Formation of a non-trivial bounded attracting set;
- Escape to infinity of the solutions of (28).

One question which is of natural interest here, is to determine the basins of attraction, and to present a relevant bifurcation diagram for the transitions between different types of motion. Although that there has been reached a significant progress in the understanding of the behavior of driven non-linear oscillators, there exist some obstacles that prevent clarifying the dynamics of particular examples. In our work we present a rigorous result for existence of horseshoe-like dynamics for (28) and hence for exhibiting the phenomena deterministic chaos. Our result is as follows:

Theorem 1. *The sufficient conditions for transition to chaotic motion in the dynamics of equality* (28) *is fulfillment of*

$$4\delta < f\pi v^2\left(\frac{1}{\cosh(\pi v/2)} - \frac{1}{\sinh(\pi v/2)}\right), \tag{29}$$

or

$$4\delta < f\pi v^2\left(\frac{1}{\cosh(\pi v/2)} + \frac{1}{\sinh(\pi v/2)}\right). \tag{30}$$

The organization of our study is as follows: In next section we shall give a short account of the Melnikov method in form convenient for our problem. Then we shall prove Theorem 1. In the last section we shall say some words on the physical implication of our result.

4.1. Short summary of the Melnikov method

We shall explain the Melnikov technique following [9].

A. General assumptions and geometric structure of the non-perturbed system.

Consider the system of differential equations

$$\dot{x} = JD_x H(x) + \varepsilon g(x,t,\varepsilon) \tag{31}$$

where $(x,t) \in R^2 \times T^1$ and J is the symplectic matrix defined by $J = \begin{bmatrix} 0 & 1 \\ -1 & 0 \end{bmatrix}$.

We get the following structural assumptions:

1. The functions

$$JD_x H : R^2 \to R^2$$

$$g : R^2 \times R \times R \to R^2,$$

are defined and at least C^2 differentiable on their respective domains of definition, and that g is periodic in t with period $T = 2\pi / \omega$.

2. The system (31) with $\varepsilon = 0$ is referred as *unperturbed system.* About it we shall assume that it possesses a hyperbolic fixed point $x_{o,h}$ connected to itself by a homoclinic orbit $x_h(t) \equiv (x_h^1(t), x_h^2(t))$.

3. Let denote by $W^s(x_{0,h})$ the set of points $x \in R^2$ that approach $x_{0,h}$ as $t \to \infty$, and by $W^u(x_{0,h})$ the set of points $x \in R^2$ that approach $x_{0,h}$ as $t \to -\infty$, under the action of the unperturbed flow

$$\dot{x} = JD_x H(x) \tag{32}$$

$W^s(x_{0,h})$ is referred as *asymptotically stable manifold* for $x_{0,h}$, and $W^u(x_{0,h})$ is referred as *asymptotically unstable manifold* for $x_{0,h}$. Denote by $\Gamma_{x_{o,h}} \equiv \{x \in R^2 \mid x = x_h(t), t \in R\} \cup \{x_{0,h}\} = W^s(x_{0,h}) \cap W^u(x_{0,h}) \cup \{x_{0,h}\}$. We shall assume that interior of $\Gamma_{x_{o,h}}$ is filled with continuous family of periodic orbits $x^\alpha(t)$ of (32) with period T^α, $\alpha \in [-1, 0]$ and $\lim_{\alpha \to 0} x^\alpha(t) = x_h(t)$ and $\lim_{\alpha \to 0} T^\alpha = \infty$.

When viewed in three-dimensional space $R^2 \times S$, the hyperbolic fixed point $x_{0,h}$ turns to hyperbolic periodic orbit $\gamma(t) \equiv \{x_{0,h}, \theta(t) = \omega t + \omega_o\}$ of the system

$$\begin{aligned} \dot{x} &= JD_x H(x) \\ \dot{\theta} &= \omega \end{aligned} \tag{33}$$

and so do $W^s(x_{0,h})$ and $W^u(x_{0,h})$ which turn to two-dimensional asymptotic manifolds $W^s(\gamma(t))$ and $W^u(\gamma(t))$ which coincide along the two-dimensional homoclinic manifold

$$\Gamma_{\gamma(t)} \equiv \{(x,\theta) \in R^2 \times S \mid x = x_h(t), t \in R\} \cup \{x_{0,h} \times S\}.$$

B. Geometric structure of the perturbed phase space.

Here we shall argue that most of the upper structure goes over for the perturbed system.

$$\begin{aligned} \dot{x} &= JD_x H(x) + \varepsilon g(x,\theta,\varepsilon) \\ \dot{\theta} &= \omega \end{aligned} \tag{34}$$

Proposition 1. *For ε sufficiently small the periodic orbit $\gamma(t)$ of (7) survives as a periodic orbit, $\gamma_\varepsilon(t) = \gamma(t) + O(\varepsilon)$, of (34) having the same stability type as $\gamma(t)$, and depending on ε in a C^2 manner. Moreover, the local stable and unstable manifolds $W^s_{loc}(\gamma_\varepsilon(t))$ and $W^u_{loc}(\gamma_\varepsilon(t))$ of $\gamma_\varepsilon(t)$ remain also C^2 ε-close to the local stable and unstable manifolds $W^s_{loc}(\gamma(t))$ and $W^u_{loc}(\gamma(t))$ of $\gamma(t)$, respectively.*

Remark 1. *The concept for local stable and unstable manifolds becomes clear when one represents the stable and unstable manifolds of the hyperbolic fixed point (periodic orbit) locally. For details see* [9] *or* [10].

Now, the global stable and unstable manifolds of $\gamma_\varepsilon(t)$ are

$$W^s(\gamma_\varepsilon(t)) = \bigcup_{t \le 0} (x,\theta)^t \left(W^s_{loc}(\gamma_\varepsilon(t))\right),$$

$$W^u(\gamma_\varepsilon(t)) = \bigcup_{t \ge 0} (x,\theta)^t \left(W^u_{loc}(\gamma_\varepsilon(t))\right)$$

where we denote by $(x,\theta)^t$ the phase flow of (34).

Consider the following cross-section of the plane $R^2 \times S$

$$\Theta^{\theta_o} = \{(x,\theta) \in R^2 \mid \theta = \theta_o\}.$$

Θ^{θ_o} is parallel to the x-plane (and coincides with the x-plane for $\theta_o = 0$). Note that $\gamma(t) \cap \Theta^{\theta_o} = x_{o,h}$ and $\Gamma_\gamma \cap \Theta^{\theta_o} = \{x \in R^2 \mid x = x_{o,h}, t \in R\} = \Gamma_{x_{o,h}}$. Consider a trajectory

$$(x_\varepsilon(t), \theta(t)), \tag{35}$$

of the perturbed vector field (34). Then its projection onto Θ^{θ_o} is given by $(x_\varepsilon(t), \theta_o) = W^s(\gamma_\varepsilon(t)) \cap W^u(\gamma_\varepsilon(t))$. Since $x_\varepsilon(t)$ actually depends on θ_o (as opposed to $x(t)$, for some solutions $(x_\varepsilon(t), \theta(t)$ of (34)), the

perturbed vector field (34) is non-autonomous, which may result in a very complicated picture of (35) in Θ^{θ_o}, possibly intersecting itself. The points from the Poincare map P_ε defined as the successive points of intersection of the solution $(x_\varepsilon(t),\theta(t))$ with Θ^{θ_o}, will be mapped also onto this curve. It turns out that these points can form very complicated (non-trivial) sets due to transversal intersection of the asymptotic manifolds $W^s(\gamma_\varepsilon(t))$ and $W^u(\gamma_\varepsilon(t))$. One computable criterion that assures such dynamics is given by:

Proposition 2. [19] *Suppose that we have a point* $(t_o,\theta_o)=(\bar{t}_o,\bar{\theta}_o)$ *such that*

1. $M(\bar{t}_o,\bar{\theta}_o)=0$,
2. $\left.\dfrac{\partial M}{\partial t_o}\right|_{(\bar{t}_o,\bar{\theta}_o)}\neq 0$,

where $M(t_o,\theta_o)$ is *the Melnikov vector*

$$M(t_o,\theta_o)=\int_{-\infty}^{\infty} DH(x_h(t)).\mathrm{g}(\mathrm{x}_h(t),\omega t+\theta_o,0)dt$$

Then $W^s(\gamma_\varepsilon(t))$ *and* $W^u(\gamma_\varepsilon(t))$ *intersect transversely at* $(x_h(-\bar{t}_o)+O(\varepsilon),\bar{\theta}_o)$ *and consequently (from the Smale-Birkhoff homoclinic theorem) for the map* P_ε *there exists an integer* $n>1$ *that* P_ε^n *has an invariant Cantor set on which it is topologically conjugate to a full shift of N symbols.*

C. Proof of Theorem 1.

Consider equation (28) written in the form

$$\begin{aligned}\dot{x}^1&=x^2,\\ \dot{x}^2&=\sin x^1+\varepsilon[-\delta x^2+f\sin(\theta-x^1)],\\ \dot{\theta}&=\nu.\end{aligned}\qquad(36)$$

Then the following lemma holds:

Lemma 1. *For* $\varepsilon=0$ *system (36) contains hyperbolic periodic orbit*

$$M=(\bar{x}^1,\bar{x}^2,\theta(t))=(\pm\pi,0,\nu t+\theta_o)\in R^2\times T^1.$$

This orbit is connected to itself by a pair of 2-dimensional homoclinic manifolds given by

$$\left(x_{\pm}^1(t), x_{\pm}^2(t), \theta(t)\right) = \left(\pm 2\arcsin(\tanh(t-t_o)), \pm \frac{2}{\cosh(t-t_o)}, \nu t + \theta_o \right). \quad (37)$$

Proof. We easily see that $(\pm\pi, 0)$ is a hyperbolic fixed point of $\dot{x}^1 = x^2$, $\dot{x}^2 = \sin x^1$, linearizing (36) (for $\varepsilon = 0$) about it. A trivial check gives that (for $\varepsilon = 0$) (37) in solution of (36). Furthermore, using asymptotic of (37) we obtain that it connects $(\pm\pi, 0, \nu t + \theta_o)$ to itself. This proves the lemma.

Using Proposition 2 and hyperbolicity of (37), we conclude that for $\varepsilon \neq 0$, (37) turns to hyperbolic periodic, orbit which we shall shortly denote by $\gamma_{\varepsilon,+}(t) \equiv \left(\pm\pi + O(\varepsilon), 0 + O(\varepsilon), \nu t + \theta_o\right)$. From Proposition 2 it follows that its asymptotic manifolds $W^s\left(\gamma_{\varepsilon,+}(t)\right)$ and $W^u\left(\gamma_{\varepsilon,+}(t)\right)$ will intersect transversely if the corresponding Melnikov vector

$$M_{\pm}(t_o, \theta_o, \delta, f, \nu) =$$

$$= \int_{-\infty}^{\infty} \left[-\delta\left(x_{h,\pm}^2(t-t_o)\right)^2 + f\sin\left(\nu t + \theta_o - x_{h,\pm}^1(t-t_o)\right) x_{h,\pm}^2(t-t_o) \right] dt =$$

$$= \int_{-\infty}^{\infty} \left[-\delta\left(\frac{\pm 2}{\cosh(t-t_o)}\right)^2 + f\left(\frac{\pm 2}{\cosh(t-t_o)}\right) \sin(\nu t + \theta_o \pm 2\arcsin(\tanh(t-t_o))) \right] dt,$$

has a simple zero. Furthermore we fix $\theta = \theta_o$, which defines the cross-section

$$\Theta^{\theta_o} = \left\{ (x_1, x_2, \theta) \,|\, \theta = \theta_o \in [0, 2\pi) \right\},$$

and consider the Poincare map $P_{\varepsilon}^{\theta_o}: \Theta^{\theta_o} \to \Theta^{\theta_o}$ generated by the flow (36). In order to make the conclusions we pursue about the dynamics of $P_{\varepsilon}^{\theta_o}$ we need to compute $M_{\pm}(t_o, \theta_o, \delta, f, \nu)$. After some algebra we obtain for $M_{\pm}$

$$M_{\pm}(t_o, \theta_o, \delta, f, \nu) = -8\delta \pm 2f\sin(\nu t_o + \theta_o)\,[I_1 \mp 2I_2],$$

where

$$I_1 = \int_{-\infty}^{\infty} \frac{1 - \sinh^2\tau}{\cosh^3\tau} \cos(\nu\tau) d\tau = \nu \int_{-\infty}^{\infty} \frac{\sinh\tau}{\cosh^2\tau} \sin(\nu\tau) d\tau,$$

$$I_2 = \int_{-\infty}^{\infty} \frac{\sinh\tau}{\cosh^3\tau} \sin(\nu\tau) d\tau = \frac{\nu}{2} \int_{-\infty}^{\infty} \frac{1\sinh\tau}{\cosh^2\tau} \cos(\nu\tau) d\tau.$$

The integrals I_1 and I_2 are evaluated by the methods of residues. The standard calculation gives

$$I_1 = \frac{\pi v^2}{\cosh(\pi v/2)}; \quad \text{and} \quad I_2 = \frac{\pi v^2}{2\sinh(\pi v/2)}.$$

Hence, for the Melnikov vector $M_\pm$ we obtain

$$M_\pm(t_o, \theta_o, \delta, f, v) = -8\delta \pm 2f\pi v^2 \left[\frac{1}{\cosh(\pi v/2)} \mp \frac{1}{\sinh(\pi v/2)}\right] \sin(vt_o + \theta_o) \tag{38}$$

Then fulfillment of (3) assures existence of simple zero for

$$M_+(t_o, \theta_o, \delta, f, v) = 0,$$

and hence transversal intersection of the asymptotically stable manifold $W^s(\gamma_{\varepsilon,+})$ and asymptotically unstable manifold $W^u(\gamma_{\varepsilon,+})$, whereas the fulfillment of (30) assures existence of simple zero for

$$M_-(t_o, \theta_o, \delta, f, v) = 0$$

and hence transversal intersection of $W^s(\gamma_{\varepsilon,-})$ and $W^u(\gamma_{\varepsilon,-})$. Now, from Proposition 2 it follows for $\varepsilon > 0$ sufficiently small there exists an integer $n > 1$ such that the map $P_\varepsilon^{\theta_o}$ has an invariant Cantor set, subset of the Poincare section Θ^{θ_o}, on which the power $(P_\varepsilon^{\theta_o})$ is conjugate to a full shift of N symbols.

The last implies that high sensitiveness of solution to the choice of initial conditions, or equivalently deterministic chaos.

5. Conclusion

The analysis shows the following two essential features of the system considered.

1. There exists a discrete set of possible stationary stable amplitudes, which can be approximately determined under certain conditions.
2. There exists a threshold value for the amplitude such that for values above it the discrete states are stable.

The phenomenon of continuous oscillation excitation with amplitude belonging to a discrete set of stationary amplitudes has been demonstrated on the basis of a common model – an oscillator under wave influence. It is shown that the conditions necessary for the manifestation of this phenomenon are realized in a natural way in an oscillator system interacting with a continuous electromagnetic wave.

Modeling the system of an oscillating charge under wave influence has

been considered. It has been shown that the continuous wave with spectral components, considerably higher than the oscillating charge's natural frequency, excites charge oscillations with a quasi-natural frequency and amplitude belonging to a discrete set of the possible stationary amplitudes, depending only on the initial conditions. The considered model may be used for phenomenological investigation of plasma particles with electromagnetic waves interactions and waves in the Earth ionosphere and planetary magnetospheres.

In fact the main consequence of Theorem 1 is the strong dependence of the solution of (28) on the choice of initial conditions. The phenomenon deterministic chaos arises often in the dynamics of the driven non-linear oscillators. In this regard our result is not surprising. Anyway, we think that it is useful to present such a condition for the parameters of the system which guarantees appearance of a Smale horseshoe like dynamics, since usually the homoclinic bifurcation (due to a simple zero of the Melnikov vector) is one of the first bifurcations that occur in the transition from regular to irregular motion for **a** given system. We want to emphasis that the homoclinic tangency (predicted with a good accuracy by the Melnikov analysis), as a rule, implies formation of a fractal boundary for the basins of attraction. The last makes difficult clarifying the global dynamics on specific examples. The other two types of motion, outlined in section 4, are treated by the means of the averaging theory using a sub-harmonic Melnikov function. Our results are subject to a forthcoming paper.

References

1. D a m g o v, V. and I.Popov. "Discrete" Oscillations and Multiple Attractors in Kick-Excited Systems. *Discrete Dynamics in Nature and Society (An International Multidisciplinary research and Review Journal)* 3(No.6), 1-26 (1999)
2. D a m g o v, V.. "Quantized" Oscillations and Irregular Behaviour of a Class of Kick-Excited Self-Adaptive Dynamical Systems. *Progress of Theoretical Physics Supplement, Kyoto, Japan* 3(No.5), 41-47 (2000)
3. D a m g o v, V.. Modeling Systems and Mechanisms of Oscillation Excitation. *Earth, Moon and Planets* 61, 87-117 (1993)
4. D a m g o v, V. and I.Popov. Multiple Attractors in a Class of Dynamical Systems. *Comptes Rendus de la Academy Bulgare des Science* 52(No.5-6), 31-34 (1999)
5. D a m g o v, V. and P.Georgiev. General Conditions for Resonance Oscillations Excitation Under the Action of External Nonlinear Force. *Comptes Rendus de la Academy Bulgare des Science* 52(No.9-10), 22-25 (1999)
6. B o g o l j u b o v, N. and Y.A. Mitropolsky. *Asimptotical Methods in the Theory of Nonlinear Oscillations*. Nauka Publ., Moskow (1916)

7. D a m g o v, V.. *Nonlinear and Parametric Phenomena in Radiophysical Systems*. "Prof. M.Drinov" Academic Publ. House, Sofia (2000)
8. E s c a n d e, D. Large-Scale Stochasticity in Hamilt.onian Systems. *Pliysica Scripta,* T2/1 (1982), 126-141
9. W i g g i n s, S. Introduction to Applied Nonlinear Dynamics and Chaos, Springer-Verlag, New York, Berlin, Heidelberg, London, Paris, Tokyo, Hong Kong, 1989
10. W i g g i n s, S. Global Bifurcations and Chaos, Springer-Verlag, New York, Berlin, Heidelberg, 1988

ОСЦИЛАЦИОННО-ВЪЛНОВ МОДЕЛ КАТО НЕХОМОГЕННО ВОДЕНА ДИНАМИЧНА СИСТЕМА

Владимир Дамгов , Николай Ерохин , ПламенТренчев

Резюме

Разгледан е обобщен модел на осцилатор, намиращ се под външно вълново въздействие. Показано е, че системи с различна физическа природа, обединявани от този модел, принадлежат към по-общия клас "кик-възбудими само-адаптивни динамични системи". Теоретичното разглеждане включва анализ в условията на големи и малки амплитуди, т.е. случаите на силна и слаба нелинейност на системата. Статията разглежда също наличието на така наречената подкова на Смейл в динамиката на частица, намираща се под въздействието на две вълни. Този проблем идва от физиката на плазмата, но диференциалните уравнения, разглеждани в статията, имат и множество други приложения.

Bulgarian Academy of Sciences. Space Research Institute.
Aerospace Research in Bulgaria. 19, 2005, Sofia

NON-DIFFUSIVE MECHANISM OF CHARGED PARTICLES ACCELERATION UNDER THE ACTION OF AN ELECTROSTATIC WAVES PACKAGE

Vladimir Damgov, Nikolay Erokhin**, N. Zol'nikova**, Plamen. Trenchev**

** Space Research Institute - Bulgarian Academy of Sciences*
*** Space Research Institute - Russian Academy of Sciences*

Abstract

A new non-diffusive mechanism of charged particles acceleration is considered. The latter is conditioned by the wave-particle interaction in the resonance of second order that corresponds to the nonlinear oscillator excitation by an external force. The calculations show that a leap of the accelerating particle can be observed in the process of the resonance interaction, from one potential well to another that moves with a greater velocity. A sequence of such leaps through out the separatrix leads to particles acceleration with multiple increasing of their kinetic energy. The mechanism of charged particles acceleration under consideration is realizing when the conditions are fulfilled as follows. For the charge that has been captured in the potential well of the wave package n-th harmonics with a frequency ω_n, wave vector κ_n and amplitude E_n, a resonance of the second order with (n+1)-th harmonics should be fulfilled. The harmonics phase velocity ω_n / κ_n is to increase with the increasing of n, i.e. $\omega_{n+1} / \kappa_{n+1} > \omega_n / \kappa_n$. The regions of the captured particles velocities must adjoin for neighboring harmonics. The waves amplitudes are sufficiently enough for nonlinear oscillator excitation and throwing it throughout the separatrix. In this way, a new mechanism has been found of non-diffusive charged particles acceleration by a package of electrostatic waves with small but finite amplitude. A procedure of parameters selection is formed for the sequence of harmonics in the package that take part in the charged particle acceleration process. The effect under consideration is of interest, particularly, for the problem of cosmic rays generation and interpretation of origin mechanisms of accelerated particles flows (of electrons and ions) that are observed in the space plasma.

1. Problem formulation and basic equations

Let us consider a charge interaction having a mass m with a package of electrostatic waves consisting $(n+1)$ modes with frequencies ω_n, wave vectors κ_n and amplitude E_n. Considering one-dimensional case, the equation of the charged particle motion can be presented in the form:

$$mx_{tt} = qE_o \sin(\kappa_o x - \omega_o t + \psi_o) + \sum_{n=1}^{N} E_n \sin(\kappa_n x - \omega_n t + \psi_n) \qquad (1)$$

where ψ_n is the wave phase, $\omega_n = \omega(\kappa_n)$ is determined by the dispersion equation. We assume that charge velocity x_t is close to the phase velocity ω_o / κ_o in the initial moment of time. For the numerical study it is suitable to pass over a counting system that moves with velocity of ω_o / κ_o and to introduce dimensionless time

$$x = \frac{\omega_o}{k_o} t + \frac{y}{k_o}, \quad \tau = \omega_{nonlin} t, \quad A_n = E_n / E_o$$

$$\omega_{nonlin} = (qk_o E_o / m)^{1/2}, \quad q_n = k_n / k_o, \quad \omega_{nonlin} = (k_o \omega_n - k_n \omega_o) / k_o \omega_{nonlin} \qquad (2)$$

where ω_{nonlin} is bounce-frequency of the oscillations that have been captured in the potential well. Varying the initial counting point of time we can make that $\psi_o \pi$. As a result, substituting (2) into Eq. (1) we obtain finally

$$\frac{d^2 y}{d\tau^2} + \sin y = \sum_{n=1}^{N} A_n \sin(q_n y - \Omega_n \tau + \Psi_n) \equiv f(y, \tau) \qquad (3)$$

Equation (3) describes the nonlinear oscillator motion in the potential well $U_o(y) = (1 - \cos y)$ when interacting with the force $f(y, \tau)$. If $f = 0$, the oscillator energy preserves, $\mathcal{E} = 0.5 y_\tau^2 + U(y)$, and $0 \le \mathcal{E} < 2$, $|y_\tau| < 2$ corresponds to the particle that has been captured in the well $-\pi < y < \pi$. The spectrum $E_n(k_n)$ that is considered to be given determines the wave amplitudes.

Below, a mechanism of charged particle interaction with waves package will be considered as follows. At the first stage, the force $f_1 \equiv A_1 \sin(q_1 y - \Omega_1 \tau + \psi_1)$ swings the oscillator in the potential well $U_0(y)$ on the basis of the resonance of the second order, when $\Omega_2 \approx 2$. The later causes a transition throughout the separatrix $\varepsilon = 2$. Further on, the charge is

captured by the wave $E_1 \sin(q_1 x - \omega_1 \tau + \psi_1)$. At the second stage, the force $f_2 \equiv A_2 \sin(q_2 y - \Omega_2 \tau + \psi_2)$ accelerates the charge due to the resonance of the second order at the frequency Ω_2. The charge makes a transition throughout the separatrix into the potential well U_1, that is created by a wave moving with a phase velocity $v_\phi^{(1)} = \omega_1 / k_1$. There upon a capture by the wave 2 occurs (the wave 2 moves with phase velocity of ω_2 / k_2), and so on, up to the phase velocity of $v_\phi^{(N)} = \omega_N / k_N$. Thus, we consider a package in which the phase velocity $v_\phi^{(N)}$ increases when the number n increases while the charged particle acceleration by velocity is $\Delta v_f = (\omega_N / k_N) - (\omega_0 / k_0)$. In the case of electronic Lengmuir's waves in the plasma without magnetic field, the dispersion equation has the form: $\omega^2(k) = \omega^2{}_{pe}(1 + 3k^2 r_D^2)$, where ω_{pe} is the electron Lengmuir's frequency, $r_D = (T_e / m_e \omega^2{}_{pe})^{1/2}$ is the Debay radius. Hence, for the elementary Lengmuir waves the phase velocity increases when the vector k decreases. Taking into account this circumstance, further on we can, e.g., assume that $k_N = k_o + n\Delta k$, where $\Delta k = (k_N - k_0)/n < 0$. Then, $q_N = 1 + n\Delta q$, $\Delta q = (q_N - 1)/N$.

As we have already mentioned above, in the mechanism of charge acceleration under consideration the charge energy increasing is due: *i*) to the growing of its oscillations in the potential well U_N on the account of second order resonance with the mode (N+1), *ii*) to the transition throughout the separatrix and *iii*) to the capture into the potential well U_{N+1}. Further on the process repeats. For securing the process to be uninterrupted and cyclic it is necessary to have mating of the particles velocities intervals that are captured by neighbouring modes n and $n+1$.The necessary condition could be obtained by the way as follows. Let ε_n are some numbers from the interval (0,1), i.e. $0 < \varepsilon_n < 1$. The particle that has been captured in the potential well of the mode n, when crossing the separatrix in the well U_n will have a velocity $(\Omega_n / q_n) + 2(A_n / q_n)^{1/2}$. This velocity should correspond to the particle velocity that has been captured by the ($n+1$) mode $(\Omega_{n+1} / q_{n+1}) - 2\varepsilon_{n+1}(A_{n+1} / q_{n+1})^{1/2}$. Hence, when choosing the mode parameters it is necessary to have in mind the condition of the mating of the

captured charges velocities intervals,

$$\left(\Omega_n / q_n\right)+2\left(A_n / q_n\right)^{1/2} > \left(\Omega_{n+1} / q_{n+1}\right)-2\varepsilon_{n+1}\left(A_{n+1} / q_{n+1}\right)^{1/2} \quad (4)$$

Even, for exciting the particles oscillations by $(n+1)$ mode – particles that has been captured into a potential well U_n - it is necessary to ensure a second – order resonance, i.e. to satisfy the condition

$$\Omega_{n+1} - \Omega_n \frac{q_{n+1}}{q_n} \le 2\sqrt{q_n A_n} \quad (5)$$

at the frequency of the $(n+1)$ mode in a system of coordinates that moves with phase velocity Ω_n / q_n and also at the bounce – frequency of particles oscillations captured in the potential well U_n.

Besides the conditions (4) and (5) let determine the amplitude A_n choice. First of all we notify that usually the amplitudes $E(k)$ change considerably at $\Delta k \sim k$ for an sufficiently wide wave spectrum. In the case under consideration $\Delta n \sim 1$ is connected with a lower change of the wave vector $\Delta k << k$. That is why A_n could be regarded to be a slowly changing functions of the mode number n, i.e. $\left|A_{n+1} - A_n\right| << \left|A_n\right|$. Depending on the conditions of wave package generation, A_n could decrease as well as increase when increasing n. Here we will study the case of A_n decreasing when increasing n. The rate of A_n decreasing is determined by the number of modes that take part in the charged particles acceleration as the minimum A_n will not ensure yet enough exciting of the nonlinear oscillator in the condition of the second order resonance.

The last question left is the choice of the mode phases Ψ_n. Below, they have been chosen by an experimental way from the interval $(-\pi, \pi)$. But we should notice that, accordingly to the calculations made for each mode n, there exist several subintervals of favorable phase Ψ_n that further charges acceleration.

2. Numerical study of charge acceleration by wave packages

In the course of numerical study of Eq.(3), the starting point was the consideration of the influence on the oscillator $y(\tau)$ with two modes $n = 1$ and $n = 2$ having parameters as follows:

$$\begin{aligned} &A_1 = 0.8, \quad q_1 = 0.85, \quad \Omega_1 = 1.87, \quad \Psi_1 = \pi/4, \quad \Omega_1 / q_1 \approx 2.2 \\ &A_2 = 0.6, \quad q_2 = 0.65, \quad \Omega_2 = 3.08, \quad \Psi_2 = \pi/2, \quad \Omega_2 / q_2 \approx 4.738 \end{aligned} \quad (6)$$

The initial conditions for the oscillator y have been taken to be

$y(0) = \dot{y}(0) = 0$. The calculations have showed that the mode 1, exciting the oscillator due to the second order resonance, throws it away from the potential well U_o. We have an analytical approximation for the average position $\langle y(\tau) \rangle$ in the time period $\tau \leq 380$ presented in the form: $\langle y(\tau) \rangle \cong 722 + 2.2(\tau - 342)$. This corresponds to the capture of the particle by the mode 1, i.e. into the potential well $U_1(y, \tau)$. Further on, the particle is captured by the mode 2 and the averaged by the fast oscillations charge position is described by an approximation as follows: $\langle y(\tau) \rangle \cong 703.25 + 4.7384(\tau - 356)$, where $\tau \in (380, 1700)$.

Taking into account the dispersion, in the onset of the mentioned interval by τ it was $|(y(\tau) - < y(\tau) >| \leq 0.4$ while by the end $\tau \sim 1700$ the oscillation amplitude in the potential well U_2 was decreased down to the level $|(y - < y >| \leq 0.26$.

Afterwards, taking into account the mode 3, the Eq.(3) became to be characterized with parameters

$A_3 = 0.5, \quad q_3 = 0.55, \quad \Omega_3 = 3.855, \quad \Psi_3 = 23\pi/80, \quad \Omega_3 / q_3 \approx 7.009$.

Parameters (6) have been used for the modes 1 and 2. The calculations have confirmed the acceleration scenario presented above: gaining energy in the potential wells U_o, U_1, U_2, thereafter charge is captured by the mode 3. For $\tau > 936$ its average position can be determined by an approximation as follows: $\langle y(\tau) \rangle \cong 2026.23 + 7.009(\tau - 947)$. At $\tau > 1274$ the amplitude of frequency deviation in the potential well, created by the mode 3, is not large: $|(y(\tau) - < y(\tau) >| \leq 0.5$. The diagram presented in Fig. 1 illustrates the charge position $y(\tau)$ when acting with three modes having parameters indicated above and at the interval $\tau < 2600$. The character of charge oscillations after its caption by the mode 3 is shown in Fig 2. The phase plane (y, p), where $p = \frac{dy}{d\tau}$, is presented in Fig. 3 for the interval $\tau < 200$ and in the Fig .4 – for the end of the calculations interval $\tau \in (1700, 2000)$.

The method of wave parameters selection that has been described above convincingly demonstrates the possibility of increasing of the mode number that take part in the process of charged particles acceleration and furthers increasing of accclerated charges energy. In the following paper we intend to analyze a non-diffusive acceleration by a package of ten modes.

3. Conclusion

The results of the analysis presented can be summarized as follows. A mechanism has been proposed of non-diffusive charged particles acceleration with a package of electrostatic waves. The mechanism is caused by a process of growing oscillations of the particle that has been captured into the potential well. The latter is due to the second order resonance at the neighbor mode that has a larger phase velocity with a transition throughout the separatrix, and particle capturing by another wave. The process described repeats cyclicly so as the consequence of resonance interactions to correspond to the ever increasing waves phase velocities. A method is formulated of selecting parameters of the wave sequence that realizes the acceleration mechanism described above. Supporting numerical calculations have been made. The developed method for analysis allows adding by a simple enough way new modes to the rest and in this way – increasing the charged particles energy. For the mechanism under consideration the nonlinearity of dispersion equation $\omega(k)$ is of a principle importance.

$$\frac{d^2}{dt^2}y(t) + \sin(y(t)) + b\cdot\frac{d}{dt}y(t) = \left(0.1 + \alpha\cdot\frac{t}{\beta + t}\right)\cdot\sin\left[k\cdot y(t) - \left(\Omega - 0.07\cdot\frac{t}{100 + t}\right)\cdot t + \phi\right]$$

$\phi := \frac{\pi}{10}$ $A := 0.1$ $k := 0.6$ $\Omega := 1.98$ $b := 0.005$ $\alpha := 0.5$ $\beta := 100$ $y(0) = 0$ $y'(0) = 0$

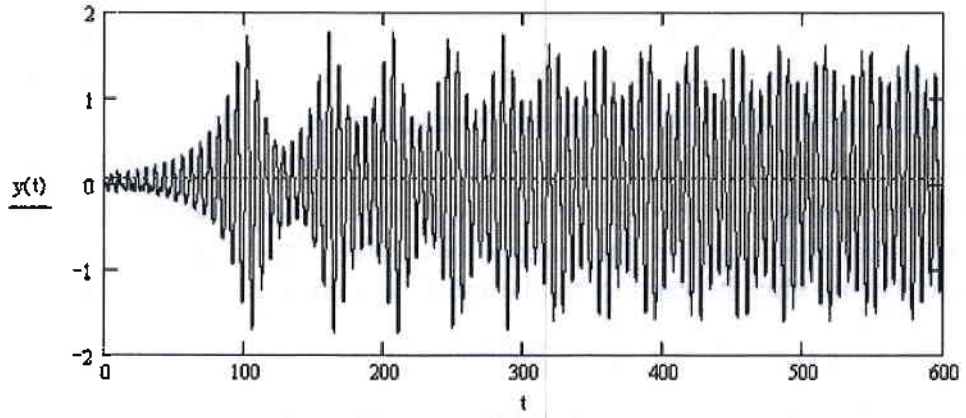

Fig. 1

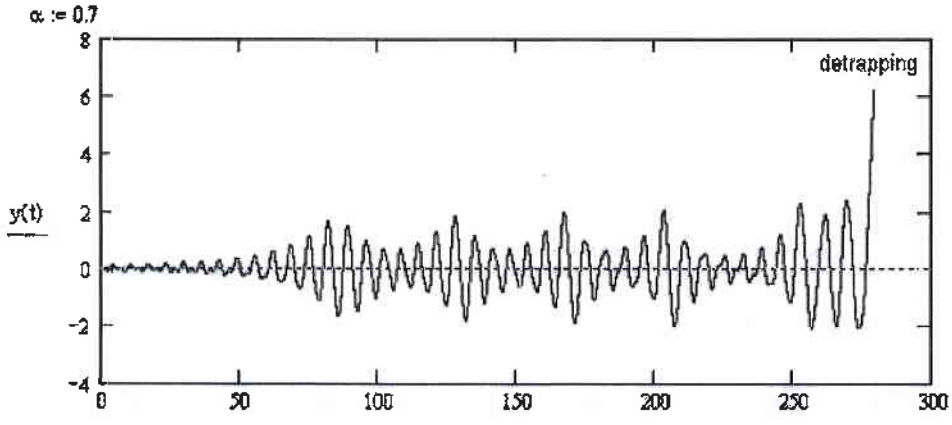

Fig. 2

$$\phi := \frac{\pi}{10} \quad A := 0.1 \quad k := 0.6 \quad \Omega := 2 \quad b := 0.01 \quad \alpha := 0.3 \quad \beta := 130 \quad y(0) = 0 \quad y'(0) = 0$$

$$\frac{d^2}{dt^2}y(t) + \sin(y(t)) + b\cdot\frac{d}{dt}y(t) = \left(0.1 + \alpha\cdot\frac{t}{\beta + t}\right)\cdot\sin\left[k\cdot y(t) - \left(\Omega - 0.11\cdot\frac{t}{100 + t}\right)\cdot t + \phi\right]$$

$$p(t) := \frac{d}{dt}y(t)$$

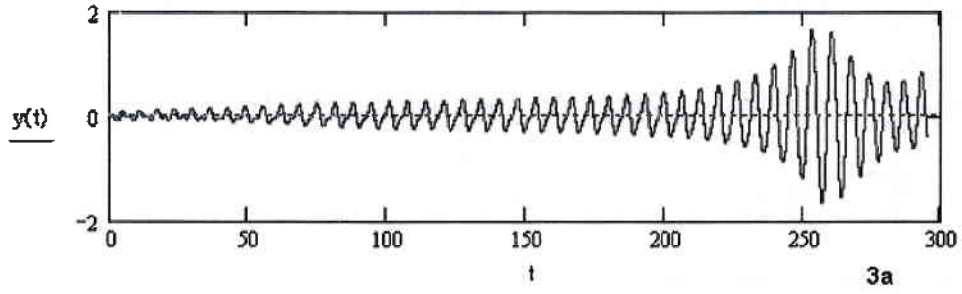

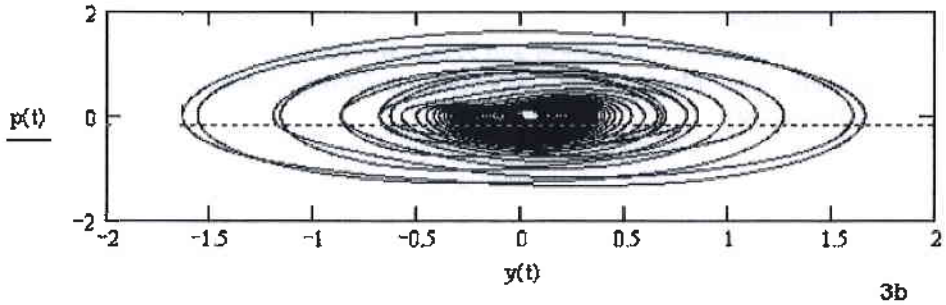

Fig. 3

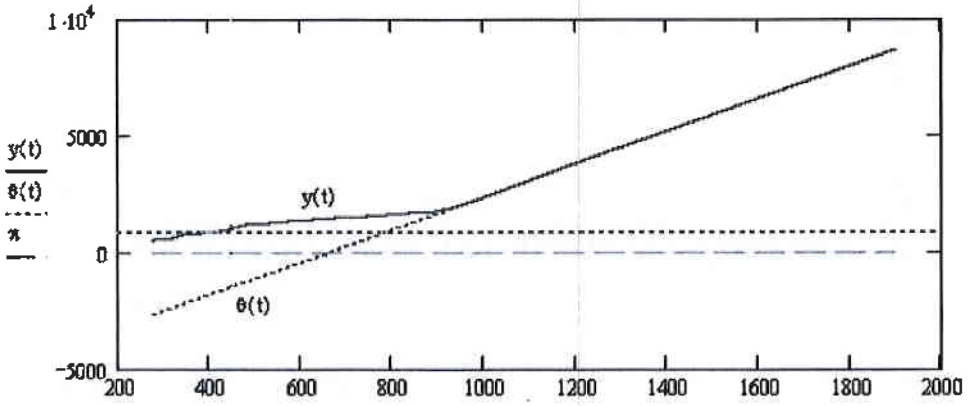

Fig. 4

Particle acceleration by waves

$$\frac{d^2}{dt^2}y(t) + \sin(y(t)) + b\cdot\frac{d}{dt}y(t) = A2\cdot\sin(k2\cdot y(t) - \Omega2\cdot t + \phi2) + A3\cdot\sin(k3\cdot y(t) - \Omega3\cdot t + \phi3) + A4\cdot\sin(k4\cdot y(t) - \Omega4\cdot t + \phi4)$$

$\phi2 := \frac{5\pi}{20}$ $A2 := 0.8$ $k2 := 0.85$ $\Omega2 := 1.87$ $\frac{\Omega2}{k2} = 2.2$ $b := 0.01$

$\phi3 := \frac{5\pi}{10}$ $A3 := 0.6$ $k3 := 0.65$ $\Omega3 := 3.08$ $\frac{\Omega3}{k3} = 4.738$

$\phi4 := \frac{23\cdot\pi}{80}$ $A4 := 0.5$ $k4 := 0.55$ $\Omega4 := 3.855$ $\frac{\Omega4}{k4} = 7.009$

$\theta(t) := 2026.23 + 7.009\cdot(t - 947)$

References

1. V. N. D a m g o v. Nonlinear and Parametric Phenomena in Radiophysical Systems. "Prof. Marin Drinov" Academic Publishing House, Sofia 2000, 450 p. (in Bulgarian).

НЕДИФУЗИОНЕН МЕХАНИЗЪМ НА УСКОРЯВАНЕ НА ЗАРЕДЕНИ ЧАСТИЦИ ПОД ДЕЙСТВИЕ НА ЕЛЕКТРОСТАТИЧЕН ВЪЛНОВ ПАКЕТ

Владимир Дамгов, Николай Ерохин, Н. Зольникова, Пламен Тренчев

Резюме

Разгледан е нов механизъм за недифузионно ускоряване на заредени частици от пакет електростатични вълни, обусловен от взаимодействието вълна-частица при резонанс от втори ред, съответстващ на възбуждането на нелинейния осцилатор от външна сила. С числени пресмятания е показано, че в процеса на резонансното взаимодействие се получава прехвърляне на ускоряваната частица от една потенциална яма в друга, движеща се с по-голяма скорост. Поредицата от такива прехвърляния през сепаратрисата допринася за ускоряването на зарядите с многократно увеличение на тяхната кинетична енергия. Този механизъм за ускоряване на заредените частици се реализира при изпълнение на следните условия. Ако зарядът е прихванат в потенциалната яма на n - ната хармонична от вълновия пакет с честота ω_n, вълнов вектор κ_n и амплитуда E_n, следва да се реализира резонанс от втори ред с *(n+1) -ва* хармонична. Фазовата скорост на хармоничната ω_n/k_n следва да нараства с увеличението на и, т.е. $\omega_{n+1}/\kappa_{n+1} > \omega_n/k_n$. За съседните хармонични обхватите на скоростите на прихванатите частици трябва частично да се препокриват. Амплитудите на вълните следва да са достатъчни за възбуждане на осцилатора и прехвърляне на заредената частица през сепаратрисата. Подробно е описан този нов механизъм на недифузионно ускоряване на заряди от пакети електростатични вълни с малка, но крайна амплитуда. Формулирана е процедура за отбор на параметрите за редицата от хармонични в пакета, участващи при ускоряването на заредените частици. Даденият ефект представлява интерес, в частност, при решаване на проблема за генерацията на космически лъчи и при интерпретацията на механизмите на произход на потоци ускорени частици (електрони и йони), наблюдавани в космическата плазма.

Bulgarian Academy of Sciences. Space Research Institute.
Aerospace Research in Bulgaria. 19, 2005, Sofia

MODEL OF RISK ASSESSMENT UNDER BALLISTIC STATISTICAL TESTS

Ivan Gabrovski, Juliana Karakaneva

Defence Advanced Research Institute
"Rakovski" Defence and Staff College

Abstract

The material presents the application of a mathematical method for risk assessment under statistical determination of the ballistic limits of the protection equipment. The authors have implemented a mathematical model based on Pierson's criteria. The software accomplishment of the model allows to evaluate the V50 indicator and to assess the statistical hypothesis' reliability. The results supply the specialists with information about the interval valuations of the probability determined during the testing process.

Introduction

Creating effective personal protection tools against ballistic threats is an important task because of human life value. Work in this area is ongoing, performed by both the manufacturers of body armour and the researchers who provide scientifically-grounded solutions for individual armour quality assessment.

Accounting for the fact that there is no tool ensuring 100 % protection, conventional approaches aim to provide probabilistic estimations of life-important organs' protection, evaluating risk degree.

In the military, the *V50* ballistic test is used, which is the internationally recognised standard to assess the fragmentation resistance of personal protection, particularly hard armour, helmet, and vest. The *V50* testing identifies experimentally the velocity at which a bullet has 50 percent chance of penetrating the test object.

The *V50* ballistic limit velocity for material is defined as the velocity at which the probability of penetrating the chosen projectiles is exactly 0.5 (STANAG 2920[1]).

Using the Up and Down firing method, the first round shall be loaded with the amount of propellant calculated to give a projectile a velocity equivalent to the estimated *V50* ballistic limit for armour.

After a number of projectile have been fired, *V50* is calculated as the average of the velocities recorded for six fair impacts consisting of the three lowest velocities for complete penetration and the three highest velocities for partial penetration, provided the spread is not greater than 40 m/s.

Many body armour manufacturers use a modified form of the military *V50* testing as a design tool to develop and assess new body armour products. This test identified the velocity at which specific projectile has 50-percent chance of penetrating the armour which is being tested.

The *V50* ballistic limit testing allows producers to evaluate various designs against one another to optimize their characteristics for a specific type of body armour. A trend has emerged in which manufacturers publish test data and also put *V50* test information on the labels of some of their body armour.

The *V50* ballistic limit testing is a useful and informative statistical tool to evaluate certain armour characteristics at the armour's design phase, and to evaluate armour degradation over time.

Formulation of the research

Determining the probability characteristics of personal protection means calls for elaboration of research methodology to raise information reliability. Moreover, it is necessary to choose suitable methods for data processing to allow evaluate the risk level of the taken decisions.

Except for *V50,* the following characteristics of body armour are used in practice:

- V_{np} ballistic limit - the velocity under which a bullet definitely (100 %) doesn't penetrate the test object;
- V_p ballistic limit - the velocity over which a bullet definitely (100 %) penetrates the test object.

The above characteristics are determined by the experiment of firing according to the "Up-Down" method. This method involves a set of experiments at which the velocity is decreased upon penetrating the test object and alternatively - the velocity is increased upon non-penetrating the test object. The attempts are made within a bracket of velocity interval covering the three areas – area of non-penetrating (*np*), area of penetrating (*p*) and area of mixed results.

In the introduction we examined the model of *V50* determining, according to USA standard. In [2], the authors show a probability-statistical

model based on the frequencies of penetrating and non-penetrating attempts, and their distribution depending on velocity.

The initial data are several pairs of firing velocities and obtained results for (*np*) and (*p*) values. We evaluate the cumulative frequencies:

$m_1, m_2, m_3, ..., m_n,$

relevant to the event "non-penetrating" at velocities greater than respectively:

$v_1, v_2, v_3, \dots, v_n,$

where v_i , $i = 1, ...,n$ are the middle points of equal-width velocity range subintervals during the experiment. This range is determined according to the above-described approach.

By analogy, the cumulative frequencies are evaluated:

$k_1, k_2, k_3, ..., k_n,$

relevant to the event "penetrating" at velocities less than respectively:

$v_1, v_2, v_3, \dots, v_n.$

For statistics: M = $\{ m_1, m_2, m_3, ..., m_n \}$ and K = $\{ k_1, k_2, k_3, ..., k_n \}$, we define the smoothed probability distributions, respectively $P_m(x)$ and $P_k(x)$, corresponding to normal distribution. The probability $P_m(x)$ is related with the "nonpenetrating" event when the velocities $\xi \geq x$, and the probability $P_k(x)$ is related with the "penetrating" event when the velocities $\xi \leq x$.

Thereby *V50* is defined as the value ***x***, for which:

$P_m(x) = P_k(x)$.

Under the above-formulated conditions, the authors develop the probability model and determine the approximated probability distributions [3]. Based on data from real experiments they evaluate quintiles through linear regression equations and draw up the distribution image for $P_m(x)$ and $P_k(x)$ within the range of the velocity ***v***.

Determination of risk level under the probabilistic-statistical estimations

The previous research continues in this paper with the objective to verify the statistical hypothesis for conforming with the normal distribution

law after the Pearson's criterion - χ^2 and determining the confidence intervals of the penetration probability.

A Basic Statistical Method in Hypothesis Testing

The verification of the hypothesis is made separately for the cases of non-penetrating and penetrating firing. Below is given the method which describes the first case.

We evaluate the frequencies of non-penetrating attempts:

$f_i = m_i - m_{i-1}$ за $i = 1,2,...,n$, where $m_0 = 0$.

According to the probabilistic model, the next estimations are the mean x and variance s of velocity, concerning the event "non-penetrating":

$$\bar{x} = \frac{1}{n}\sum_{i=1}^{n} v_i f_i, \qquad s^2 = \frac{1}{n-1}\sum_{i=1}^{n} f_i (v_i - \bar{x})^2 .$$

The theoretical probabilities $p_1, p_2, p_3, ..., p_n$ of random variables

$$t_i = \frac{v_i - \bar{x}}{s}$$

are $p_i = |F(t_i) - F(t_{i-1})|$ for $i = 1,2,3,...,n$ and $p_1 = F(t_1)$.

The statistics χ^2:

$$\chi^2 = \sum_{i=1}^{n} \frac{r_i^2}{r p_i} - r ,$$

(1)

where $r_i / r = f_i$ and $r = \sum_{i=1}^{n} r_i$,

features Pearson distribution:

$$P(\chi^2 \geq \chi_0^2) = \frac{1}{2^{\frac{n-1}{2}} \Gamma(\frac{n-1}{2})} \int_{x_0^2}^{\infty} x^{\frac{n-1}{2}-1} e^{-\frac{x}{2}} dx ,$$

(2)

and $\Gamma(n) = \int e^{-z} z^{n-1} dz$

is a well known *gamma* function.

This test based on statistics χ^2 is called chi-square test. The hypothesis' examination comprises the following steps:

- Choosing level of importance $q\%$, for example $q = 5$, and following (1) evaluating χ_q^2, such that $P(\chi^2 > \chi_q^2) = \frac{q}{100}$;
- Calculating the value of χ^2 according to (2);
- There are two cases for χ^2:

1) $\chi^2 > \chi_q^2$ i.e. we get into the critical region and therefore, the non-conformity between the observed results and theoretical distribution data is considerable, so, the hypothesis is rejected, or

2) $\chi^2 \le \chi_q^2$ i.e. the non-conformity is not considerable and the hypothesis is accepted.

Determination of the confidence intervals of unknown probability

The determination of the confidence interval of unknown probability concerning the event "non-penetrating", for example at the interval $(v_i - \frac{h}{2}, v_i + \frac{h}{2})$ for r_i "non-penetrating" firings and n_i common implemented shots during this interval, under confidence level of at least $1-2\alpha$, is carried out as follows:

- Evaluating the root $\tilde{p}_{r_i\alpha}$ of equation:

$S_{n_i r_i}(\tilde{p}_{r_i\alpha}) = \alpha$, where

$$S_{n_i r_i}(p) = \sum_{j=0}^{j=r_i} C_{n_i}^j p^j (1-p)^{n_i - 1} \text{ и } C_n^j = \frac{n!}{j!(n-j)!};$$

- Evaluatinge the root $p_{r_i\alpha}$ of equation:

$S'_{n_i r_i}(p_{r_i\alpha}) = \alpha$, where

$$S'_{n_i r_i}(p) = \sum_{j=r_i}^{j=n_i} C_{n_i}^j p^j (1-p)^{n_i - 1}.$$

Then the interval $p_{r_i\alpha} < p < \tilde{p}_{r_i\alpha}$ covers the unknown probability p of the event "non-penetrating" within the interval $(v_i - \frac{h}{2}, v_i + \frac{h}{2})$ under confidence level $1-2\alpha$.

Software instrument

Characteristic of the application software

Based on the probabilistic statistical method, the authors coded a software application. It is a *Windows Forms* style application and works under *.NET Framework* (Fig. 1). The software environment is *MS Visual Studio .NET* and the language in which it was coded is *C#*. The application's implementation under *.NET* has several advantages compared to the old *Windows* style (COM) applications.

First, the whole information about the application and the components used by it is saved in configuration files. These files use *XML* syntax to save hierarchical data which makes them more flexible than the old *.ini* files.

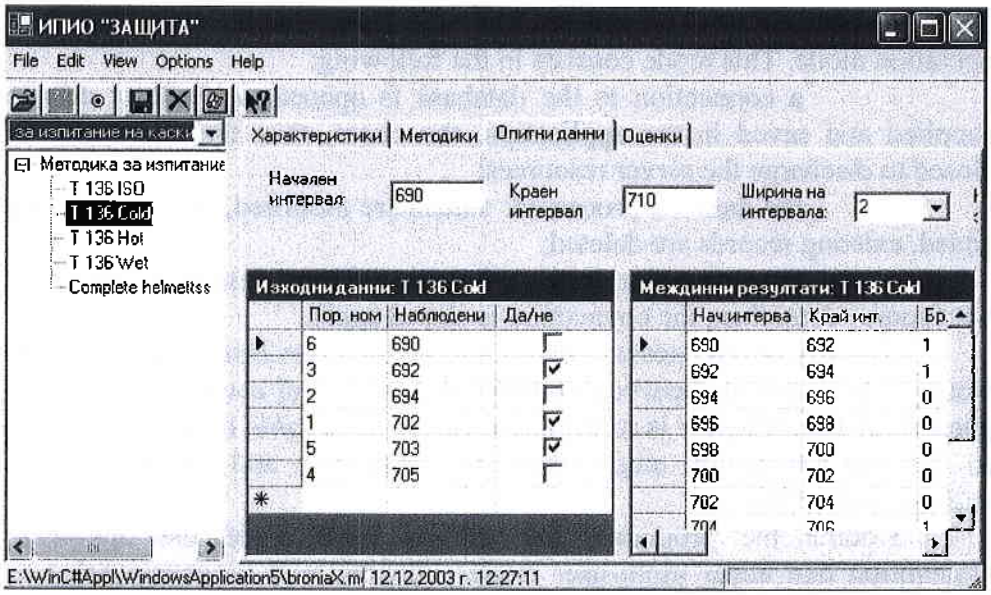

Fig. 1

The other advantage is the object-oriented approach. In contrast to *COM*, *.NET Framework* is designed under the inheritance concept. All objects of the *.NET Framework* form a single-root hierarchy, the class *System.Object* to which all other classes are successors. These classes ensure functionality in all possible areas, including user interface, data access, security, *Internet* programming, communications between devices, etc.

And third, *.NET* provides a solution for the version problem. The particular components of the application are saved in an application

directory, or in its sub-directory. Different applications can use different versions of the components because they are saved in different directories. Each component of the global cash is saved in a separate subdirectory and different versions of the same component can exist simultaneously on the same computer device. Each application coded under a given component version continues working correctly even when the user installs a new (or older) version of this component.

Working with database

All data of the estimation model are saved into a database, the *Microsoft Access.*

The *System.Data* classes build the part of the *.NET Framework* known as *ADO.NET* for working with the database (DB). *ADO.NET* use *.NET* controlled data providers. The application uses *read-only* data operation mode. This mode consists in the following:

- a connection to the database is opened, a block of data is supplied and saved in the application, the client, then the connection is closed to discharge the server resources;
- the data are processed: values are modified, new records are added, existing records are deleted;
- the connection is opened again and local data are harmonized with source data, then, the connection is closed again.

The key of data access is an object of the class *DataAdapter*, which works as a connector between *DataSet* and the actual source of data. The purpose of *DataAdapter* is to fill one or more *DataTable* objects with data, so that the application might close the connection and operate thereon without connection.

Coding the programs, the authors have made the optimistic assumption that under multi-user mode collisions will be occasional, i.e., most likely the application will work on the client workstation with client database. For the cases when the database is on the server and many users work with, ways to prevent collisions have been provided.

The program provides user interface to introduce data and functions, to process the results from experiments, and to present output results in the form of histograms and documents.

Besides the previous research of the authors, namely determining *V50* ballistic limits of body armour (Fig. 2), the software instrument presents specified-above characteristics. The results are evaluated based on the given algorithm and relevant program module. According to the above-

procedure, the calculations yield the values of χ^2 - crucial, χ^2 of "non-penetrating" and χ^2 of "penetrating' shots (Fig. 2). The output report shows whether the hypothesis is accepted or rejected (Fig. 3).

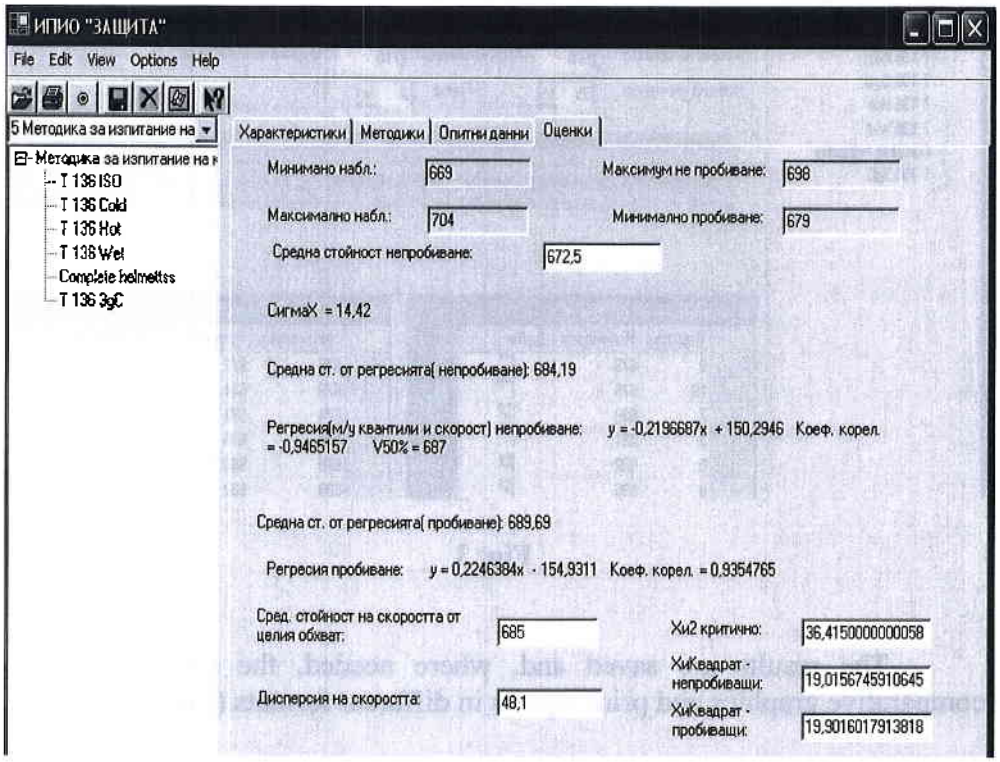

Fig. 2

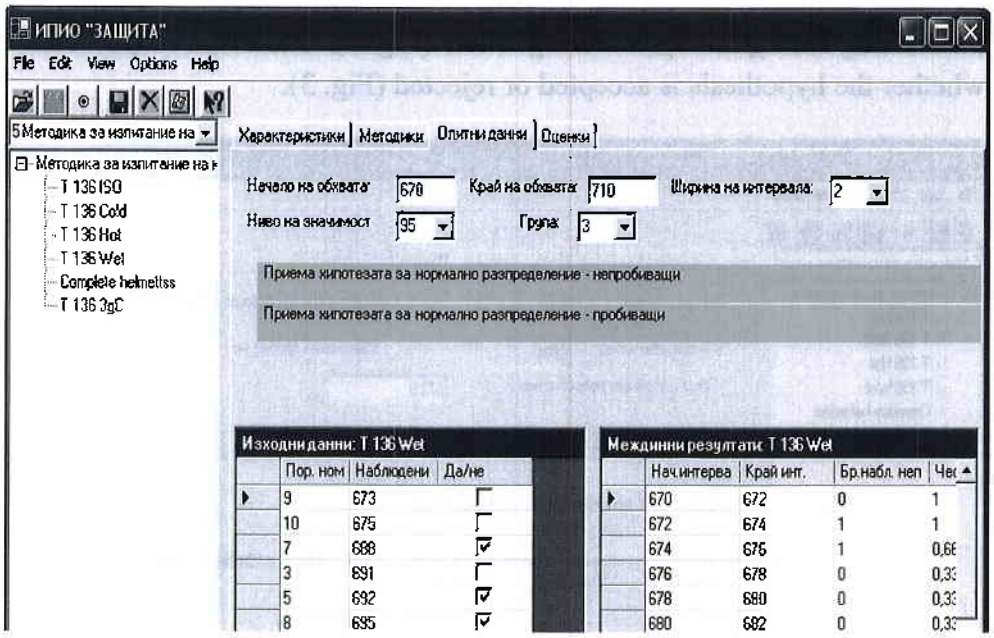

Fig. 3

The results are saved and, where needed, the user can obtain comparative graphics and print reports in different formats (Fig. 4).

Conclusions

The authors' efforts are focused on the creation of mathematical model and procedure to estimate the basic characteristics of body protection armours. The application of probabilistic-statistical approach provides to make much estimation based on real experiments with helmets and armoured vests. The developed software application is a very useful tool in this process. The obtained results conform to the theoretical hypothesis. This assumed approbation manner confirms the approach's correctness and validates the chosen method.

The presented product furnishes the responsible agency with an effective tool to estimate body armours characteristics during ballistic tests. Moreover, the software instrument, which is based on modern computer technology, can be used in the research and manufacture of new protection equipment.

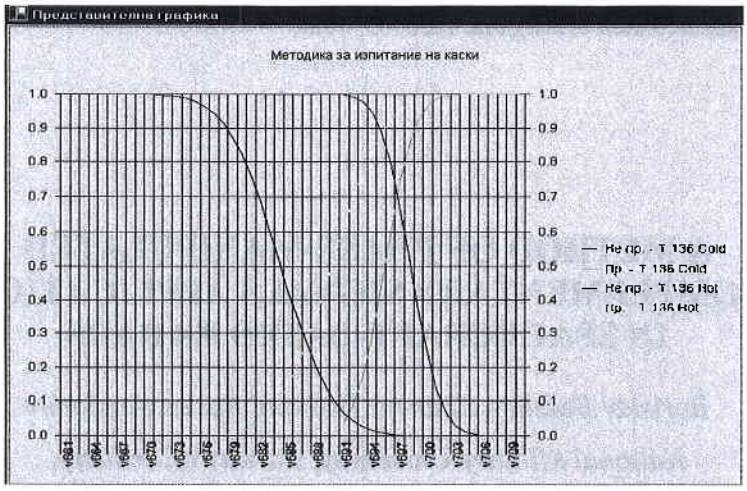

Fig.4

References

1. MILITARY STANDARD V50 BALISTIC TEST FOR ARMOR – STANAG 2920.
2. Габровски, И., Ю. Каракънева, Хр. Христов. Математически модел за определяне показателите на средствата за индивидуална балистична защита. Сборник доклади от Научната сесия на Шуменския университет, 2003. (in Bulgarian)
3. Крамер Г. Математические методы статистики. М., "МИР", 1975, (2-е изд). (in Russian)

МОДЕЛИРАНЕ НА ОЦЕНКАТА НА РИСКА ПРИ ОПРЕДЕЛЯНЕ НА БАЛИСТИЧНИТЕ ПОКАЗАТЕЛИ НА СРЕДСТВАТА ЗА ИНДИВИДУАЛНА ЗАЩИТА

Иван Габровски, Юлияна Каракънева

Резюме

В материала е представено приложението на математически модел за оценка на риска при статистическо определяне на балистичните граници на защитното оборудване. Авторите са създали математически модел на базата на критериите на Пиърсън. Софтуерната реализация на модела дава възможност да се изчисли показателят V50 и да се оцени надеждността на статистическата хипотеза. Резултатите дават на специалистите информация за оценката на интервалите на вероятността, определени в процеса на тестването.

Bulgarian Academy of Sciences. Space Research Institute.
Aerospace Research in Bulgaria. 19, 2005, Sofia

A METHOD OF PHASE-MANIPULATED COMPLEMENTARY SIGNALS APPLICATION IN SPACECRAFT-BASED RADARS

Borislav Bedzhev, Zhaneta Tasheva, Rosen Bogdanov

National Military University, Faculty of Artillery, Air-Defence and Communication and Information Systems

Abstract

The radar imagery, realized by means of synthetic aperture radars (SARs) is very important in the exploring of planet, satellite and comet surfaces. The most valuable feature of the autocorrelation function (ACF) of the SAR signals is the level of their side lobes, because they determine the dynamic diapason of the image and the possibility to discover small objects. With regard to this, our paper suggests a method for applying in spacecraft-based SARs the so named generalized complementary signals, which ACF does not have any side-lobes. It uses the polarization features of the electromagnetic waves.

Key Words: *Synthetic aperture radars, ideal autocorrelation function, generalized complementary signals.*

1. Introduction

The radar imagery is very important in the exploring of planet, satellite and comet surfaces [1, 2]. It may be sketched as follows. The transmitter of the spacecraft-based radar sends electromagnetic signals. The examined objects reflect the signals, producing so named echo-signals. They are the input to the radar receiver. Mostly, in order to maximize the ratio "signal/noise", the receiver is constructed as a filter, matched to the sent signals. In this case the receiver output is the autocorrelation function *(ACF)* of the sent signals. This is clarified on Fig. 1, where a radar signal is depicted (Fig. la). The duration of the signal is Γ, but it is separated in η sub-signals (or "elementary signals") with duration r_0 (i.e. $n = T / r_0$) and different carrier frequency. This technique is named "discrete frequency shift-keying" *(DFSK)*. It allows obtaining a different echo-signal from every

"reflected point" of the object. Commonly, the receiver output, produced of a single point echo, is characterized by a main peak *V* and a sequence of side-lobes with maximal amplitude *Vmax,* as shown on Fig. lb. At the end, the radar receiver output signals are sampled and processed, which lead to extracting of the object image [3].

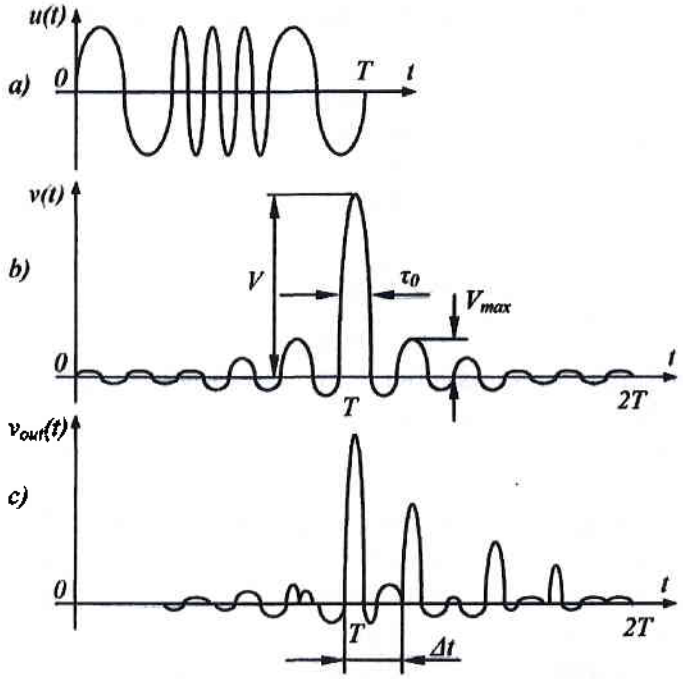

Fig. 1 Processing of radar signals

In general, the above described technique of complex radar signals usage guarantees simultaneously large performance range (provided by the aggregated power of elementary signals) and high distance resolution (defined by *TQ)* of the spacecraft-based synthetic aperture radars *(SARs).*

Unfortunately, the real objects comprise more than one reflected points. As a result, the echo-signals of all reflected points interfere, as depicted in Fig. lc. In this situation is hard to obtain a detailed object image, because the side-lobes of more power signals mask the main peaks of the weak signals.

With regard to this, our paper aims to suggest a method for applying of so named generalized complementary signals, which *ACF* does not have any side-lobes. It uses the polarization features of the electromagnetic waves.

2. A Method of Phase Manipulated Complementary Signals Applying in Spacecraft-based Radars

It is known [4] that discrete phase and frequency modulated signals may be presented as the real part of the complex-valued function:

$$(1) \qquad V(t) = \sum_{j=1}^{n} \{U_j . \exp(i\theta_j) . \exp[2\pi i (f_0 + f_j)t]\} u_0(t - j\tau_0),$$

where / = v-T; *Uj* is the amplitude of the j* elementary impulse y=1,2,...,«; $/_0$ is the carrier frequency; {/ь/2,—,/«} are real time functions, which expresses the frequency modulation; *{Θ j; 0 < θ j < 2π; j* = 1,2, ...*n]* is the set of numbers, describing the phase modulation and:

$$(2) \qquad u_0(t) = \begin{cases} 1, \ if \ \ 0 \le t \le \tau_0 \\ 0, \ if \ \ t < 0, \ or \ \ t > \tau_0 \end{cases}.$$

To maximize the transmitter efficiency and to simplify the practical realization of the process of signal receiving, the so-named uniform signals with r_0 = *const; Uj* = *const; j* = 1,2,..., *n;; 0j* e {(2л/) *Im; 1* = 0,1,...,*m* - 1}are most widely applied.

In this case and if only discrete phase shift keying *(DPSK)* is applied, the signal is named "discrete phase manipulated *(PM)* signal". It can be comprehensively described by the sequence $\{\zeta(\theta')\}^{n}_{=1}$ *of* normalized complex amplitudes of elementary signals [41:

$$(3) \qquad \zeta(j) = \exp(i\theta_j); \ \ \zeta(j) \in \{\exp(2\pi i l / m); l = 0,1,..., m-1\}.$$

As above mentioned, the signals, which *ACF* has close-to-zero level of the side-lobes, are the most attractive for implementation in spacecraft based *SARs.* With regard, in the rest part of the paper our attention shall be focused on the so-named generalized complementary signals, which *ACF* is free of any side-lobes. It is known that a single radar signal does not have non-periodical *ACF* with zero level of the side-lobes. Moreover, the classes of single uniform discrete radar signals with small level of their side-lobes seem to be very rare. Due to this reason, Golay introduced [5] the so-named complementary series (or signals (CSs)). They are a pair of two uniform binary phase manipulated signals, which aggregated non-periodical *ACF* is similar to a delta pulse.

It is necessary to emphasize, that Golay's definition of *CSs* is not useful in some important cases. This situation has motivated some theoreticians to extend the classical definition as follows [6, 7,8].

Definition 1: *The set of ρ sequences (PM signals), which elements are complex numbers, belonging to the multiplicative group of the m-th (m>2) roots of unity:*

$$(4)\qquad \{A_1 = \{\xi_1(j)\}_{j=1}^{n_1}; A_2 = \{\xi_2(j)\}_{j=1}^{n_2}; \ldots; A_p = \{\xi_p(j)\}_{j=1}^{n_p}\};$$
$$\xi_k(j) \in \{\exp(2\pi i l / m_k); l = 0,1,\ldots, m_k - 1\}; k = 1,2,\ldots, p.$$

are a set of generalized complementary signals (GCCs) if and only if their aggregated ACF has an ideal shape, similar to delta impulse:

$$(5)\qquad R_c(r) = \sum_{k=1}^{p} R_{A_k}(r) = \begin{cases} n = n_1 + n_2 + \ldots + n_p; & \text{if } r = 0; \\ 0; & \text{if } r = 1,2,\ldots, \max\{n_k\}. \end{cases}$$

In (5) the non-periodical *ACF R^, (r)* are defined with the well known formula [4]:

$$(6)\qquad R_\zeta(r) = \begin{cases} \sum_{j=1}^{n-|r|} \zeta(j)\zeta^*(j+|r|), & -(n-1) \le r \le 0 \\ \sum_{j=1}^{n-r} \zeta^*(j)\zeta(j+k), & 0 \le r \le n-1. \end{cases}$$

Consequently, Golay's codes are a particular case of the GCCs, when $\rho = 2$, $m = 2$. The CCs and GCCs are unique among all *PM* signals with their following features:

- their aggregated *ACF* has an ideal shape, similar to a delta pulse;
- if a pair of GCCs, consisting η elements, is known, then it is easy to create an infinite set of pairs with unlimited code-length.

It ought to emphasize that the most type uniform *PM* signals with close to ideal *ACF* have limited code-length. For instance, Barker codes exist only for $\eta < 13$, if η is an odd integer.

With regard to the GCCs positive features, they are studied very intensively and a quick reference showed more than 200 conference reports and magazine articles, related to this theme, during the past ten years.

The natural question, which arises from Definition 1, is "How can be implemented the GCCs in a real communication system?". The most obvious answer is the usage of ρ different frequency carriers *ffr,k = l,2,...,p,* phase manipulated according to the sequences $A_k, k = l,2,\ldots,p$. Unfortunately, this is not the best approach, when the communication system is a spacecraft-based *SAR*. This conclusion will be clarified with following example. Suppose that spacecraft-based *SAR* exploits GCCs with $\rho = 2$ and the transmitter radiates simultaneously two uniform *PM* signals with carriers /j, /2, manipulated according to the sequences *A\, Aj* . As a result of so-named Doppler effect, the carriers f_e^

of echo-signals will be:

$$(7) \qquad f_{ek} = f_k \frac{1 - V_R/c}{1 + V_R/c} \approx f_k(1 - 2V_R/c), \; k = 1,2,$$

where $V\%$ is the radial velocity of the spacecraft relatively to the object and c is the velocity of the electromagnetic waves propagation. If the explored object is on the earth surface, then V_R must be at least 27 360 km/h. Then the difference $\Delta f = |f_{e1} - f_{e2}|$ will be too significant and it may lead to irreparable phase distortions between the components of the *GCCs*.

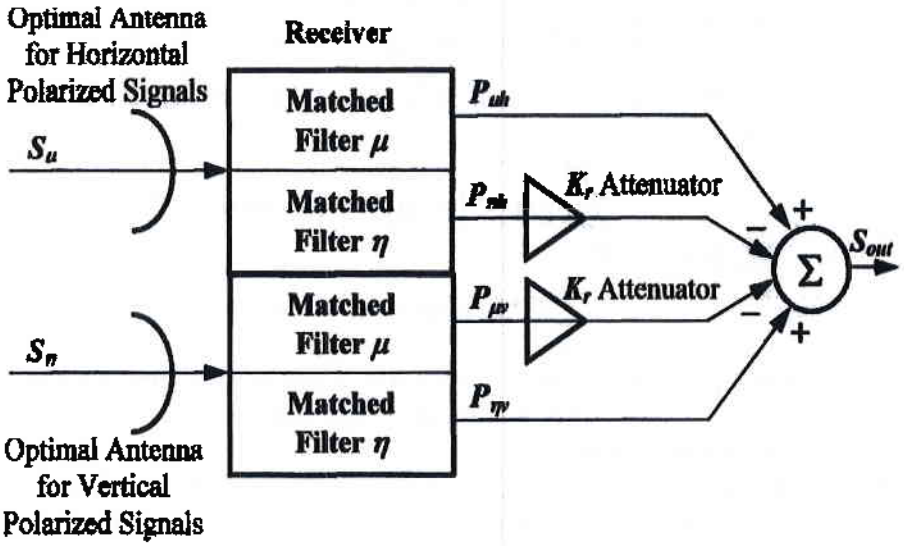

Fig. 2 Method of GCCs applying in spacecraft-based *SARs*

Due to above reason in the rest part of our report we shall prove a more appropriate approach to GCCs implementation in spacecraft-based *SARs*. Namely, we propose the two uniform *PM* signals, composing a pair of *GCCs,* to be transmitted on one frequency carrier f_0 simultaneously but by means of different types of polarization. Let the horizontal and the vertical polarized *PM* signals be described with the sequences *A - tPUyfji-i* $^{anc}*$ ^2 $^{=}$ *{n(j))* /=i respectively. Then the signals, reflected by an object point, will be $S^\wedge$, S_n respectively. The reflected signals are connected with transmitted signals by following matrix equation:

$$(8) \qquad \begin{Vmatrix} S_\mu \\ S_\eta \end{Vmatrix} = \begin{Vmatrix} D_{11} & D_{12} \\ D_{21} & D_{22} \end{Vmatrix} \begin{Vmatrix} A_1 \\ A_2 \end{Vmatrix}; \; \|D\| = \begin{Vmatrix} D_{11} & D_{12} \\ D_{21} & D_{22} \end{Vmatrix},$$

where the complex valued matrix |D| is the so-named "polarization matrix of the target scattering". Its entries depend on physical features of the

object, its orientation and position relatively to the radar and carrier frequency of transmitted signals. When these parameters are constant, then the entries of the matrix *WOW* are constants also and more over D17 = Z)?i.

Accounting that the size of a single reflected point is small, it may be concluded that Dj j $m\ D_{22}$ · Consequently, the matrix jJDjj can be presented in the form:

$$\|D\| = \begin{Vmatrix} k_1 & k_1 k_2 \\ k_1 k_2 & k_1 \end{Vmatrix}, \quad (9)$$

where $D_u = D_{22} = *$ ïí $\Phi\eta^{lk}\rangle = (\#21^{fk}\rangle = {}^{k}2$-

As above stated, the main obstacle for GCCs practical implementation by means of polarized electromagnetic waves is the fact that every echo-wave comprises the both horizontal and vertical polarized components. Due to this reason, we propose the method of signal processing, shown on Fig. 2. We shall explain it using the following notation. Let $\{\zeta\theta')\}^{\eta}_{=}]$ be the sequence of normalized complex amplitudes of elementary signals, composing an arbitrary complex signal. As mentioned, the result of processing of this signal by its matched filter will be the *ACF* of the signal. It may be presented with the following polynomial:

$$P(x) = F(x).F^*(x^{-1}). \quad (10)$$

Here:

$$F_\zeta(x) = \zeta(n).x^{n-1} + \zeta(n-1).x^{n-2} + ... + \zeta(2).x + \zeta(1), \quad (11)$$

$\{\zeta(j)\}_{j=1}^{n}$, $F_\zeta^*(x^{-1})$ is the so- named "Hall polynomial", corresponding to the sequence is the polynomial:

$$F_\zeta^*(x^{-1}) = \zeta^*(n).x^{-(n-1)} + \zeta^*(n-1).x^{-(n-2)} + ... + \zeta^*(1), \quad (12)$$

the coefficients of the polynomial *P(x)* are:

$p_k = R_c(k)$; κ = -(n-\)-(n-2),...-\,ЪX:.,n-2,n-\,

and the values *Rr(k)* of the *ACF* are computed according to (6).

Accounting the above notation, (8) and (9), the outputs of matched filters, shown on Fig. 2, may be expressed by following polynomials:

$$
\begin{aligned}
&P_{\mu h}(x) = k_1[F_\mu(x) + k_2.F_\eta(x)].F_\mu^*(x^{-1});\\
&P_{\eta h}(x) = k_1[F_\mu(x) + k_2.F_\eta(x)].[k_r F_\eta^*(x^{-1})];\\
&P_{\eta v}(x) = k_1[k_2.F_\mu(x) + F_\eta(x)].F_\eta^*(x^{-1});\\
&P_{\mu v}(x) = k_1[k_2.F_\mu(x) + F_\eta(x)].[k_r F_\mu^*(x^{-1})].
\end{aligned} \tag{13}
$$

In (13) k_r is a special coefficient, brought into the scheme by means of two directed attenuators. Now it is easy to see, that if attenuators on Fig.2 are regulated to obtain $k_r = k_2$, then:

$$
\begin{aligned}
S_{out}(x) &= P_{\mu h}(x) - P_{\eta h}(x) + P_{\eta v}(x) - P_{\mu v}(x) =\\
&= k_1\{[F_\mu(x)F_\mu^*(x^{-1}) + F_\eta(x)F_\mu^*(x^{-1})] -\\
&- k_2^2.[F_\mu(x)F_\mu^*(x^{-1}) + F_\eta(x)F_\mu^*(x^{-1})]\} = k_1.2n.(1 - k_2^2).
\end{aligned} \tag{14}
$$

Formula (14) shows that the method of *GCCs* usage, depicted on Fig. 2, preserves the cancellation of the *ACF* side-lobes, despite of the harmful presence of cross-reflected signals. The signal power losses depend on the relative coefficient of the cross-polarized reflection k_2.

3. Conclusions

The method of GCCs applying in spacecraft-based radars, presented above, preserves the positive features of the *GCCs,* especially the cancellation of the *ACF* side-lobes, despite of the harmful presence of cross-reflected signals. This result is reached by small losses of signal power, because mostly $k_2 < 20\%$ and hence $(1 - Ц) > 96\%$.

References

1. Гецов П., Жеков Ж., Мардиросян Г., Христов И., Ефективност на визирни оптични системи при наблюдение на отдалечени обекти при различна яркост на фона, Сб. научни трудове от НС на ВВУАПВО, ч. 2, Шумен, 1997г., с. 243-249.
2. Жеков Ж., Мардиросян Г., Христов И., Ижанова Д., Абсорбционни ултрафиолетовьш озонометр, Бълг. геофиз. сп. 1998, № 3-4, с. 50-54
3. Лазаров, А.Д., Радиовълни, антеннофидерни и микровълнови устройства, БСУ, 2003, www.bfu.bg.
4. Варакин Л. Е., Системи связи с шумоподобньши сигналами - М.: Радио и связь, 1985.-384 с.
5. Golay M. Y. E., Complementary series, IRE Trans, on Information Theory, 1961, vol. IT-7, №2, pp. 82-87

6. Tseng C. C, Liu S. L., Complementary sets of sequences, IEEE Trans, on Information Theory, 1972, vol. IT- 18, №5, p. 644 - 652
7. Игнатов В. В., Добровольский С. А., Гужва А. Ю., Матричные системы сигналов для использования я СНСНЗДДО С0МА. с?лек1ииси>ие. J.VVJ. J\~ У. t. 41-42
8. Frank L.R., Polyphase Complementary Codes, IEEE Trans, on Inform. Theory, 1980, vol. IT-26, № 6, pp. 641 – 647

МЕТОД ЗА ПРИЛАГАНЕ НА ФАЗОВО МАНИПУЛИРАНИ КОМПЛЕМЕНТАРНИ СИГНАЛИ В КОСМИЧЕСКИТЕ РАДИОЛОКАЦИОННИ СИСТЕМИ

Борислав Беджев, Жанета Ташева, Росен Богданов

Резюме

Получаването на радарни изображения на повърхността на планетите, спътниците и кометите е важен момент при тяхното изучаване. В този процес най-важното свойство на автокорелационната функция (АКФ) на радиолокационните сигнали е нивото на страничните листи на АКФ, защото то определя динамичния диапазон на изображението и възможността за откриване на малоразмерни обекти. По тази причина в статията се обосновава метод за използване на така наречените обобщени комплементарни сигнали (ОКС), чиято сумарна АКФ няма странични листи. Методът се характеризира с това, че запазва ценните свойства на ОКС въпреки ефекта на кръстосано поляризационно отражение на радарните сигнали. Този положителен резултат се постига технически просто и с минимални загуби на енергия на ехо-сигналите.

CHRONICLE

FIRST SCIENTIFIC CONFERENCE „SPACE, ECOLOGY, SAFETY"

Garo Mardirossian

Space Research Institute, Bulgarian Academy of Sciences

From 10 to 13 June, 2005, at the Rest House of the Bulgarian Academy of Sciences, Town of Varna, the First Scientific Conference with International Participation SPACE, ECOLOGY, SAFETY (SES'2005) took place. It was organized by the Space Research Institute of the BAS and the Bulgarian Astronautical Federation. Over 3 days, more than 90 scientific reports were presented, distributed into 9 sections – Space Physics and Astronomy, Aerospace Equipment and Technologies, Remote Sensing and Geoinformation Systems, Ecology and Risk Management, Space Materials Science, Space Medicine and Biology, Space and Warcraft, Space Education. A special session called „Small Balkan Satellite - BalkanSat" was organized. The presentation was both oral and poster.

The nearly one hundred participants came from various academic institutions, civil or military higher academic establishments, state or private firms. Young people were presented well too, in the face of post-graduate students from the SRI and other institutions.

About 15 scientists from abroad were also presented from England, Albania, Azerbaydzhan, Germany, Italy, and Macedonia. The presentation of Russian scientists was very impressive through Prof. Klimov and Prof. Erohin from the Space Research Institute of the Russian Academy of Sciences, Prof. Issaev from IZMIRAN etc.

In the end, a Round Table was organized, at which the participants hared their experience, opinions, and ideas on this topic which is coming to the fore not only in Bulgaria, but on a world scale, too.

All scientific reports were published in a two-volume Collection SES'2005, which was delivered to the participants at the time of registration for the Conference.

During the Conference, an exhibition entitled "Space" was organized presenting the pictures of Mr. Petar Stoyanov, Senior Researcher at the Space Research Institute.

The conductance of the Conference which marks the beginning of annual conferences on the topic may be qualified as very successful. Special appreciation is due to the Organization Committee with Honoured Chairman Acad. Nikola Sabotinov, Vice Cairman of the BAS, Chairman Prof. Petar Getsov, Director of the Space Research Institute, and all other organizers and participants.

The second Scientific Conference SPACE, ECOLOGY, SAFETY will take place in June 2006, again at the Rest House of the BAS in Varna,.

Information on the 35th COSPAR Scientific Assembly – Paris, France

Jordanka Semkova

Solar-Terrestrial Influences Laboratory, Bulgarian Academy of Sciences

The 35th COSPAR Scientific Assembly was held 18-25 July 2004, in Palais des Congres in Paris, France. The assembly was co-hosted by CNES (Centre National d'Etudes Spatiales –France) and by ESA (European Space Agency) and was organized with the support of the French Ministry of Research, the French Academy of Sciences, the Regional Council, the

City of Paris and the National Scientific Research Center (CNRS), as well as with the sponsorship of a number of industrial companies.

The Paris Assembly presented one of the richest scientific programmes in the field of space research, gathering more than 2,000 researchers.

The core scientific program, made up of 94 meetings spanning the range of topics addressed in COSPAR was exceptionally interesting, including 4,460 presentations, a far larger number than for any previous COSPAR Assembly.

The perfect organization of the Assembly and the conditions in the Palais des Congres in Paris – one of the most modern congress centers in the world, allowed the international space science community to exchange information on the latest progresses in space research, presented through the numerous oral and poster sessions, as well as the many informal discussions.

During the Assembly, a total of 33 papers with leading authors from the Bulgarian Academy of Sciences and Bulgarian universities were presented in almost all Scientific Commissions and in several panels. Most presentations – 23, came from the Solar-Terrestrial Influences Laboratory – BAS (STIL-BAS), 3 presentations were from leading authors from the Space Research Institute-BAS (SRI-BAS), 4 - from the Geophysical Institute-BAS. Six scientists from the STIL-BAS, attended the Assembly, four of them were partially supported by the organizers. Participating scientists presented altogether 10 own papers, as well as the papers of their colleagues, who were unable to attend the Assembly.

COSPAR 2004 included a new series of Panel Events at which a group of very prestigious speakers from all over the world gave participants a look at the future by addressing policy issues and conditions which affect the conduct of space science. The Panel Events concerned: The Future of Space and International Cooperation; Space Sciences in Europe; The Future of Humans in Space and the Role of ISS; Highlights from the recent Mars Missions and the Future of Mars Exploration jointly sponsored by COSPAR and IAA; The Role of Space in Monitoring Global Change.

During the Panel Event "The Future of Space and International Cooperation", guided by Prof. Sagdeev, panelists were the leaders of NASA, ESA, RKA, JACSA, Chinese and Indian space agencies. In his speech, J. J. Dodrain - the General Director of ESA, focused on the role of space research as a contributor to the success of EU enlargement. He welcomed the association of new EU Member States, as well as of

Rumania, to ESA activities and the European Space Policy. These countries have already established Cooperation Agreements with the ESA. Bulgaria was not mentioned among these countries. Participating Bulgarian scientists discussed that additional efforts of Bulgarian space research community are needed to stress on and foster establishment of Framework Cooperation Agreement between the ESA and the Bulgarian Government concerning participation in ESA programs and White Paper process in Europe.

ACKNOWLEDGEMENTS. Jordanka Semkova is grateful to the Editorial Board of the Aerospace Research in Bulgaria journal for the assistance in accreditation as a reporter to the 35th COSPAR Scientific Assembly - Paris.

A Brief Report on the 10th Scientific Assembly of the International Association of Geomagnetism and Aeronomy

Rositsa Koleva

Solar-Terrestrial Influences Laboratory, Bulgarian Academy of Sciences

The 10th Scientific Assembly of the International Association of Geomagnetism and Aeronomy (IAGA) took place from 18 till 29 July, 2005 in Toulouse, France. IAGA is one of the seven associations of the International Union on Geodesy and Geophysics (IUGG). The objective of IAGA is to promote and coordinate studies in a large area of Earth's sciences – "From the Sun and Planets ... to the Earth's deep interior" as its slogan says. IAGA is organised into five Divisions and two Interdivisional Commissions: D1. Internal Magnetic Field; D2. Aeronomic Phenomena; D3. Magnetospheric Phenomena; D4. Solar Wind and Interplanetary Field; D5. Geomagnetic Observations, Surveys and History; ID Commission on History; ID Commission on Developing Countries. The fields of interest to the readers of this journal – divisions D3 and D4, overlap with the research dine within COSPAR, but the organisers of the IAGA Assembly tried to find different aspects of the scientific investigations and the emphasis in the presented papers was placed on results form global and micro-scale modelling and the extent to which the models are confirmed by experimental evidence. As there were no Bulgarian presentations at the 10th Assembly, I shall try to provide a brief overview of the presentations which

impressed me. A particular feature of IAGA Assemblies are the Reporter Review Sessions in each Division in which scientists nominated in advance review the last two-years publications on a given topic. In his review on inner magnetosphere interaction [1], J. Goldstein stated that the basic dynamics and global structure of the inner magnetospheric electric field has been obtained, and important sub-global contributions, due to coupling between the ring current and ionosphere, have been identified. Long-suspected relationships between the hot plasmas (ring current and radiation belts) and the colder plasmas (plasmasphere, ionosphere) have been demonstrated. In his review on ULF waves [2], D. H. Lee noted that over 140 papers were published on the topic in the preceding 2 years, but he outlined about 40. On ULF waves in the boundary layers, the paper by Teodosiev at al.[3] was cited. Bulgaria was mentioned once more – in his talk, J. Bougeret [4] spoke about the Regional Planning Meeting for the Balkan and Black Sea Region, which was held in Sozopol, Bulgaria, 6-8 June 2005, hosted by STIL-BAS. Of particular interest to many space researchers was the review on CMEs, presented by R. Schwenn [5]. He pointed that, in recent years, an unprecedented amount of high-quality data from various space probes has been piled up that exhibit the enormous variety of CME properties and their effects on the whole heliosphere. However, major problems could still not be solved, e.g. what are the mechanisms of CME; how are CMEs related to flares; at the Sun CME has a 4-region structure, but in the interplanetary space CME exhibits only a 2-region structure – how and why this evolution takes place; etc. Many presentations were devoted to storms and substorms. T. Pulkkinen [6] presented evidence that the energy dissipation in the magnetosphere-ionosphere system is driven by the z-component of the interplanetary magnetic field, but is controlled by the solar wind dynamic pressure. Issues concerning superstorms were controversial. M. W. Liemohn et al., [7] conclude that geomagnetic storms with different intensities are merely a continuum of responses to solar wind inputs, all having the same coupling functions. On the contrary, Kozyra et al., [8] reported that superstorms, especially those occurring in the presence of low solar wind density exhibit unusual features.

At the Assembly, four associated lectures were delivered. Though they were given early in the morning in a large and representative lecture room, they were attended by a large audience. D. Loper [9] focused on the role of the geomagnetic field in the evolution of life on Earth. According to him, life on Earth became possible because of the existence of the closed loop: magnetic field, which preserves water – water, which permits plate

tectonics – plate tectonics, which provides the cooling necessary to sustain a dynamo in the core, the latter generating the magnetic field. The lecture delivered by D. Baker was devoted to the Electronic Geophysical Year (eGY) proposed in commemoration of the International Geophysical Year (1957 – 1958). eGY provides an opportunity for the international geoscientific community to focus effort on a 21-st Century e-Science approach to issues of data stewardship: open access to data, data preservation, data discovery, data rescue, capacity building, and outreach. The development of Virtual Observatories and Laboratories is a central feature of eGY. eGY is an internationally-recognized resolution by the scientific community to achieve a step increase in making past, present, and future geoscientific data readily, rapidly, conveniently, and openly available. The challenges of eGY concern many space researchers in Bulgaria and I recommend visiting its web site at http://www.egy.org/ab.

References

1. Goldstein, J., Global interactions of the inner magnetospheric plasmas, IAGA2005-A-00941.
2. Lee, D. H. Reporter review of ULF waves, IAGA2005-A-00521.
3. Teodosiev, D., P. Nenovski, P. Hristov, R. Koleva, J. Vojta, P. Trisk, J. Chum, I. Shibaev, ULF wave measurements aboard the Magion-4 subsatellite: narrow-band wave events observed in the magnetopause regions, *Planet. Space Sci.*, 53, pp 317-326, 2005.
4. Bougeret, J. L., Davila, J., Harrison, R., et al., Science during the International Heliospheric Year 2007-8, IAGA2005-A-01461.
5. Schwenn, R., CMEs, solar wind and Sun-Earth connections: CMEs, solar wind, and Sun-Earth connections: unresolved issues, IAGA2005-A-00839.
6. Pulkkinen, T. I., M. Palmroth, T. V. Laitinen, P. Janhunen, M. A., Shukhtina and V. A. Sergeev, Magnetospheric energy circulation: characterization of dynamic states from observations and global MHD simulation, IAGA2005-A-00748.
7. Liemohn, M. W., J.-Ch. Zhang, M. F. Thomsen, and J. U. Kozyra, Comparison of solar wind, geophysical, and geosynchronous characteristics for moderate, intense, and super storms, IAGA-2005-A-00886.
8. Kozyra, J., and the Superstorms Analysis Team, Crossing the threshold to superstorms, IAGA2005-A-01431.
9. Loper, D., Earth's magnetic field and life, IAGA2005-A-1559.
10. Baker, D., YGY+50 and eGY, IAGA2005-A-01558.

JUBILEES

Prof. Dr. Dipl. Eng. Petar Getsov Became 55 Years of Age

Prof. Petar Getsov was born on October 20, 1950, in the Village of Samovodene, Town of Veliko Turnovo. He is a renowned expert in the field of Aerospace Device Construction and Automatic Regulation and Control Systems, and Study of Man as a Controlling Body in Control (Ergatic) Systems). The notorious career of Prof. Getsov dates since 1974, when he graduated from the *G. Benkovski* Higher Military Aviation School, Town of Dolna Mitropoliya, as Engineer in Aircraft Electrical, Instrumentation, and Automatic Equipment. In 1978, at the N. E. Zhukovski Higher Military Engineering Academy, Moscow, Prof. Getsov presented his PhD Thesis entitled Study of the Operational Efficiency of an Aircraft Power-Supply Automatic Regulation System by the Method of Semi-Nature Modelling. In 1983, he was elected Associate Professor at the *G. Benkovski* HMAS in the subject of Aircraft Automatic Control and Regulation. In 1985 and 1986, he became Senior Researcher II rank, in the same subject at the Military Technical Scientific Research Institute at the Ministry of Defence of the Republic of Bulgaria, and the Space Research Institute at the Bulgarian Academy of Sciences, accordingly. In 2002, he was elected Senior Researcher I rank at the latter Institute.

Prof. Getsov has occupied successively the following positions: Lecturer, Senior Lecturer, and Vice Head of the Chair of Electrical Engineering and Aviation Equipment at the *G. Benkovski* HMAS, Head of the Aviation Equipment Department at the Military Technical Scientific Research Institute at the Ministry of Defence of the Republic of Bulgaria, Head of the Aerospace Devices and Telecontrol Department, Head of the Aerospace Control Systems Department at the Space Research Institute, BAS, Professor of Aerospace Instrumentation for Ecologic Monitoring at the New Bulgarian University, Sofia, Professor of Aviation Navigation and Control Systems at the Plovdiv Subsidiary of the Technical University of Sofia. Since 1996, Prof. Getsov is Director of the Space Research Institute, BAS. For 25 years already, Prof. Getsov has been head of various scientific

units; he was scientific leader of 20 graduate students and 10 post-graduate students. During his long and prolific scientific career, Prof. Getsov has participated in 57 scientific projects, being a participant in 10 of them and leader of the other 47. The publication activity of Prof. Getsov features 144 works (papers, reports, textbooks, monographs etc.); he has 71 citations at home and abroad. He has participated in 47 scientific contributions and has 50 innovations, author's certificates, implementations etc. Prof. Getsov is member of the following prestigious scientific formations: since 1995 - Chairman of the Scientific Council of the Space Research Institute – BAS, the Dedicated Scientific Council at the Military Committee in Military Engineering Sciences of the Higher Attesting Committee, since 2003 - member of the International Academy of Technological Sciences, since 2005 - member of the New York Academy of Sciences, member of the Interinstitutional Committee on Space Matters at the Council of Ministers of the Republic of Bulgaria. Prof. Getsov is Chairman of the Bulgarian Astronautical Society (2003) and of the Bulgarian Astronautical Federation (2004).

Prof. DSc Dipl. Eng. Garo Mardirossian Became 60 Years of Age

Prof. Garo Mardirossian was born on October 10, 1944, in Sofia. He graduated from the *Lomonossov* Exemplary Vocational School of Fine Mechanics and Optics, Sofia. Then, he completed by correspondence the Technical University in Sofia to become Weak Current Electrical Engineer. From 1965 to 1979 he worked at the Geophysical Institute of the Bulgarian Academy of Sciences where he held successively the offices of technician, expert master of scientific equipment, engineer, Research Fellow, and Head of the Central Laboratory of Seismology. In 1980, in relation with the implementation of the *Bugaria-1300* National Space Programme, he started working for the Space Research Institute of the BAS. Since 1990 he has been Senior Researcher in Remote Sensing Techniques and Equipment for Study of the Earth and Planets, in Ecology and Economy. His core scientific interest is focused on the study of ecologic catastrophes using ground-based (contact) and aerospace (remote) techniques and equipment. He is one of the founders of the Master's and

Post-Graduate Programme in Remote Sensing Aerospace Studies at the New Bulgarian University.

Prof. Garo Mardirossian is author of more than 80 scientific publications, about 60 scientific reports, 4 books, dozens of scientific-popular papers, and 24 invention patents. He is Honoured Inventor since 1982. He has presented two PhD Theses in Geophysics (1985 and 2000). He has participated in the implementation of nearly all significant national and international space projects with Bulgarian participation. In 1991, G. Mardirossian was elected Professor rank and nominated active member of the PWPA (Professors World Peace Academy), New York, on account of his „scientific, application, inventor's and science-popularization activity, as well as his merits for the democratization process". In 1999, his name was inscribed onto the Golden Book of Bulgarian Inventors and Discoverers, and in 2000 - on the Encyclopedia of the 2000 Most Prominent Scientists of the XX Century, issued by the Cambridge Biographical Centre.

In 2002, Prof. Mardirossian won an international competition and was invited to work for the National Center for Scientific Research (Centre National de la Recherche Scientifique - CNRS), France, on the topic of Remote Sensing of Earth Atmosphere funded under NATO's Scientific Programme. In 2003, he presented his Doctor's Thesis in the field of technical sciences. Since 2004, he has been Chairman of the General Assembly of Scientists, and since 2005 - Senior Researcher, I rank at the SRI-BAS. Prof. Mardirossian has great merit for the establishment and consolidation of the journal „Aerospace Studies in Bulgaria", issued periodically, to which he has been Secretary-in-Chief since 1982, and Vice Chief Editor since 1996.

Prof. DSc Hernani Borisov Spiridonov Became 70 Years of Age

The scientific biography of Prof. Spiridonov began long ago, in 1963, at the Enterprise for Geophysical Prospecting and Geologic Mapping at the Committee of Geology, Sofia, where he held the office of geologist-geomorphologist. There, he participated in the geologic and geomorphologic mapping and search of ores and minerals, initially in the capacity of mapping geologist, and later

– as head of a geological team. The material collected and processed by him during that period was summarized in his PhD Thesis entitled "Morphotectonics of the Northern Slopes of the East Rila Mountain and Part of the West Rhodopes Mountain", which he presented successfully in 1975.In the same year, upon winning a competition, he was appointed Research Fellow, I rank, at the Space Research Institute of the Bulgarian Academy of Sciences. He was the first researcher employed at the Remote Sensing of the Earth from Space Department. From 1975 to 1980 he was Leader of a Problem Group, and from 1980 to 2005 he was Head of the Remote Sensing of the Earth from Space Department. In 1995, he presented his Doctor's Thesis on the topic "Ring Morphostructures in the Sredna Gora Mountain" after which, in 1996, he was appointed Senior Researcher, I rank. In 1997, he was elected Professor.

The abundant scientific and creative biography of Prof. Spiridonov includes over 200 scientific works, of them: 112 publications, over 60 papers and communications, and over 30 reports, related with international scientific expeditions and tasks of the Space Research Institute, the greater part of which are stored at the National Centre for Information Activity, Sofia. He is author of a great number of monographs, 10 of which have been published in Russia, England, Poland, Czechia, Slovakia, Mongolia, and Vietnam, and 15 – in Bulgaria. Apart from these, in 1999, he published the monograph "Ring Morphostructures in the Sredna Gora Mountain", which was distinguished by a Diploma of the Union of Scientists in Bulgaria. In the field of science-popularization activity, Prof. Spiridonov has published 3 books: "A Close Look at Vietnam", "Space and Natural Resources", and "Study of the Earth from Space".

Prof. Spiridonov has participated in a number of international forums, congresses, conferences, and symposia in Russia, Poland, Czechia, Slovakia, Hungary, Romania, Cuba, Germany, Finland, India, Mongolia, and Vietnam, to many of which he was invited lecturer. From 1975 to 1991 he was member of the Office of the Work Group on Remote Sensing of the Earth from Space Using Aerospace Techniques, which in 1991 was one of the scientific schools under the *Intercosmos* International Programme. At the same time, he was National Coordinator to the Methods for Interpretation of Remote Sensing Data Scientific School (Section No.2), whereby Bulgaria participated in the international space program. He participated in the preparation of the scientific programs in the field of geologic study of the Earth; remote sensing in geography, agriculture and forest economy, ecology, and thematic mapping.

Prof. Spiridonov was leader of over 50 airplane expeditions conducted on the territory of Bulgaria and other countries, during which synchronous and quasi-synchronous measurements were performed at three levels: satellite, airplane, and ground level. He was leader of the Bulgarian scientists who worked at various test sites under the projects Caribe, Tyan Shan, Gobi Hangai, Biosphere-K, Tropico-3, Spectr, Bulgaria-1300, Kiolong, Erdem etc.

Prof. Spiridonov was the founder of aerospace research in Bulgaria and their application in natural sciences. There are over 200 citations of his publications, more than ? of which abroad. He was many times reviewer of PhD and Doctor's Theses on Professor Election Procedures. He was Chief Editor and Co-Editor of numerous monographs, collections, and journals. He was awarded orders and medals by the Bulgarian and Russian State in relation with the successful missions of both Bulgarian astronauts. He was scientific leader of post-graduate students at the SRI-BAS, and the *Saint Ivan Rilski* University of Mining and Geology. For ten years already he has been Chief Editor of the Geomorphologic Map of Bulgaria issued in scale M 1:100 000. Prof. Spiridonov has lectured at various institutes in Russia, Mongolia, Vietnam, and Cuba, and in the recent years, at the *Archbishop K. Preslavski* University of Shoumen and the *Saint Ivan Rilski* University of Mining and Geology. He has participated as leader of various projects and contracts, both international, as well as home ones. During 1994–1995, he was leader of the interpretation team under the *CORINE Land Cover* International Contract at the European Union under the PHARE Programme. He was for thirty years leader of the Remote Sensing of the Earth from Space Department at the SRI-BAS, three mandates – member of the General Assembly of the BAS and 10 years - Chairman of the Scientific Council of the SRI-BAS.

Prof. Spiridonov created the Remote Sensing of the Earth from Space scientific school at the SRI-BAS, which was at the time a pioneer school for Bulgaria and the BAS. He has his third mandate as member of the Scientific Expert Committee in Earth Sciences and member of the Dedicated Scientific Council of Geography; he has been for three mandates Chairman of the Scientific Council at the SRI-BAS and member of the Scientific Council of Geography at the Institute of Geography; he was for 17 years National Representative of Bulgaria under the *Intercosmos* Programme in the Remote Sensing of the Earth Using Aerospace Techniques scientific school and National Coordinator of the Remote Sensing Data Interpretation Methods scientific school. During 1975–1999, he was member of the COSPAR ISC on Space Studies of the Earth's

Surface, Meteorology and Climate, Subcommission A.3 - Geology and Productivity of Land Surface and Oceans. He was elected Expert at the European Committee - Directorate-General XII - Science, Research and Development No.EE1998A14345. On 21.02.2003, he was elected member of the research team of the International Biographical Center Research Council, Cambridge, England, for his contribution in the field of geology, neotectonics, and remote sensing.

We wish Prof. DSc Hernani Spiridonov health and longevity. Happy jubilee, Prof. Spiridonov!

Prof. DSc Dipl. Eng. Nikola Georgiev Became 70 Years of Age

Prof. Nikola Georgiev displayed professional interest in the field of geodesy yet in juvenile age. He graduated from the *Hristo Botev* Construction School in Sofia, and afterwards majored in Geodesy, Photogrammetry, and Cartography at the Higher Institute of Architecture and Construction.

The scientific and pedagogical career of Prof. Georgiev started at the Higher People's Military Artillery School, Town of Shoumen, where he lectured in Mathematical Geodesy and Cartography, Geodetic Astronomy, and Physical Geodesy. During this period he became post-graduate student of the prominent Bulgarian scientist-geodesist, Acad. Vl. Hristov, and in 1967 presented his PhD Thesis on the topic "The Direct and Reverse Geodetic Problem for Great Distances" issued as a monograph in 1967.

In 1965, N. Georgiev joined the Central Laboratory for Higher Geodesy (CLHG) at the Bulgarian Academy of Sciences (BAS) as a Research Fellow. Here, he focused his scientific activity and interests in the field of Space Geodesy, a new and prospective scientific field at that time. In recognition for his successful results, during 1975-1977, he was invited to work for the Council of Astronomy of the Russian Academy of Sciences, where he developed analytical theory for high-precision determination of Earth satellite orbits and their use for the purposes of space geodesy. In 1978, he presented his Doctorial Thesis at the *A. Sterberg* State Institute of Astronomy of the *M. Lomonossov* State University of Moscow on the topic "A Satellite Geodesy Orbital Method for Short Time Intervals" attaining the

title Doctor of Physico-Mathematical Sciences. Its major results were published in the joint Bulgarian-Russian monograph "Using Earth Satellite Optic Observations for Geodetic Purposes" which was published in 1979 and later on gained great popularity.

Upon his return to Bulgaria in 1977, N. Georgiev was appointed Director of the CLHG - BAS. Here, he organized a large team of researchers and professionals, with whom he developed intensively and successfully various aspects of the analytical theory for determination of satellite orbits, with particular emphasis on its application for the purposes of global geodynamics. Under his supervision, the CLHG continued its scientific research work in both the traditional fields of higher geodesy as well as in some new areas. In his capacity of Director of the CLHG, Prof. N. Georgiev paid particular attention to the young researchers assisting their scientific and creative development.

This period witnessed the consolidation and elevation to a new quantitative level of CLHG's international relations with the Academies of Science of Russia, Germany, Poland, Czechoslovakia, Roumania, Cuba and other countries. The CLHG established creative contacts with other geodetic, scientific, academic and production institutions in Bulgaria. The CLHG provided methodical supervision for the Satellite Photographic Observation Station at the *J. Gagarin* People's Astronomical Observatory with Planetarium, Town of Stara Zagora.

The career of Prof. N.Georgiev was marked not only by his prolific scientific activity, but by his pedagogical activity as well. He lectured at the Higher Institute of Architecture and Construction, the *Gen. Blagoy Ivanov* Higher People's Military Construction School, and the Higher People's Military Artillery School.

• 1975 - elected Sen. Res. II rank in Space and Mathematical Geodesy;

• 1981 - elected Sen. Res. I rank in Space and Mathematical Geodesy• 1982 - elected Professor in Geodesy at the *Gen. Blagoy Ivanov* HPMCS;

• 1990 – nowadays working at the Remote Sensing Department of the SRI-BAS.

Prof. Georgiev has over 200 scientific publications in dedicated journals, collections, international, foreign and Bulgarian editions, of them: published abroad - 88; in Bulgaria - 115; individual works - 59; team works – 139, being the first author of 105 of the latter. He has written 9 monographs. He was invited lecturer to 55 home and overseas forums, member of organizational, scientific, and program committees.

The results of the scientific and organizational activity of Prof. N. Georgiev resulted in his wide international recognition. He is member of

international and overseas organizations, his name is inscribed on a number of home and foreign encyclopedias, he was elected member of a number of foreign Academies of Science on account of his academic achievements, he is also leader of international projects and programs:

• *Corresponding Member* of the International Astronautical Academy (Internationalis Astronautica Academia MCMLX), Paris, elected in 1990;

• *Academician* of the International Astronautical Academy (Internationalis Astronautica Academia MCMLX), Paris, elected in 1997;

• *Expert* of the European Commission, Directorate General XII, Science, Research & Development, Subject EE 19981A1418, since July 02, 1999;

• *Subproject II–4.I* - " Dynamics Study of the Euro-Asian Lithosphere (IDEAL)";

• *Topic II-4.I-4.* - "Complex Geodynamic Interpretation of the Results";

• *Project IV, IDEAL* -"Motion Study of the Euro-Asian Lithosphere Using High-Precision Laser Distance Meters and Radio-Interferometric Observations";

• *Topic II. 1* "Optic Laser Light-Reflecting System", Satellite Bulgaria–1300-2;

• Chief Editor of: *"Higher Geodesy"* (issues Nos.5 to 14); *"Aerospace Research in Bulgaria"*, (issues Nos. 13 to 19).

Since 1990, Prof. Georgiev has been working for the SRI – BAS where he focused his attention on: the methods for coordinate attachment, rectification, and interpretation of high-resolution space images; space methods for study of regional and global geodynamics; analysis of remote-sensing and ground-based studies of the neotectonics and geodynamics of the Moesian platform. During this period, he was also Chairman of the General Assembly of Scientists.

During the successive periods of his carrier, Prof. DSc N. Georgiev was National Coordinator and active participant in prestigious international organizations, such as: INTERCOSMOS, KAPG, COSPAR, MAG, МСПГ, Scientific Secretary of the Dedicated Scientific Council in Geodesy and Geophysics; member of the Scientific Council in Geophysics at the Higher Attesting Committee (1983-1987 and since 2005 to nowadays); Vice-Chairman of the Dedicated Scientific Council in Geodesy at the Higher Attesting Committee (1985-1988 and since 2005 to nowadays). On account of his versatile activity he was awarded with Order of Cyril and Methodius, I class, the Golden Order of Labour, the Badge of an Excellent Worker of the BAS etc.

Yordanov, D. V. COMPUTER MODELS OF AIRPLANE AND HELICOPTER CONTROL SYSTEMS. Publishing House of the Technical University of Sofia, 2004-2005, 155p.

In 2005, the Publishing House of the Technical University, Sofia, presented to the attention of the experts in aviation equipment and technologies the textbook entitled "Computer Models of Airplane and Helicopter Control Systems" written by Sen. Res. Dr. Dimitar Vasilev Yordanov from the Space Research Institute of the BAS. In it, the author presents his ideas as to how the potentialities of the *Matlab–Simulink* software product may be used to interpret in a new way some problem issues related with the aircraft control contour's operation. The two parts of the textbook acquaint the reader with the methods of solving control system design problems, satisfying the controllability normative characteristics' requirements, and some applications of the models for study the control contour's operation in normal and emergency situations, related with control system failures or atmospheric disturbances. The models have been chosen for specific regimes where the control systems operation features some peculiarities, demanding a creative modeling approach to be applied. They do not cover the whole variety of problems characterizing control systems' operation. The aim of the author is to provoke the experts' research approach and their ability to take decisions based on modelling results. The correct solution of the problems requires of the author to have basic knowledge in the specific aviation field, computer literacy, and a reasonable amount of fantasy.

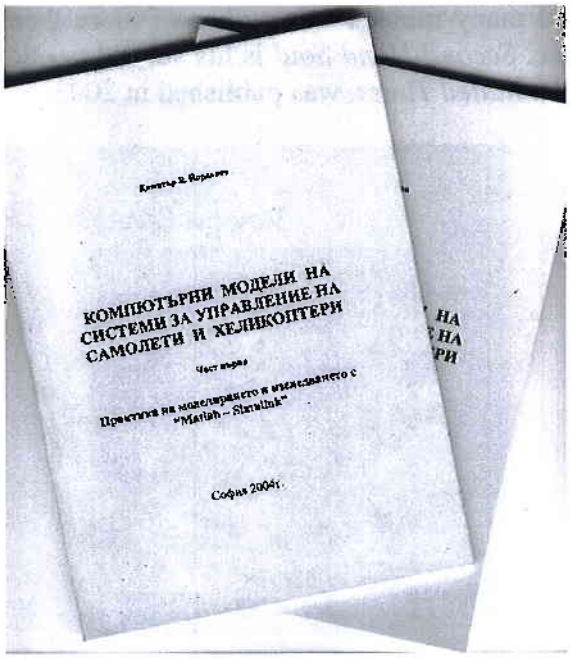

Vassev, V. S. SECOND-HAND SOUL, Collection of poems, ASI Publishing House, Sofia, 2005, 64 p.

The Editorial Board of the journal "Space Research in Bulgaria" is very pleased to present to the readers' audience the newly published book of the well-known and respected employee of the Space Research Institute, Mr. Valeri Vassev, whom all of us have admired for many years already for his genuine and unrivalled poetic gift.

Mr. Vassev was born on April 28, 1952, in Sofia. He majored as a historian from the *St. Kliment Ohridski* University of Sofia. For about two dozens of years already he has been practicing as journalist and publicist in the mass media. Mr. Vassev was Editor in the *Nauka and Izkustvo* and *Panorama* publishing houses, the *Bulgarska Armiya, Novinar*, and *Ossobeno Mnenie* newspapers and many more. He is author of more than 2000 papers, interviews, essays etc. *Second-Hand Soul* is his second poetic collection. The first one, entitled *Mutilated Times*, was published in 2003.

Do never open
the pages of a book,
the door to the unknown,
the petal of the rose
the anterior of love...
If you are not prepared to know:
time's infinity,
immortality's eternity,
life's wisdom,
your true Self...
For only then
you'll come to know:
who keeps the memory,
what keeps the Earth going round,
where the cycle originates...
And only then you will
discover the truth about:
the stars' beauty,
the burn of passion,
the light's might,
the magic of birth...
So that you might live forever after –
that is, your true Self...
no second-hand love...
your soul - an eternal traveller...

(Verse translated by L. Kraleva)
Res. Fellow L. Kraleva